ALMA MATER STUDIORUM
UNIVERSITÀ DI BOLOGNA

DOTTORATO DI RICERCA IN

SCIENZE DELLA TERRA, DELLA VITA E DELL'AMBIENTE

Ciclo 36

Settore Concorsuale: 04/A3 - GEOLOGIA APPLICATA, GEOGRAFIA FISICA E GEOMORFOLOGIA

Settore Scientifico Disciplinare: GEO/05 - GEOLOGIA APPLICATA

NUMERICAL MODELLING OF FLOW-LIKE LANDSLIDES AND THE RELATED PHENOMENA ADOPTING THE IMPROVED SMOOTHED PARTICLE HYDRODYNAMICS (SPH) MODELS

Presentata da: *Zhitian Qiao*

Coordinatore Dottorato

Maria Giovanna Belcastro

Supervisore

Matteo Berti

Esame finale anno 2024

Acknowledgements

Three years have passed in the blink of an eye, graduation is approaching and it's almost time to say goodbye. However, the scene of my first arrival in Bologna three years ago is still vivid in my memory. At that time, my emotions could be summarized in two words: excitement and fear. I was curious about this entirely new world, and eager to explore everything as soon as possible. However, at the same time, I felt afraid of this entirely unfamiliar environment because I knew that I would need to navigate this journey independently. Fortunately, I spent three incredibly memorable years in Bologna, during which I not only made academic progress but also gained a group of interesting and lovely friends. At this moment, two words come to mind: nostalgia and gratitude. I am reluctant to say goodbye to everything here—the people I've met, the experiences I've had, and even the belongings that have accompanied me. Most importantly, I would like to express my sincere gratitude to the following individuals and institutions whose support and guidance were instrumental in the completion of this PhD thesis.

My deepest appreciation goes to my PhD supervisor, Prof. Matteo Berti supervisor for his patience, wisdom, and encouragement during the highs and lows of the research process. I have to say that I'm so lucky to have such an excellent supervisor. He is professional in his field and has patience with young researchers. He provided me with the intellectual freedom to explore and the necessary guidance to navigate the complexities of my research. His support has not only enriched my academic knowledge but also facilitated my personal growth and transformation.

My sincere thanks to the Lecturer at Chang'an University, Wei Shen for his tireless dedication, encouragement, and invaluable insights throughout the entire thesis-writing process. He is a passionate young researcher with profound insights in the field of landslide dynamics and numerical simulation. We met during my master's studies. At that time, as a Ph.D. candidate, he always provided me with invaluable guidance and helped me polish the manuscript once and once again

Abstract

Flow-like landslides are a common and serious geologic hazard worldwide that can lead to substantial environmental degradation. They can severely damage infrastructure, including roads, bridges, buildings, and utility lines. Additionally, they may alter the natural landscape, cause deforestation, and contribute to soil erosion. Understanding the dynamic characteristics of this type of landslide is crucial for devising effective mitigation strategies and promoting resilience in vulnerable areas.

Numerical modeling plays a crucial role in understanding, predicting, and managing flow-like landslides. It provides valuable insights into the complex dynamics of catastrophic landslide events, allowing researchers, engineers, and policymakers to assess risks, and design mitigation measures. In this PhD thesis, three challenging topics (slope failure, landslide-structure interaction (LSI) and entrainment) are thoroughly analyzed by means of numerical modelling. To investigate the first topic, I first implemented the elastic-plastic constitutive model in the DualSPHysics framework to simulate the mechanical behavior of strain history-dependent materials such as cohesive soils. Furthermore, the failure and deformation processes of a cohesive soil slope without strain softening and that of a sensitive clay slope with strain softening, are studied to validate the proposed SPH model. The multiple failure process of the Caijiapo landslide (China) was analyzed by the developed SPH model. A novel SPH model was proposed to address the second and third topics. Due to the importance of friction in the dynamic simulation of flow-like landslides, an HBP rheology model coupled with the friction dissipation was embedded into the DualSPHysics code. Regarding LSI issues, column collapse and sand flume benchmarks were carried out to verify the performance and capability of the developed SPH model. Then, the propagation of a real debris-flow event occurring in northern Italy and its interaction with check dams installed along the flow path were analyzed. As for the last topic, the viscoplastic flow experiment on the erodible bed was selected to certify the capability of the SPH model in handling the entrainment phenomenon associated with flow-like landslides. Besides, the entrainment process of the Ximiaodian loess

landslide (China) was reconstructed using the SPH model combined with the HBP law considering friction dissipation.

Overall, this PhD thesis aims to improve our understanding of the sophisticated processes (slope failure, propagation and deposition) of flow-like landslides and the related phenomena (LSI and entrainment). The simulation results of the case studies in this thesis show that the improved SPH models perform well in simulating the flow-like landslides and the phenomena mentioned above, indicating the potential application of the improved SPH models in the risk assessment and management of flow-like landslides.

Contents

1. Introduction

1.1 Preface

My PhD project focuses on the numerical modeling of flow-like landslides. The main goal of this project is to improve the understanding of some complex flow-like landslide phenomena by numerical modeling approaches. In this thesis, three crucial topics in flow-like landslide simulation were discussed. The first topic is related to the slope failure. A landslide is the movement of rock, earth, or debris down an unstable slope. Almost every landslide starts with a slope failure. Slope failure occurs when forces acting down-slope (mainly due to gravity) exceed the strength of the earth materials that compose the slope. Slope failure is a crucial issue in geotechnical engineering. The second topic we discuss is landslide-structure interaction (LSI). It is an important topic in the field of disaster mitigation. The properties of both the flow mass and the protective structure influence the interaction mode, and an accurate prediction of impact forces acting on a structure is critical to the design of protective structures. The third topic is entrainment. Entrainment is a fundamental physical process in flow-like landslide dynamics, and it is responsible of the increase of flow volume along the path commonly observed in the field (Gregoretti et al., 2018; Han et al., 2015; Shen et al., 2019a). Accordingly, three improved SPH models based on the original DualSPHysics code were developed to investigate the above important processes of flow-like landslides.

1.2 State-of-the-art

Flow-like landslides are a disastrous natural hazard due to their high velocity and long run-out distance. Various phenomena such as slope failure, rock fragmentation, liquefaction, entrainment and landslide-structure interaction are involved in the initiation, propagation, and depositions of flow-like landslides. Understanding these phenomena is crucial for assessing the susceptibility of slopes to flow-like landslides, implementing effective early warning systems, and developing

strategies to mitigate the potential impacts on communities and infrastructure. The following mainly reviewed the state-of-the-art flow-like landslides from the slope failure mechanism, landslide-structure interaction (LSI) and entrainment mechanism.

1.2.1 Slope failure mechanism

Slope failure, also known as landslides or mass wasting, refers to the downslope movement of rock, soil, and debris under the influence of gravity. This phenomenon occurs when the forces acting to destabilize a slope exceed the strength of the materials holding it together. Slope failure can manifest in various forms, including slides, falls, flows, and complex combinations of these movements. Slope failure often involves large deformations, causing disastrous consequences to society. Therefore, slope stability analyses remain important in various fields such as geotechnical engineering, civil engineering, environmental science, and natural hazard assessment.

Since the mid-20th century, various methods and techniques have been employed to analyze and determine the safety of slopes. Limit equilibrium methods (LEMs) and finite element method (FEM) are two widely used slope stability analyses approaches. LEMs, such as Bishop's Method (Bishop, 1955), Janbu's Method (Janbu, 1968), Morgenstern and Price's method (Morgenstern and Price, 1965) and Spencer method (Spencer, 1967), analyzed slopes by considering equilibrium conditions and introduced the concept of the factor of safety. Although LEMs are widely accepted and have become standard practice in geotechnical engineering to assess slope stability due to their simplicity, they require the assumption of a critical slip surface. The accuracy of results is highly dependent on the correct identification of this surface, which can be challenging, especially in complex geological conditions. Numerical methods such as the finite element method (FEM) may be more suitable for such scenarios. FEM-based approach with the shear strength reduction (Griffiths and Lane, 1999; Zienkiewicz et al., 1975) is a numerical method that divides the slope into finite elements and analyzes the stress and deformation characteristics. It is particularly useful for complex geometries and heterogeneous materials. Despite that, in certain material models, especially when dealing with

large deformation problems, instabilities may arise, causing distortion in the mesh.

An alternative method to avoid mesh distortions is to adopt the meshless method, utilizing a set of particles to replace the mesh in FEM-based approaches. Material point method (MPM), particle finite element method (PFEM) and smooth particle hydrodynamics (SPH) are the three most commonly used particle-based numerical methods in the last two decades. The material particle method (MPM) has been adopted to study the progressive slope failure mechanism (Wang et al., 2016; Zabala and Alonso, 2011). A random MPM model was proposed to investigate the influence of heterogeneity on slope failure mechanisms involving large deformations (Wang et al., 2017). The particle finite element method (PFEM) was initially proposed for fluid mechanics applications (Oñate et al., 2011, 2008), but soon becoming a popular method for solid mechanics and geomechanics applications (Oliver et al., 2005; Zhang et al., 2020, 2017). The smooth particle hydrodynamics method (SPH) proposed by Bui et al., (2008) has recently been developed for solving large deformation problems in geotechnical engineering, and it has been proven to be a powerful numerical approach for capturing the post-failure behavior of geotechnical materials. Afterwards, some modified SPH models are developed to perform the deformation analyses of geomaterials (Bui and Nguyen, 2021; Nonoyama et al., 2015; Wang et al., 2019; Zhang et al., 2019).

1.2.2 Landslide-Structure Interaction (LSI)

Several previous studies have investigated the influence of protective structures on flow-like landslides. Accurate estimation of impact force acting on the protective structure is still a challenging task. On-site investigations, experimental measurements and numerical simulations are the three main ways to evaluate impact forces on protective structures. In the last few years, Limited field data at local scale have been well-documented because of the difficulties in monitoring fast and strong flows. A permanent monitoring station that was installed downstream of the Jiangjia Ravine in the early 1960s reported the maximum impact pressure and total discharge of 139 debris

flows that occurred between 1961 and 2000 (Hong et al., 2015). An observation system was devised at Mt Yakedake in Japan in 1972 to measure the impact force of the volcanic muddy flow (Suwa et al., 1973). A series of check dams and a flexible barrier is installed within the Illbach River. Impact on an instrumented flexible barrier was reported by Wendeler et al., (2007). Although this approach is able to acquire reliable in-situ data, maintenance of infrastructures post-failure and tracking of internal variables such as velocity as well as deformation of sliding bodies are still a huge problem. Therefore, many researchers adopted small-scale flume experiments to reproduce the impact process of the flow against obstacles and further analyze the blocking effect of the flow on obstacles. Small-scale laboratory experiments were designed to study the influence of a dam on granular avalanches (Faug et al., 2008a). Moriguchi et al., (2009) designed a small-scale sand flume test at different slopes and measured the impact force of sands on a fixed rigid wall. 64 tests were carried out to study the impact of dry granular flows on a rigid retaining wall model (Jiang and Towhata, 2013). Choi et al., (2018) conducted various tests to explore the influence of various arrangements of slit-type barriers. Cui et al., (2015) conducted a miniaturized flume experiment to measure impact force of viscous debris flow. Zhou et al., (2018) studied the effects of water content (0-30%) on the impact behavior of granular flows by flume model tests and proposed a dimensionless index called the suction number to quantify the effect of suction on the dynamic behavior of granular flows. Armanini et al., 2019 developed a rational approach to study dynamic impact of a water and sediments surge against a rigid wall. Rossi and Armanini, 2019 analyzed the dynamic impact of a debris flow surge against a slit check dam using the rational approach developed by Armanini et al., (2019), combined with the assumption that the streamlines of the surge continue undisturbed until the moment of impact, i.e. that the momentum exiting the slit is equal to that of the incoming flow portion of a width equal to the slit. Experiments using transparent analogue debris flows in a small-scale flume were conducted to investigate the bulk impact forces on rigid barriers (Sanvitale et al., 2021). Huang et al., (2022a) designed a laboratory flume test to investigate the effects of barrier stiffness on the flow kinematics and impact forces. These small-scale tests are simple and convenient for engineering purposes, but only suitable for those events with limited volume. However, centrifuge modeling methodologies are considered as a good alternative to appropriately

scale source volume and stress (Ng et al., 2017c). A series of centrifuge tests were carried out to investigate the effect of different geophysical flow types on different mitigation measures (Ng et al., 2019, 2017c; Song et al., 2018, 2017; Zhang and Huang, 2022).

Numerical modelling is an efficient method for exploring the dynamic impact characteristics of landslide-structure interactions owing to its advantages of high repeatability and low cost. According to Austrian Standard Regulation 24801, Hübl et al., (2017) developed a standardized stress model for design of torrential barriers under impact by debris flow. A model-based approach for the design and performance evaluation of works controlling stony debris flows was proposed by Bernard et al., (2019). The depth-averaged model widely used in the numerical simulation of debris flow is unable to achieve this goal due to the lack of vertical information. In contrast, full 3D models such as the Discrete Element Method (DEM), Smoothed Particle Hydrodynamics method (SPH) and Material Point Method (MPM) can successfully address this issue. Calvetti et al., (2017) assessed the maximum impact force of a dry granular flow on the rigid barrier by means of a DEM model and further a simplified formula was proposed to calculate the maximum impact force. Ng et al., (2017a) applied a DEM model to explore the interaction between dry granular flow and rigid barrier deflectors and discussed the influence of different structural forms on flow-structure interaction. Shen et al., (2018) quantified the impact of dry debris flow against a rigid barrier through DEM analyses of flume tests. Zhang and Huang, (2022) presented a novel centrifuge model and calibrated by a DEM model to evaluate the influence of flow speed and on the impact behavior of granular flow. Dai et al., (2017) developed a fluid–structure coupled numerical model based on SPH to estimate the impact force of debris flows. He et al., (2018) evaluated the interaction between dry granular flows and rigid barrier using an incompressible smoothed particle hydrodynamics (ISPH) model. Sheikh et al., (2021) incorporated two boundary algorithms into the SPH mothed for estimating the boundary interaction force of a column of granular material collapsing onto a frictional surface. A flow–structure coupled with SPH model was presented by Huang et al., (2022b) to investigate the effects of barrier stiffness on the debris impact. Mast et al., (2014) used an MPM model to quantify the force interaction between a gravity-driven landslide and a square rigid column.

A soft–rigid contact model was built in the coding framework of MPM and calibrated by an idealized debris avalanche flow that flows down hillslope and hits a retaining wall (Li et al., 2018). Li et al., (2020) developed two contact models in the MPM computational scheme to evaluate the impact force acted on baffle structures. In order to gain a better understanding of impact mechanisms of dry or saturated granular flows against rigid walls, Cuomo et al., (2021) established an MPM model for simulating flume tests of Moriguchi et al., (2009) and (Song et al., 2017). In recent years, many coupled approaches such as DEM-CFD (Li and Zhao, 2018), SPH-FEM (Chen et al., 2019), MPM-DEM (Liu et al., 2018), SPH-DEM (Trujillo-Vela et al., 2020), SPH-DEM-FEM (Liu and Liang, 2022) have been developed and contributed to the design of mitigation strategies.

1.2.3 Entrainment mechanism

Gravity-driven flows can erode the bed along which they descend and increase the volume of material initially mobilized (Bates et al., 2016). This process is called basal entrainment and is a common phenomenon associated with flow-like landslides. Previous studies indicate that the final mass accumulated in the deposition area can expand to 1 to 12 times (Sovilla et al., 2006), or even 50 times (Hungr et al., 2007), the initial mass. Therefore, entrainment plays a significant role in the volume-enlarged flow-like landslide.

So far, great efforts have been made to study the entrainment of flow-like landslides. Among them, Field observation and monitoring are the most direct method. Sovilla et al., (2006) studied entrainment in snow avalanches using observations from (1) the Swiss Vallée de la Sionne test site, (2) the Italian Pizzac site, (3) catastrophic avalanches that occurred during the winter 1998–1999 in Switzerland, and (4) a medium-sized spontaneous avalanche that occurred in 2000 in Davos, Switzerland. Berger et al., (2011) installed erosion sensors in the channel of the Illgraben catchment in western Switzerland and measured the timing and magnitude of channel bed erosion by three debris flows occurred in 2008. Schürch et al., (2011) applied terrestrial laser scanning and flow hydrograph analysis to quantify erosion and deposition in a series of debris flows at Illgraben,

Switzerland. In 2014, a monitoring station was installed in the initiation area of the Cancia debris-flow channel that recorded many events in the period 2015-2023. Simoni et al., (2020) investigated erosion–deposition dynamics of July 2015 debris-flow events in relation to the slope of the debris flow channel and its local morphology.

Many laboratory tests have been done on granular flows over the erodible bed layers. Flume experiments were conducted by Egashira et al. (2001) to study the effect of bed sediment size on entrainment. They found that increasing particle size of the flow relative to the particle size in the bed could increase erosion rate. Two erosional dam-break wave experiments conducted to study the effect of sediment material properties on the entrainment (Fraccarollo and Capart, 2002). Small-scale experiments were performed to investigate the effect of an erodible bed on the mobility of a granular flow (Crosta et al., 2017; Farin et al., 2014; Mangeney et al., 2010). Bates and Ancey, (2017) studied bed entrainment by conducting dam-break experiments releasing a fixed amount of viscoplastic fluid (a Herschel–Bulkley fluid) on a sloping, erodible bed of fixed depth. Experiments are limited by scale and material issues. For instance, Iverson (1997) indicated the importance of the scale factor in simulation of granular flows. Takagi et al (2011) stated that the shape of particles significantly affects the motion of shallow granular flows (e.g., small-scale debris flows experiments).

With the advance of computer technology, numerical modelling has become a good alternative for flow-like landslide entrainment analysis. Particle-based model is the widely used method among the recent numerical models capable of simulating the entrainment process of flow-like landslides in recent years. Particle Finite Element Method (PFEM), Smoothed Hydrodynamics Method (SPH) and Material Point Method (MPM) are the three common particle-based models. Oñate et al., (2006) proposed a PFEM model to solve bed erosion problems in free surface flow. (Galano et al., 2021) extended the capabilities of the PFEM method to model sediment transport and scouring effects. A three-dimensional, surface cell (SC)-based smooth particle hydrodynamics (SPH) model was proposed to simulate bed-sediment entrainment by viscous debris flows (Han et al., 2020). An elastic-viscoplastic model (Ulrich, 2013) was also combined to a multi-phase SPH formulation (Hu

and Adams, 2006) to model granular flows and non-cohesive sediment transport (Ghaïtanellis et al., 2018). Various erosion and entrainment behaviors in snow avalanches were studied using the material point method (Li et al., 2022). An MPM model that can capture entrainment from a wet erodible bed is implemented to investigate debris flow entrainment (Vicari et al., 2022).

Based on the above studies, it is clear that entrainment mechanisms vary with different types of landslides, because of their difference in the material components and properties. For debris flows, the material entrainment can be generally summarized as two steps (Frank et al., 2015; Hungr et al., 2007; Iverson and Ouyang, 2015). The first step is bed destabilization and erosion (Fig. 1.1a). Bed erosion occurs when the bed strength reduces, possibly caused by the rapid undrained loading, impact loading and liquefaction. Subsequently, instability of stream banks undercut by bed erosion triggers the second step of the entrainment: side-bank collapse (Fig. 1.1b). In snow avalanches, frontal entrainment and basal erosion are two common entrainment mechanisms (Gauer and Issler, 2004; Li et al., 2022; Sovilla and Bartelt, 2002). For rock avalanches, the entrainment mechanism is composed of plowing at the margins and erosion at the base (Hungr and Evans, 2004; McDougall and Hungr, 2005). As shown in Fig. 1.2, the basal materials are entrained into the flow during the scouring process. Plowing is the dominant mechanism at the margin where materials can be plowed into and displace the front materials.
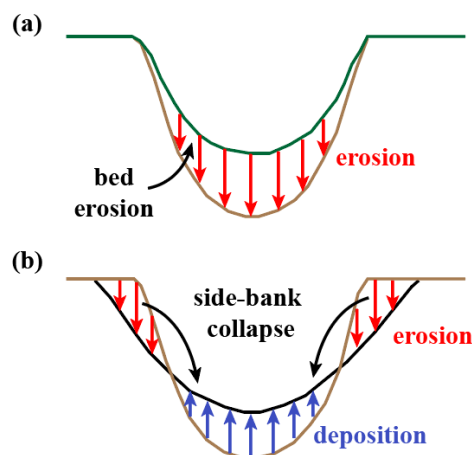
Fig. 1.1 Schematic diagram of entrainment mechanism in debris flows: (**a**) bed erosion and (**b**) side-bank collapse (Frank et al., 2015)
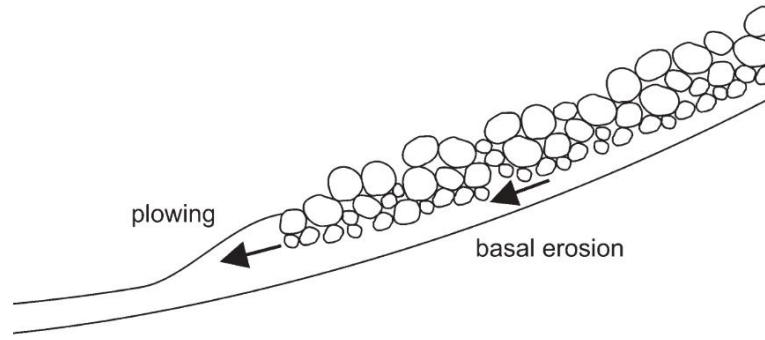
Fig. 1.2 Schematic diagram of entrainment mechanism in rock avalanches (McDougall and Hungr, 2005)

In recent years, several entrainment models have been proposed and widely applied in the simulation of the debris flow. According to the work of Medina et al., (2008), the existing scheme for simulating entrainment can be generally summarized into two categories: the static and the dynamic approach. Both methods follow the same entrainment conditions: basal erosion is triggered when the bed shear force is greater than the resistance force. However, the static approach considers a static equilibrium between the bed shear force and the basal resistance force, and an explicit entrainment or erosion depth can be obtained by Eq. (1.1). Conversely, the second approach applies a dynamic equilibrium to compute the erosion depth. For this type of method, the quantity of the erosive mass depended on the momentum conservation.

$$h_{ero} = \frac{\tau_b - \tau_{res}}{\rho g (\cos\theta \tan\varphi_b - \sin\theta)} \tag{1.1}$$

where h_{ero} is the erosion depth, τ_b and τ_{res} are the bed shear force and resistance force, respectively. θ is the slope of the sliding surface, and φ_b is the basal friction angle.

With respect to the dynamic approach, A physically based model was presented by Fraccarollo and Capart, (2002) and the expression of E is given by:

$$E = \frac{\tau_b - \tau_{res}}{\rho \bar{v}} \tag{1.2}$$

In which E represents the entrainment rate and with a unit of m/s, $\bar{v}$ is the mean velocity of the debris flow.

The physical based model is deduced by mechanical analysis and has a clear physical meaning, which is beneficial for understanding the complex entrainment mechanism. In addition, it can more accurately capture the evolution of the 3D terrain. In recent years, this model has been widely used to reproduce the complicated entrainment process (Han et al., 2018, 2015; Iverson, 2012; Iverson and Ouyang, 2015; Sovilla et al., 2006). On the other hand, Hungr, (1995) proposed a simple yet effective entrainment model that has been currently developed by other researchers for the dynamic simulation of debris flow (Blanc et al., 2011; McDougall and Hungr, 2005). For this empirical model, the entrainment rate is assumed to be proportional to the flow velocity and the debris depth:

$$E = E_r h v \tag{1.3}$$

where E_r is the growth rate (with a unit of m^{-1}) describing the relative volume increase per unit displacement. This parameter needs to be input by users and further adjusted by back-analysis. The expression of E_r is given by:

$$E = \frac{ln(V_f/V_0)}{L} \tag{1.4}$$

where V_0, V_f are volumes of material entering and exiting the entrainment zone, respectively, and L is the estimated average path length of the entrainment zone. This equation is derived from the assumption of natural exponential growth of landslide volume with displacement, and it can provide a preliminary estimation.

1.3 Objectives and research questions

Flow-like landslides often occur in mountainous or hilly terrain where human settlements are present. The rapid and destructive nature of these events can result in loss of life, injuries, and displacement of communities. Therefore, flow-like landslides have become an urgent task for the safety of the surrounding villages. Although great efforts have been made in terms of slope failure analysis (Dey et al., 2015; Griffiths and Lane, 1999; Jin et al., 2020a; Kohv et al., 2010; Li et al., 2016; Liu et al., 2019; Nonoyama et al., 2015; Sun et al., 2022; Wang et al., 2016; H. Wang et al., 2021; Xu et al., 2014; Yuan et al., 2020; Zhang et al., 2018), evaluation of landslide-structure interaction (Abdelrazek et al., 2016; Armanini et al., 2019; Bernard et al., 2019; Calvetti et al., 2017;

Chen et al., 2019, 2021; Choi et al., 2018; Cui et al., 2015; Cuomo et al., 2022, 2021; Hong et al., 2015; Jiang and Towhata, 2013; Liu and Liang, 2022; Mast et al., 2014; Ng et al., 2017c) and estimation of entrainment (Bates and Ancey, 2017; Berger et al., 2011; Fraccarollo and Capart, 2002; Frank et al., 2015; Ghaïtanellis et al., 2018; Goodwin et al., 2023; Guo et al., 2022; Han et al., 2015; Hungr et al., 2007; Iverson and Ouyang, 2015; Nikooei and Manzari, 2021), the dynamic processes of flow-like landslides are not yet fully understood. As a result, the numerical reproduction of this type of landslide is still challenging. It is therefore of great significance to better understand the above complex phenomena involved in flow-like landslides for landslide prevention. This thesis helps address the need for improved understanding by numerically modeling flow-like landslides using the modified DualSPHysics code. The followings are the main research questions of this thesis:

Q1: Can we deepen our knowledge of complex slope failure mechanisms using SPH models? Will the slope failure mechanisms differ depending on their distinct characteristics and geological conditions?

Q2: How to correctly predict the impact force of fast flowing front on protective structures? Are the interaction mechanisms between different types of protective structures and debris flows different?

Q3: What is the entrainment mechanism of loess landslide? How does the friction coefficient affect the entrainment pattern?

1.4 Outline of thesis

This thesis has been organized into six chapters. This first chapter reviews the background of the three research topics on flow-like landslides and demonstrates the objectives of the research. Chapter 2 briefly introduces the DualSPHysics code. Chapters 3, 4 and 5 can be considered as three independent works corresponding to answering the above three research questions.

In more detail, Chapter 2 introduces the Theory of the Smooth Particle Hydrodynamics method (SPH) implemented in DualSPHysics. Firstly, the interpolation approximation and smoothing kernel functions are introduced in Section 2.1 and Section 2.2, respectively. Then governing equations and various diffusive treatments are discussed in Section 2.4-2.5. Section 2.6 and Section 2.7 to provide an overview about the time stepping algorithms and boundary condition treatments, respectively. Finally, the general workflow of the DualSPHysics code is summarized in Section 2.8.

In Chapter 3, the elastic-plastic constitutive model was incorporated into the original DualSPHysics code to extend its application in simulating strain history-dependent materials such as cohesive soils. Two benchmark cases, the failure process of a cohesive soil slope without strain softening and that of a sensitive clay slope with strain softening, are studied to validate the improved SPH model. The simulation results illustrate that our model can effectively predict the large deformation of the cohesive soil slope and the sensitive clay slope. Then the run-out process of the Caijiapo landslide is analyzed by the modified SPH model to investigate its failure mechanism.

In Chapter 4, we proposed a novel SPH model for analyzing the interaction between debris flow and prevention structures, by incorporating a modified HBP law with frictional dissipation into the original SPH model. The proposed model is validated by column collapse and flume benchmark experiments first, and then utilized to analyze a real debris flow and its interaction with the prevention structures in the Cancia catchment in northern Italian Alps. The results of the column collapse experiment show that our model exhibits a better performance in simulating the collapse process compared with the original SPH model, and the simulation results of the sand flume test illustrate that the proposed model can accurately predict the impact force of debris flow on the prevention structure. Additionally, the research of this chapter has been published in the journal *Landslides*: Qiao, Z., Shen, W., Berti, M., Li, T., 2023b. An advanced SPH model for protective constructions of debris flows adopting the modified HBP constitutive law. Landslides. https://doi.org/10.1007/s10346-023-02123-6

Chapter 5 is focused on the entrainment process associated with flow-like landslides. Firstly, experiments of viscoplastic flow over erodible beds with different yield strengths (Bates and Ancey, 2017) were simulated using the original SPH model combined with the HBP constitutive law. Then we investigated the effect of bed yield strength on the mobility of the flow. Finally, we extended the SPH model into a real loess landslide. The Ximiaosdian Landslide (China) was reproduced by coupling the SPH model and the HBP law considering friction dissipation.

Chapter 6 presents the overall conclusions drawn from the research of this thesis and provides recommendations for future studies. Conclusions of Chapters 3-5 are provided at the end of each chapter after each technical paper. The references cited in Chapters 1-5 are listed in the Reference Chapter at the end of the thesis.

1.5 Other research progress during the PhD period

During my PhD, I also studied the runout characteristics and entrainment phenomena of flow-like landslides using depth-averaged models. In Section 1.5.1, we comprehensively analyzed the influence of numerical methods on the run-out, entrainment and deposition characteristics of an alpine debris flow. And the related research results have been published in the journal of *Frontiers in Earth Science:* Qiao, Z., Li, T., Simoni, A., Gregoretti, C., Bernard, M., Wu, S., Shen, W., Berti, M., 2023a. Numerical modelling of an alpine debris flow by considering bed entrainment. Front. Earth Sci. 10, 1–17. https://doi.org/10.3389/feart.2022.1059525. In Section 1.5.2, the influence of slope gradient and gully channel on the run-out, entrainment and deposition characteristics of a rockslide-debris flow were investigated. The related research results have been published in the journal of *Landslides*: Shen, W., Berti, M., Li, T., Benini, A., Qiao, Z., 2022. The influence of slope gradient and gully channel on the run-out behavior of rockslide-debris flow: an analysis on the Verghereto landslide in Italy. Landslides 19, 885–900. https://doi.org/10.1007/s10346-022-01848-0

1.5.1 Influence of numerical methods on the run-out and entrainment of an alpine debris flow

In this paper, two typical depth-averaged models have been used to analyze a well-documented debris-flow event that occurred in the Cancia basin on 23 July 2015. The simulations with and without bed entrainment are conducted to investigate the influence of this process on the runout behavior of the debris flow. Results show that the actual runout can be reproduced only by considering bed entrainment. If entrainment is not taken into account, part of the debris mass deviates from the main path and both models predict unrealistic bank overflows not observed in the field. In addition, both models with entrainment performed reasonably well, giving satisfactory accuracy of the final erosion-deposit distribution, inundation area, and run-out distance comparing with the survey measurements, but some noticeable differences occurred in two models because using different numeric codes will show different results, even when modeling the same case. For the analyzed case, the DAN3D code always gives higher mobility and larger lateral spreading relative to the Shen model, while Shen's model reproduces relatively thicker deposits.

1.5.2 Influence of slope gradient and gully channel on the run-out and entrainment of a rockslide-debris flow

A recent rockslide-debris flow that occurred in the Northern Apennines of Italy was reconstructed using an improved depth-averaged model. The influence of slope gradient and gully channel on the entrainment, deposition, and run-out behavior of Verghereto rockslide-debris flow was numerically analyzed. The simulated run-out, entrainment and deposition characteristic of this landslide by adopting different basal friction strengths for the rockslide region and debris flow region agreed well with the field data of entrainment and deposition distributions, indicating that the depth-averaged model can reasonably simulate the run-out, entrainment and deposition processes of this type of landslides. Entrainment occurs in both high and low slope gradient zones. However, entrainment can only be observed in the high slope gradient zones, while in the low gradient zones, the post-failure topography shows accumulation and deposition. Moreover, the simulation results also demonstrate that the presence of a gully channel is a key factor in determining landslide mobility and run-out

distance. Compared to a landslide with similar size and geological settings but without a gully channel, the run-out distance is much less, and the landslide does not develop into a flow.

2. Basic theory of SPH method

Smoothed particle hydrodynamics (SPH) is a Lagrangian and mesh-less method and was originally proposed to solve astrophysics problems (Gingold and Monaghan, 1977; Lucy, 1977). Since then, it has been widely extended to various disciplines such as ballistics, volcanology, oceanography and fluid dynamics (Altomare et al., 2020; Dai et al., 2014; Frissane et al., 2019; Hérault et al., 2011; Libersky et al., 1993a; Monaghan, 1994, 1988; Randles and Libersky, 1996; Swegle and Attaway, 1995). More importantly, this method has recently been applied in the field of geomechanics to analyze some complex large deformation issues (Bui et al., 2008; Chen et al., 2013; Huang and Dai, 2014; Pastor et al., 2009; Peng et al., 2015).

DualSPHysics is an open-access Smoothed Particle Hydrodynamics code based on the SPH model named SPHysics (www.sphysics.org). SPHysics is developed to study the free-surface flow phenomena where Eulerian methods can be difficult to apply, such as waves, impact of dam-breaks on off-shore structures. DualSPHysics is available to download from www.dual.sphysics.org. This software is implemented in C++ and CUDA and is designed to execute code either on multiple CPUs using OpenMP or on a GPU. The GPU version of DualSPHysics implements optimal parallelization to maximize speedup during particle interaction calculation (Fig. 2.1).
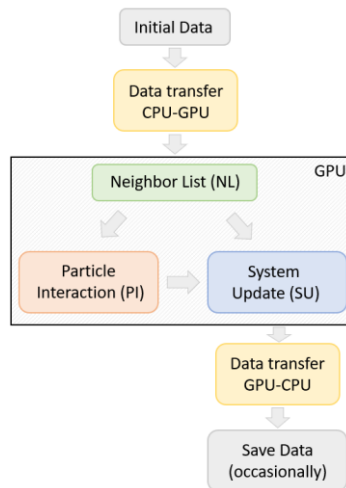
Fig. 2.1 Conceptual diagram of the GPU implementation of DualSPHysics code

2.1 Interpolations

In the SPH frame, the flow materials are discretized as a series of disordered particles. All physical quantities, such as position, velocity, density and pressure, can be estimated using an interpolation method. The integral approximation of any field function in the support domain is defined by:

$$\langle f(\boldsymbol{r})\rangle = \int_{\Omega} f(\boldsymbol{r}')W(\boldsymbol{r}-\boldsymbol{r}',h)d\boldsymbol{r}' \tag{2.1}$$

where the $\langle \cdot \rangle$ bracket denotes an approximation, Ω is the support domain. $\boldsymbol{r}$ and $\boldsymbol{r}'$ are the position vectors, h is the smoothing length determined by the distance of particles dp, which indicates the influence scales of the kernel function. W is the interpolating kernel, which integrates to unity across the support domain in each case (Fig. 2.2).

$$\int_{\Omega} W(\boldsymbol{r}-\boldsymbol{r}',h)d\boldsymbol{r}' = 1 \tag{2.2}$$

In addition, the kernel converges to a Dirac delta function around the particles considered when the smoothing length approaches zero.

$$\lim_{h\to 0} W(\boldsymbol{r}-\boldsymbol{r}',h)d\boldsymbol{r}' = \delta(\boldsymbol{r}-\boldsymbol{r}') \tag{2.3}$$

Eq. (2.1) is further approximated by summarizing the contributions from the neighboring particles in the support domain.

$$\langle f(\boldsymbol{r}_i)\rangle = \sum_{j=1}^{N} \frac{m_j}{\rho_j} f(\boldsymbol{r}_j)W(\boldsymbol{r}_i-\boldsymbol{r}_j,h) \tag{2.4}$$

where $\boldsymbol{r}_i$ and $\boldsymbol{r}_j$ are the position of particles i, and j, m_j and ρ_j are the mass and density of particle j, respectively, N is the total number of particles, and $j = 1$ to N are particles located within the support domain, which depends on the chosen kernel and its smoothing length. Significantly, the derivative form of Eq. (2.4) is obtained by ordinary differentiation of the interpolating kernel.

$$\langle \nabla \cdot f(\boldsymbol{r}_i)\rangle = \sum_{j=1}^{N} \frac{m_j}{\rho_j} f(\boldsymbol{r}_j)\nabla_i W(\boldsymbol{r}_i-\boldsymbol{r}_j,h) \tag{2.5}$$
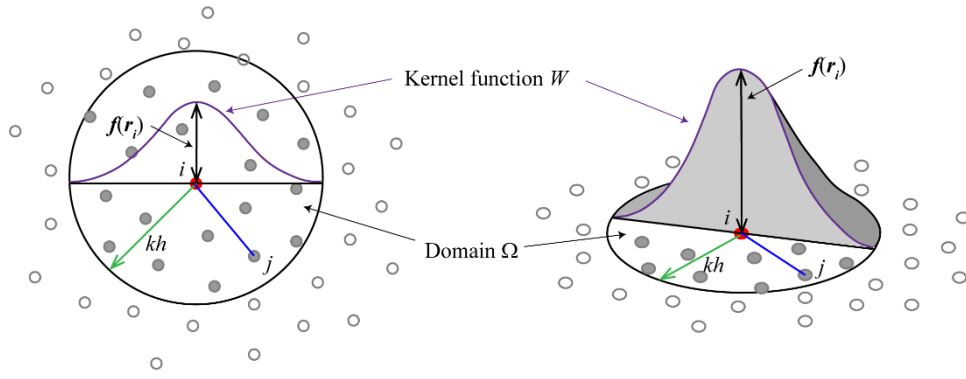
Fig. 2.2 Shape and compact support of the kernel function

2.2 Kernel functions

The choice of kernel function W has a significant impact on the performance of the SPH model. Two smoothing kernels, Cubic Spline and Quintic Wendland (Wendland, 1995), have been implemented in Dualsphysics. Kernels are expressed as a function of the non-dimensional distance between particles (q), given by $q = r/h$, where r is the distance between any given particles i and j, and the smoothing length h controls the size of the around particle i in which neighboring particles are considered.

(i) Cubic Spline

$$W(r,h) = \alpha_D \begin{cases} 1 - \frac{3}{2}q^2 + \frac{3}{4}q^3 & 0 \leq q \leq 1 \\ \frac{1}{4}(2-q)^3 & 1 \leq q \leq 2 \\ 0 & q \geq 2 \end{cases} \tag{2.6}$$

where α_D is equal to $10/7\pi h^2$ in 2D and $1/\pi h^3$ in 3D. The shape of this function and its derivative is shown in Fig. 2.3.
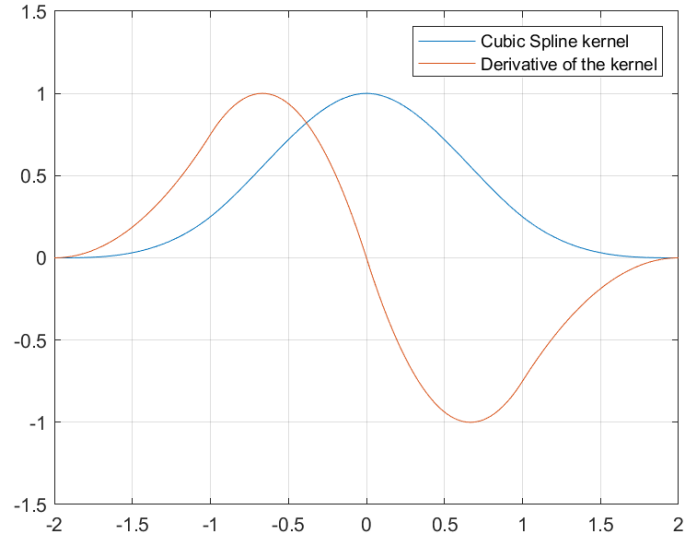
Fig. 2.3 Cubic Spline kernel and its derivative divided by the dimensional factor α_D

Note that the tensile correction method (Monaghan, 2000) is only activated in the cases of a kernel whose first derivative goes to zero with the particle distance q.

(ii) Quintic Wendland

$$W(r,h) = \alpha_D\left(1 - \frac{q}{2}\right)^4 (2q + 1) \quad 0 \le q \le 2 \tag{2.7}$$

where α_D is $7/4\pi h^2$ and $21/16\pi h^3$ in 2D and 3D, respectively. The shape of this function and its derivative is shown in Fig. 2.4.
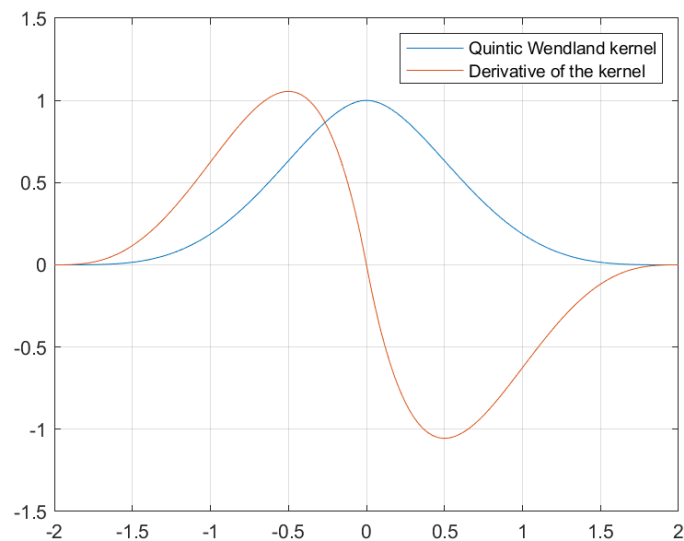
Fig. 2.4 Quintic Wendland kernel and its derivative divided by the dimensional factor α_D

2.3 Governing equation

In the SPH framework, the fluid is usually described as a weakly compressible material. By employing the Einstein summation notation, the mass and momentum conservation equations in Lagrangian form can be written as

$$\frac{d\rho}{dt} = -\rho \nabla \cdot \boldsymbol{v} + D \tag{2.8}$$

$$\frac{d\boldsymbol{v}}{dt} = -\frac{1}{\rho} \nabla P + \boldsymbol{g} + \Gamma \tag{2.9}$$

where ∇ is the vector differential operator, Γ refers to dissipative terms, v is velocity of the fluid particles, ρ is density, g is the gravity acceleration, P is the isotropic hydrostatic pressure, which can be determined adopting the equation of state (Fourtakas and Rogers, 2016; Gray et al., 2001), as expressed in the following equation:

$$P = \frac{c_s^2 \rho_0}{\gamma} \left[\left(\frac{\rho}{\rho_0} \right)^\gamma - 1 \right] \tag{10}$$

where ρ_0 is the reference density, which is 1000 kg/m^3 for the water. C_s is the speed of sound estimated by $\beta \sqrt{g h_{max}}$, and the recommended value of the constant β is 10 (Marrone et al., 2013; Monaghan, 2000), γ is a dimensionless constant that is generally suggested to be 7 (Monaghan, 2000).

In Section 2.4 and 2.5, a brief introduction is given to the different options for density diffusion term D and momentum dissipation Γ available in DualSPHysics, respectively.

2.4 Density diffusion terms

Different density diffusion terms (DDT) formulations are available in DualSPHysics to stabilize the density field from high-frequency oscillations. These terms take the general form of

$$D_i = \delta h c_a \sum_{j=1}^{N} \psi_{ij} \cdot \nabla_i W_{ij} V_j \tag{2.11}$$

where $c_a = 0.5(c_i + c_j)$ and δ is the delta-SPH coefficient, which controls the magnitude of the diffusion term. The term ψ_{ij} is based on the Neumann–Richtmeyer artificial dissipation. And the artificial DDT (Molteni and Colagrossi, 2009) is given by:

$$\psi_{ij} = 2(\rho_j - \rho_i)\frac{r_{ij}}{\|r_{ij}\|^2} \tag{2.12}$$

Lately, the correction of Eq. (2.12) is developed by accounting for the dynamic component of the density (Fourtakas et al., 2019). Thus, the term ψ_{ij} can be expressed as:

$$\psi_{ij} = 2(\rho_{ji}^T - \rho_{ij}^H)\frac{r_{ij}}{\|r_{ij}\|^2} \tag{2.13}$$

where superscripts T and H denote the total and hydrostatic component of the density of a weakly compressible fluid. Eq. (2.10) links the density to the total pressure at the particle location. Thus, only hydrostatic pressure is needed. According to Eq. (2.10), the hydrostatic density difference takes the following form:

$$\rho_{ij}^H = \rho_0 \left(\sqrt[\gamma]{\frac{\rho_0 g z_{ij} + 1}{c_s^2 \rho_0 / \gamma}} - 1\right) \tag{2.14}$$

where z_{ij} is the vertical distance between particle i and j.

Compared with artificial diffusive terms (Eq. (2.12)), Eq. (2.13) improves the behavior of pressure near the wall boundaries, which avoids computing the normalized density gradient.

2.5 Momentum dissipation terms

2.5.1 Artificial viscosity

The artificial viscosity proposed by Monaghan (1992) has been used frequently to reduce oscillations and stabilize the SPH scheme due to its simplicity. In SPH notation, Eq. (2.9) can be written as:

$$\frac{dv_i}{dt} = -\sum_{j=1}^{N} m_j \left(\frac{P_i}{\rho_i^2} + \frac{P_j}{\rho_j^2} + \Pi_{ij}\right)\nabla_i W_{ij} + g \tag{2.15}$$

where i represents the index of the concerning particle, j is the index of the neighboring particles of particle i, and W_{ij} is the simplified expression of $W(r_i - r_j, h)$. P denotes the pressure of fluid

particles and the artificial viscosity term Π_{ij} is given by:

$$\Pi_{ij} = \begin{cases} \dfrac{-\alpha \overline{c_{ij}} \mu_{ij}}{\overline{\rho_{ij}}} & v_{ij} \cdot r_{ij} < 0 \\ 0 & v_{ij} \cdot r_{ij} \geq 0 \end{cases} \tag{2.16}$$

with

$$\mu_{ij} = \frac{h v_{ij} \cdot r_{ij}}{r_{ij}^2 + \eta^2} \tag{2.17}$$

where $\mathbf{v}_{ij} = \mathbf{v}_i - \mathbf{v}_j$ and $\mathbf{r}_{ij} = \mathbf{r}_i - \mathbf{r}_j$ denote the velocity and position vector, respectively. α is the artificial viscosity coefficient that needs to be adjusted for each case. $\overline{c_{ij}} = (c_i + c_j)/2$ and $\overline{\rho_{ij}} = (\rho_i + \rho_j)/2$ are the mean speed of sound and the mean density, respectively. And the parameter $\eta^2 = 0.01h^2$ is adopted to avoid numerical divergence when the distance between particles tends to zero.

2.5.2 Laminar viscosity and Sub-Particle Scale (SPS) turbulence

Alternatively, laminar viscous stress in the momentum equation is expressed as (Lo and Shao, 2002; Morris et al., 1997):

$$v_0 \nabla^2 \mathbf{v}_i = \sum_{j=1}^{N} m_j \frac{4v_0 r_{ij} \cdot \nabla_i W_{ij}}{(\rho_i + \rho_j)(r_{ij}^2 + \eta^2)} \mathbf{v}_{ij} \tag{2.18}$$

where v_0 is the kinetic viscosity (typically 10^{-6} m^{2}s for water).

The concept of the Sub-Particle Scale (SPS) was first described by Gotoh et al., (2001) to represent the effects of turbulence in their moving particle semi-implicit model. The momentum conservation equation (Eq. (2.9)) can be re-written as:

$$\frac{d\mathbf{v}}{dt} = -\frac{1}{\rho} \nabla P + \mathbf{g} + v_0 \nabla^2 \mathbf{v} + \frac{1}{\rho} \nabla \cdot \vec{\tau} \tag{2.19}$$

where the third term on the right-hand side of Eq. (2.19) can be treated following Eq. (2.18) and $\vec{\tau}$ represents the SPS stress tensor and Favre-averaging is needed to account for compressibility in weakly compressible SPH (Dalrymple and Rogers, 2006) where an eddy viscosity assumption is used to model the sub-particle tensor with Einstein notation for the shear stress component in directions x and y according to:

$$\frac{\bar{\tau}_{xy}}{\rho} = 2\nu_t \left(S_{xy} - \frac{1}{3}S_{xy}\delta_{xy}\right) - \frac{2}{3}C_I \Delta l^2 \delta_{xy}|S_{xy}|^2 \qquad (2.20)$$

where the turbulence eddy viscosity $\nu_t = [C_s\Delta l]^2|S|$ and $C_I = 0.0066$, the Smagorinsky constant $C_{sps} = 0.12$, Δl is the initial particle spacing, and the local strain rate $|S| = 0.5\left(2S_{xy}S_{xy}\right)^{1/2}$, where S_{xy} is an element of the SPS strain tensor. Finally, adopting the same variationally consistent form of the pressure gradient (Eq. (2.11)), the dissipation term Γ in DualSPHysics takes the following form:

$$\Gamma_i = \sum_{j=1}^{N} m_j \frac{4\nu_0 r_{ij} \cdot \nabla_i W_{ij}}{(\rho_i + \rho_j)(r_{ij}^2 + \eta^2)}\boldsymbol{v}_{ij} + \sum_{j=1}^{N} m_j \left(\frac{(\tau_{xy})_i}{\rho_i^2} + \frac{(\tau_{xy})_j}{\rho_j^2}\right)\nabla_i W_{ij} \qquad (2.21)$$

2.6 Time integration algorithms

The physical magnitudes (velocity, density, pressure and position) vary at every time step due to the particle interaction. Two explicit numerical integration schemes (Verlet and Symplectic algorithms) are implemented in DualSPHysics. For brevity, the governing equations are written as

$$\begin{aligned} \frac{d\boldsymbol{v}_i}{dt} &= \boldsymbol{F}_i \\ \frac{d\rho_i}{dt} &= R_i \\ \frac{d\boldsymbol{r}_i}{dt} &= \boldsymbol{v}_i \end{aligned} \qquad (2.22)$$

2.6.1 Verlet algorithm

Verlet time integrating algorithm is widely used in molecular dynamics (Verlet, 1967). It is a second-order accurate space integrator, providing a low computational cost compared to other integration techniques, mainly because it does not require multiple calculations for each step. Verlet time stepping algorithm is generally split into two parts. Variables are firstly calculated by:

$$\begin{aligned} \rho_i^{n+1} &= \rho_i^{n-1} + 2\Delta t R_i^n \\ \boldsymbol{v}_i^{n+1} &= \boldsymbol{v}_i^{n-1} + 2\Delta t \boldsymbol{F}_i^n \\ \boldsymbol{r}_i^{n+1} &= \boldsymbol{r}_i^n + \Delta t \boldsymbol{v}_i^n + 0.5\Delta t^2 \boldsymbol{F}_i^n \end{aligned} \qquad (2.23)$$

where R_i^n and $\boldsymbol{F}_i^n$ are calculated by Eq. (2.8) and Eq. (2.9), respectively.

Furthermore, the density and velocity equations are decoupled due to the integration over a staggered

time interval. Therefore, an intermediate step is required every N_S steps ($N_S \approx 40$ is suggested) to avoid the divergence of the integrated values, variables are calculated according to

$$\rho_i^{n+1} = \rho_i^n + \Delta t R_i^n$$
$$\boldsymbol{v}_i^{n+1} = \boldsymbol{v}_i^n + \Delta t \boldsymbol{F}_i^n \qquad (2.24)$$
$$\boldsymbol{r}_i^{n+1} = \boldsymbol{r}_i^n + \Delta t \boldsymbol{v}_i^n + 0.5\Delta t^2 \boldsymbol{F}_i^n$$

where the superscript $n \in \mathbb{N}$ and Δt denotes the time step and $t = n\Delta t$.

2.6.2 Symplectic algorithm

Symplectic time integration scheme implemented in DualSPHysics is an explicit second-order algorithm with a predictor and corrector stage (Domínguez et al., 2021).

During the predictor stage, the values of density, velocity and position are estimated at the middle of the time step according to

$$\rho_i^{n+\frac{1}{2}} = \rho_i^n + \frac{\Delta t}{2} R_i^n$$
$$\boldsymbol{v}_i^{n+\frac{1}{2}} = \boldsymbol{v}_i^n + \frac{\Delta t}{2} \boldsymbol{F}_i^n \qquad (2.25)$$
$$\boldsymbol{r}_i^{n+\frac{1}{2}} = \boldsymbol{r}_i^n + \frac{\Delta t}{2} \boldsymbol{v}_i^n$$

Dring the corrector stage, $R_i^{n+\frac{1}{2}}$ and $\boldsymbol{F}_i^{n+\frac{1}{2}}$ are used to calculate the corrected density and velocity, respectively. Position of the particle at the end of the time step can be estimated according to

$$\rho_i^{n+1} = \rho_i^n \frac{2-\varepsilon_i^{n+\frac{1}{2}}}{2+\varepsilon_i^{n+\frac{1}{2}}}$$
$$\boldsymbol{v}_i^{n+1} = \boldsymbol{v}_i^n + \Delta t \boldsymbol{F}_i^{n+\frac{1}{2}} \qquad (2.26)$$
$$\boldsymbol{r}_i^{n+1} = \boldsymbol{r}_i^n + \Delta t \frac{\boldsymbol{v}_i^{n+1}+\boldsymbol{v}_i^n}{2}$$

where $\varepsilon_i^{n+\frac{1}{2}} = -\left(R_i^{n+\frac{1}{2}}/\rho_i^{n+\frac{1}{2}}\right)\Delta t$.

2.6.3 Variable time step

Generally, the time step in the explicit time integrating schemes is strongly dependent on the Courant-Friedric-Levy (CFL) condition, the force terms and the viscous diffusion term. A variable time step Δt is calculated according to (Monaghan and Kos, 1999):

$$
\begin{aligned}
\Delta t &= C_{cfl} min\left(\Delta t_f, \Delta t_{cv}\right) \\
\Delta t_f &= \min_i\left(\sqrt{h/|d\boldsymbol{v}_i/dt|}\right) \\
\Delta t_{cv} &= \min_i \frac{h}{C_f + \max_j\left|h\boldsymbol{v}_{ij}\cdot\boldsymbol{r}_{ij}/\left(r_{ij}^2 + \eta^2\right)\right|}
\end{aligned}
\tag{2.27}
$$

where Δt_f is based on the force per unit of mass $|d\boldsymbol{v}_i/dt|$ and Δt_{cv} combines the Courant-Friedric-Levy condition and the viscosity of the system. $|d\boldsymbol{v}_i/dt|$ is the magnitude of particle acceleration, the speed of sound in fluid $C_f = \max\left(C_s, 10|v|_{max}\right)$, where $|v|_{max}$ is the maximum velocity of fluid particles. CFL number C_{cfl} is a constant that can vary between 0.1 and 0.2.

2.7 Boundary conditions

DualSPHysics currently provides two boundary treatments (Dynamic Boundary Conditions and Modified Dynamic Boundary Conditions) for solid boundaries. Both boundary conditions treat the solid boundaries as a series of boundary particles $a \in B$ that differ from the fluid particles F (Domínguez et al., 2021).

2.7.1 Dynamic boundary conditions (DBCs)

The default boundary condition in DualSPHysics Dynamic Boundary Conditions (DBCs) is simply represented by boundary particles that satisfy the same continuity equation as fluid particles. However, these boundary particles remain either fixed in position to approximate the non-slip boundary condition or move according to the user-defined movement functions. More details can be found in (Crespo et al., 2007).

The repulsion mechanism of this method is briefly summarized as follows: when a fluid particle approaches a boundary and the distance between them becomes smaller than k times the smooth length (kh), the density of the affected boundary particles increases, resulting in a pressure increase according to the equation of state. In consequence, this increase in pressure will lead to an increase in the acceleration magnitude for the fluid particle approaching the boundary, which defines the repulsion force.

This type of boundary condition is easy to set up and has low computational cost because the calculation of density and pressure of boundary particles can be conducted within the same loops as fluid particles. Additionally, complex 3D geometry can be represented using DBCs. However, an unphysical gap between the fluid and boundary particles appears, decreasing the accuracy of pressures measured on the boundary. Therefore, modified dynamic boundary conditions (MDBCs) are proposed to avoid the limitation of DBCs.

2.7.2 Modified dynamic boundary conditions (MDBCs)

MDBCs are developed by (English et al., 2022). The boundary particles of MDBCs are arranged in the same way as the boundary particles in the original DBCs. Note that an additional boundary interface is created for the projection of boundary particles, located half a particle spacing ($dp/2$) from the layer of boundary particles closest to the fluid. For each boundary particle, a ghost node is projected into the fluid across a boundary interface, similarly as the procedure employed by Marrone et al., (2011). Herein, two types of ghost node mirroring approaches are considered due to the different locations of boundary particles (Fig. 2.5). Fluid properties are then calculated at the ghost node through a first-order consistent SPH spatial interpolation over the surrounding fluid particles only (Liu and Liu, 2006) and finally mirrored back to the boundary particles.
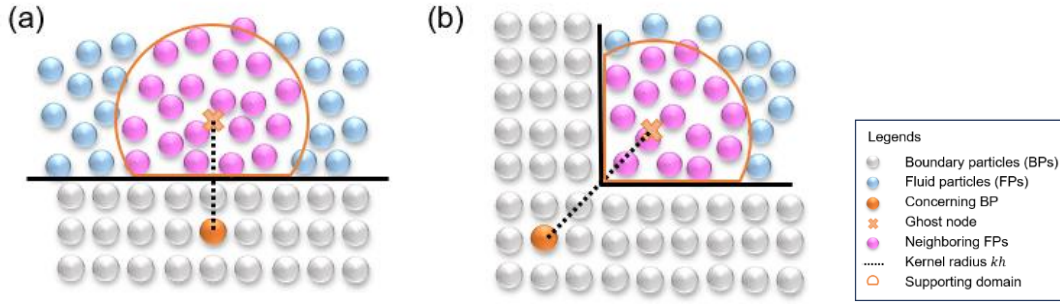
Fig. 2.5 Schematic diagram of ghost node mirroring methods for boundary particles in (**a**) a flat interface and (**b**) a corner

2.8 Algorithm workflow

In summary, DualSPHysics software works in the following ways (Fig. 2.6). The main loop consists of three main steps: (i) solving governing equations, (ii) considering boundary conditions and (iii) integrating in time to update all the physical properties of the particles in the system.
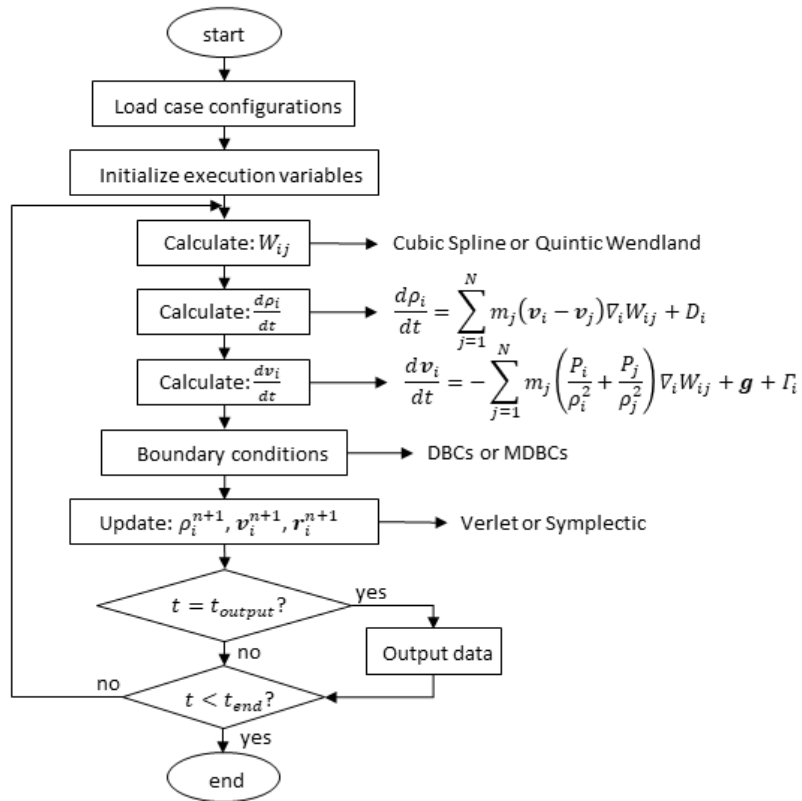
Fig. 2.6 Flowchart of DualSPHysics code implementation

3. Failure patterns of roto-translational sliding

Slope failures occur when driving forces overcome resisting forces. The driving force is typically gravity, and the resisting force is the slope material's shear strength. It can result in various types of movements, including slides, falls, flows, creep, and complex combinations of these movements. Understanding the contributing factors and mechanisms of slope failure is essential for effective risk assessment, mitigation planning, and sustainable land use practices in areas prone to these natural events. Engineers and geoscientists adopt various methods, including slope stability analysis, in-site monitoring, and numerical simulation, to assess and manage the potential for slope failure in different geographical settings. In this section, we focus on the failure mechanism of the roto-translational landslide.

3.1 Introduction

The roto-translational landslides are widely distributed all over the world (Michael, 2000; Xin et al., 2018; Yenes et al., 2015, 2009). They also occur frequently in the northeast margin of the Tibetan Plateau in China, resulting in catastrophic consequences to the nearby facilities and residents. For instance, in 1955 the Wolongsi landslide induced by heavy rainfall destroyed a railway, buried two villages, and caused tens of fatalities (Shi et al., 2013). In 2013, a landslide was reactivated in the Hongluo village, destroying the Lianhuo highway. In 2019, the Majiapo landslide at the upstream of the Wei River affected two villages, resulting in significant economic loss (Wang et al., 2020). Therefore, it is crucial to understand the mechanisms of roto-translational landslides to mitigate and prevent them.

A significant characteristic of these landslides is that multiple slip surfaces may form in the run-out process. The slip surface of this type of landslides is combined by a rotational slip surface and a translational slip surface (Xin et al., 2018; Yenes et al., 2009). Great efforts have been made to study the failure mechanisms of the roto-translational landslides (Bentley et al., 2023; Dey et al.,

2015; Kennedy et al., 2021; Kohv et al., 2010; Liu et al., 2019; Locat et al., 2013, 2011; Luo and Zhang, 2016; Quinn et al., 2012; Sun et al., 2022; Xu et al., 2014; Zhang et al., 2017, 2019). Many researchers adopted on-site monitoring approaches to record the progressive failure process of these landslides (Bentley et al., 2023; Kohv et al., 2010). However, filed monitoring fails in capturing the minor changes in the sliding body that may develop during the failure process. Alternatively, some physical model tests were carried out to reproduce the failure process of these landslides (Kennedy et al., 2021; Sun et al., 2022). Although these tests are able to obtain and analyze various field variables such as stress, strain, velocity, displacement, etc., they are costly and have poor repeatability. By contrast, numerical modeling has become a good choice to analyze the failure and run-out process of roto-translational landslides due to the rapid development in computational technology in recent decades. Among the numerical models for simulating landslides, the models based on particle methods such as the material particle method (MPM) (Liu et al., 2019; Vardon et al., 2017; Wang et al., 2016), smoothed particle finite element method (SPFEM) (Jin et al., 2020a, 2020b; Yuan et al., 2020), particle finite element method (PFEM) (Zhang et al., 2020, 2017) and smoothed particle hydrodynamics (SPH) (Bui et al., 2011; Bui and Nguyen, 2021; Nonoyama et al., 2015; Zhang et al., 2019) are becoming increasingly popular. The SPH is adopted in this study due to its advantages in dealing with the large deformation problem with complex boundary conditions.

To reproduce the mechanical behavior of soils involved in the roto-translational landslides, it is very important to incorporate suitable constitutive laws into the numerical model. The viscous-plastic (Han et al., 2019; Qiao et al., 2023; Yang et al., 2020) and the elastic-plastic (Bui et al., 2008; Chen and Qiu, 2012; Deb and Pramanik, 2013; Liang et al., 2020) are two widely used constitutive laws in SPH simulations. The viscous-plastic law adopts Bingham, HBP or $\mu(I)$ models to describe the rheological behavior of flow materials, which is mainly suitable for modeling viscous-plastic flows that are strain history-independent. While for modeling strain history-dependent materials such as cohesive soils in this study, the elastic-plastic constitutive law is more appropriate. To the best of our knowledge, few existing works have considered the strain softening in the elastic-plastic constitutive law in the SPH framework, and the previous studies mainly focused on the progressive

failure of ideal slopes, with very limited applications to real roto-translational landslides. Therefore, in this research, I propose a modified SPH model by embedding a strain softening elastic-plastic constitutive law into the original open source SPH code: DualSPHysics (Crespo et al., 2015). Two benchmark cases are used to validate the proposed model, and the Caijiapo landslide that occurred in Qishan County, Shaanxi Province, China is analyzed to reveal the progressive failure mechanism of this landslide.

3.2 Methodology

3.2.1 Governing Equations

In the SPH framework, the landslide mass is usually described as a weakly compressible material (Dai et al., 2014; Fourtakas and Rogers, 2016; He et al., 2018; Liang et al., 2020; C. Wang et al., 2021). By employing the Einstein summation notation, the mass and momentum conservation equations in Lagrangian form can be written as

$$\frac{d\rho}{dt} = -\rho \frac{\partial v^\alpha}{\partial x^\alpha} \tag{3.1}$$

$$\frac{dv^\alpha}{dt} = -\frac{1}{\rho} \frac{\partial \sigma^{\alpha\beta}}{\partial x^\beta} + g^\alpha \tag{3.2}$$

where the Greek subscripts α and β (=1, 2 or 3) stands for the Cartesian components x, y and z by employing the Einstein summation notation. v is the velocity vector of the soil particles, ρ is the density of the soil particles, g is the gravity acceleration. σ donates the Cauchy stress, which can be written as:

$$\sigma^{\alpha\beta} = -p\delta^{\alpha\beta} + s^{\alpha\beta} \tag{3.3}$$

where p is the isotropic hydrostatic pressure, s is the deviatoric shear stress, and δ is the Kronecker's delta. p can be calculated through two approaches either by adopting the equation of state (Eq. (2.10)) (Fourtakas and Rogers, 2016; Gray et al., 2001) and soil constitutive equation (Bui et al., 2008; Chen and Qiu, 2012). In our study, p is derived directly from the soil constitutive equation and can be expressed as

$$p = -\frac{1}{3}\sigma^{\alpha\alpha} \tag{3.4}$$

3.2.2 Constitutive model

In this section, the ideal elastic-plastic constitutive law is implemented in the original SPH model first. To reproduce the progressive failure process of the roto-translational landslides, a strain softening elastic-plastic constitutive law is then incorporated into the SPH framework.

3.2.2.1 Constitutive equation

The strain rate tensor $\dot{\varepsilon}^{\alpha\beta}$ can be written as:

$$\dot{\varepsilon}^{\alpha\beta} = \frac{1}{2}\left(\frac{\partial v^\alpha}{\partial x^\beta} + \frac{\partial v^\beta}{\partial x^\alpha}\right) \tag{3.5}$$

For an ideal elastic-plastic material, $\dot{\varepsilon}^{\alpha\beta}$ can be written in the following form:

$$
\begin{aligned}
\dot{\varepsilon}^{\alpha\beta} &= \dot{\varepsilon}_e^{\alpha\beta} + \dot{\varepsilon}_p^{\alpha\beta} \\
\dot{\varepsilon}_e^{\alpha\beta} &= \frac{\dot{s}^{\alpha\beta}}{2G} + \frac{\dot{\sigma}^{\gamma\gamma}\delta^{\alpha\beta}}{9K} \\
\dot{\varepsilon}_p^{\alpha\beta} &= \dot{\lambda}\frac{\partial g}{\partial \sigma^{\alpha\beta}}
\end{aligned}
\tag{3.6}
$$

where $\dot{\lambda}$ is the rate of plastic multiplier λ, g is the plastic potential function, $\dot{\sigma}^{\gamma\gamma}$ is the sum of the three normal stress rate components, G and K are the shear modulus and the elastic bulk modulus, respectively. G and K can be represented by Poisson's ratio v and Young's modulus E as:

$$G = \frac{E}{2(1+v)} \text{ and } K = \frac{E}{3(1-2v)} \tag{3.7}$$

After rearranging Eq. (3.6), the general stress-strain relationship for the elastic-plastic material is given by:

$$\dot{\sigma}^{\alpha\beta} = 2G\dot{\varepsilon}^{\alpha\beta} + \left(K - \frac{2G}{3}\right)\dot{\varepsilon}^{\gamma\gamma}\delta^{\alpha\beta} - \dot{\lambda}\left[\left(K - \frac{2G}{3}\right)\frac{\partial g}{\partial \sigma^{mn}}\delta^{mn}\delta^{\alpha\beta} + 2G\frac{\partial g}{\partial \sigma^{\alpha\beta}}\right] \tag{3.8}$$

where α and β are free indexes, m and n are dummy indexes, $\dot{\varepsilon}^{\gamma\gamma}$ is the volumetric strain, and the rate of plastic multiplier $\dot{\lambda}$ is calculated by the following equation:

$$\dot{\lambda} = \frac{2G\dot{\varepsilon}^{\alpha\beta}\frac{\partial f}{\partial \sigma^{\alpha\beta}} + \left(K - \frac{2G}{3}\right)\dot{\varepsilon}^{\gamma\gamma}\frac{\partial f}{\partial \sigma^{\alpha\beta}}\delta^{\alpha\beta}}{2G\frac{\partial f}{\partial \sigma^{mn}}\frac{\partial g}{\partial \sigma^{mn}} + \left(K - \frac{2G}{3}\right)\frac{\partial f}{\partial \sigma^{mn}}\delta^{mn}\frac{\partial g}{\partial \sigma^{mn}}\delta^{mn}} \tag{3.9}$$

where f denotes the plastic yield function, which is consistent with the plastic potential function g in the associated flow rule. However, the soil described in this study is generally considered to be a non-associated plastic material. The expressions of f and g are no longer the same, which will be presented in Section 3.2.2.2.

3.2.2.2 Yielding criterion

The Mohr-Coulomb model (Dai et al., 2014; Hu et al., 2015; Krimi et al., 2018) and Drucker-Prager (DP) model (Chen and Qiu, 2012; Peng et al., 2021) are the most widely used yield criteria for soil materials. The DP model with the non-associated flow rule is adopted in this work. The yield function f and the plastic potential function g are given as follows.

$$f(I_1, J_2) = \sqrt{J_2} + \alpha_\varphi I_1 - k_c = 0 \tag{3.10}$$

$$g(I_1, J_2) = \sqrt{J_2} + \sin \psi \, I_1 \tag{3.11}$$

where I_1 is the first invariant of the stress, J_2 is the second invariant of the deviatoric stress, ψ is the dilatancy angle, and α_φ and k_c are constants related to the internal friction angle φ and cohesion c:

$$\alpha_\varphi = \frac{\tan \varphi}{\sqrt{9 + 12 \tan \varphi \tan \varphi}} \; , \; k_c = \frac{3c}{\sqrt{9 + 12 \tan \varphi \tan \varphi}} \tag{3.12}$$

For large deformation of the soil, rigid body rotation (Libersky et al., 1993b) should be considered, and the relationship between stress rate and strain rate can be expressed in incremental form as:

$$\dot{\sigma}^{\alpha\beta} = 2G\dot{\varepsilon}^{\alpha\beta} + \left(K - \frac{2G}{3}\right)\dot{\varepsilon}^{\gamma\gamma}\delta^{\alpha\beta} - \dot{\lambda}\left(3K \sin \psi \, \delta^{\alpha\beta} + \frac{G}{\sqrt{J_2}}s^{\alpha\beta}\right) + \sigma^{\alpha\gamma}\dot{\omega}^{\beta\gamma} + \sigma^{\beta\gamma}\dot{\omega}^{\alpha\gamma} \tag{3.13}$$

where $\dot{\omega}$ is the rotation rate tensor, which can be written as

$$\dot{\omega}^{\alpha\beta} = \frac{1}{2}\left(\frac{\partial v^\alpha}{\partial x^\beta} - \frac{\partial v^\beta}{\partial x^\alpha}\right) \tag{3.14}$$

$\dot{\lambda}$ is determined by the following equation:

$$\dot{\lambda} = \frac{3\alpha_\varphi K \dot{\varepsilon}^{\gamma\gamma} + (G/\sqrt{J_2}) s^{\alpha\beta} \dot{\varepsilon}^{\alpha\beta}}{9\alpha_\varphi K \sin\psi + G} \tag{3.15}$$

To consider the strain-softening of soil, the strength parameters (c and φ in Eq. (12)) are determined by the following expressions (Zabala and Alonso, 2011):

$$\begin{aligned} \varphi(\bar{\varepsilon}^p) &= \varphi_r + (\varphi_p - \varphi_r) e^{-\eta\bar{\varepsilon}^p} \\ c(\bar{\varepsilon}^p) &= c_r + (c_p - c_r) e^{-\eta\bar{\varepsilon}^p} \end{aligned} \tag{3.16}$$

where the subscripts p and r refer to the peak and residual strength, respectively. η is the strain softening coefficient controlling the reduction of the shear strength, and $\bar{\varepsilon}^p$ is the equivalent plastic strain which can be represented by the deviatoric plastic strain rate tensor $\dot{e}_p^{\alpha\beta}$ as:

$$\bar{\varepsilon}^p = \sqrt{\frac{2}{3} \dot{e}_p^{\alpha\beta} \dot{e}_p^{\alpha\beta}} \tag{3.17}$$

The SPH discretization forms of Eqs. (3.1), (3.2) and (3.13) are given in the following expressions. They are the time-dependent variables and updated at each time step.

$$\frac{d\rho_i}{dt} = \sum_{j=1}^{N} m_j (v_i^\alpha - v_j^\alpha) \frac{\partial W_{ij}}{\partial x_i^\alpha}$$

$$\frac{dv_i^\alpha}{dt} = \sum_{j=1}^{N} m_j \left(\frac{\sigma_i^{\alpha\beta}}{\rho_i^2} + \frac{\sigma_j^{\alpha\beta}}{\rho_j^2} \right) \frac{\partial W_{ij}}{\partial x_i^\beta} + g^\alpha \tag{3.18}$$

$$\frac{d\sigma_i^{\alpha\beta}}{dt} = 2G\dot{\varepsilon}_i^{\alpha\beta} + \left(K - \frac{2G}{3} \right) \dot{\varepsilon}_i^{\gamma\gamma} \delta_i^{\alpha\beta} - \dot{\lambda}_i \left(3K \sin\psi \, \delta_i^{\alpha\beta} + \frac{G}{\sqrt{J_2}} s_i^{\alpha\beta} \right) + \sigma_i^{\alpha\gamma} \dot{\omega}_i^{\beta\gamma} + \sigma_i^{\beta\gamma} \dot{\omega}_i^{\alpha\gamma}$$

where i represents the index of the concerning particle, j is the index of a neighboring particle of particle i, W_{ij} is the kernel function. The strain and rotation rate tensor of particle i in Eq. (3.18) can be discretized as follows:

$$\dot{\varepsilon}_i^{\alpha\beta} = \frac{1}{2} \sum_{j=1}^{N} \left[\frac{m_j}{\rho_j} (v_j^\alpha - v_i^\alpha) \frac{\partial W_{ij}}{\partial x_i^\beta} + \frac{m_j}{\rho_j} (v_j^\beta - v_i^\beta) \frac{\partial W_{ij}}{\partial x_i^\alpha} \right]$$

$$\dot{\omega}_i^{\alpha\beta} = \frac{1}{2} \sum_{j=1}^{N} \left[\frac{m_j}{\rho_j} (v_j^\alpha - v_i^\alpha) \frac{\partial W_{ij}}{\partial x_i^\beta} - \frac{m_j}{\rho_j} (v_j^\beta - v_i^\beta) \frac{\partial W_{ij}}{\partial x_i^\alpha} \right] \tag{3.19}$$

3.2.3 Workflow of the developed SPH model

The calculation process of the developed SPH model considering soil constitutive relationship is shown in Fig. 3.1. Compared with the original DualSPHysics code (Fig. 2.6), a Crucial step ($d\sigma_i^{\alpha\beta}/dt$ calculation) is added into the main loop to model strain history-dependent materials such as cohesive soils. In this algorithm, three physical quantities (densityρ, velocity $\boldsymbol{v}$ and Cauchy stress $\boldsymbol{\sigma}$) are the time-dependent variables and updated at each time step.
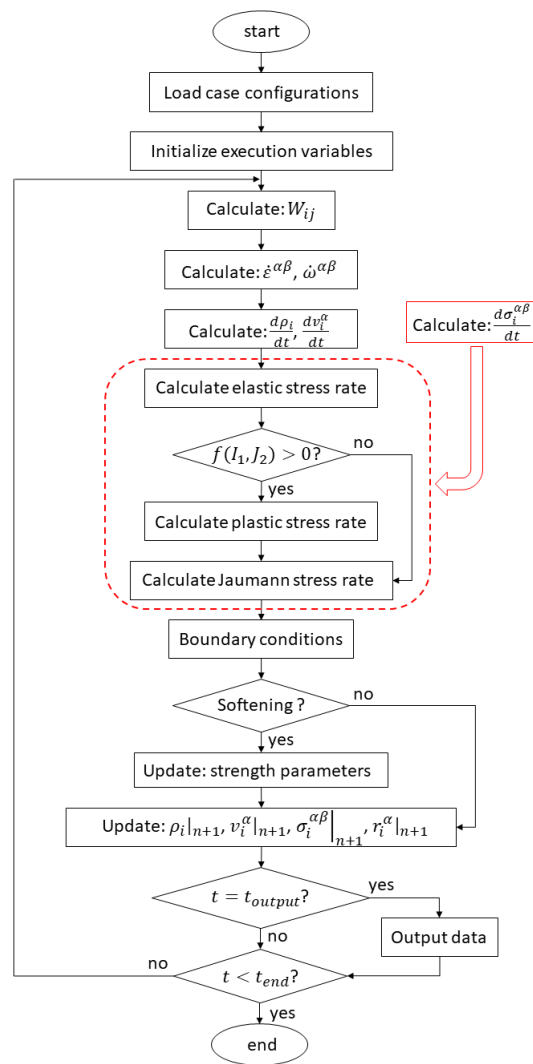

Fig. 3.1 Calculation process of the proposed SPH model

3.3 Model validation

In this section, two benchmark tests are carried out to validate the modified SPH model. The first one is the failure of a cohesive slope without strain softening. This numerical test is typically used to demonstrate the capability of the model in simulating the large deformation problem (Bui et al., 2011; Yuan et al., 2020). Subsequently, we carried out a strain softening clay slope failure test to verify the performance of the proposed model in depicting the progressive failure process of the roto-translational landslides.

3.3.1 Cohesive slope failure without strain softening

The DP model is adopted in simulating the failure process of the cohesive soil slope without strain softening. Fig. 3.2 shows the geometric and boundary configurations of this soil slope. In this simulation, the slope material is treated as a homogeneous cohesive soil and modeled by 11039 SPH particles with an initial particle distance of 0.2 m. The simulation parameters for this test are listed in Table 3.1.
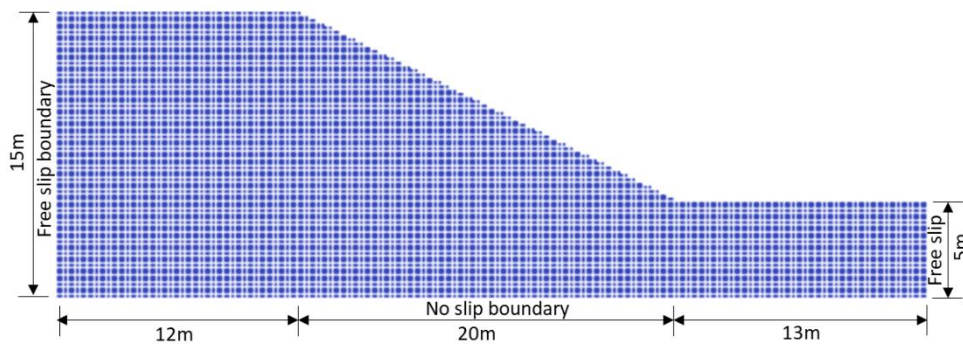

Fig. 3.2 Geometric and boundary configurations of a cohesive soil slope model

Table 3.1 Material properties for the cohesive soil slope analysis

Parameters	Value
Soil density (kg/m^3)	2040
Young's modulus (MPa)	100
Poisson's ratio	0.3

Internal friction angle (°)	20
Cohesion (kPa)	10
Dilatancy angle (°)	9

The shear strength reduction method (Eq. (3.20)) is applied to search the slip surface (Griffiths and Lane, 1999). The gravity force is imposed on all particles to obtain the initial stress condition, and then the simulations using a series of strength reduction factors (SRFs) are analyzed until the occurrence of slope failure.

$$c_r = c_0/SRF$$
$$\varphi_r = tan^{-1}(tan\,\varphi_0/SRF)$$
(3.20)

where c_0 and φ_0 are the initial cohesion and friction angle, respectively, c_r and φ_r are the reduced cohesion and friction angle, respectively. As the increase of SRF, the slope gradually becomes unstable, plastic deformation develops and slope failure occurs. The critical value of SRF, namely the safety factor of slope (FOS), is obtained when a shear band is fully developed in the slope.

Fig. 3.3 illustrates the evolution of the shear band with increasing SRF. For SRF=1.3, the plastic strain only develops at the slope toe and the slope soon stabilizes again. In this case, the slope is subjected to local failure rather than global failure. When SRF increases to 1.35, the shear band extends from the slope toe to the upper part of the slope and stops beneath the crest of the slope. As shown in Fig. 3.3c and 3d, when SRF approaches 1.4, the circular shear bands are fully developed, resulting in the global failure of slope. The simulated failure surface is in line with that obtained by the limit equilibrium method (Bishop's circle). However, the shear band of Fig. 3.3d is clearer than that observed in Fig. 3.3c, which indicates that the failure has not been completed yet in the simulation with SRF=1.38. Therefore, the critical SRF in our SPH model is 1.4, which is basically consistent with the results of FEM analysis (FOS=1.4) and the limit equilibrium analysis (FOS=1.37). According to the above analysis, the progressive failure process of a cohesive slope can be summarized as follows: the soil particles at the slope toe yield first, and then the soil particles next to these weakened particles begin to yield. Eventually, the entire failure surface is formed.
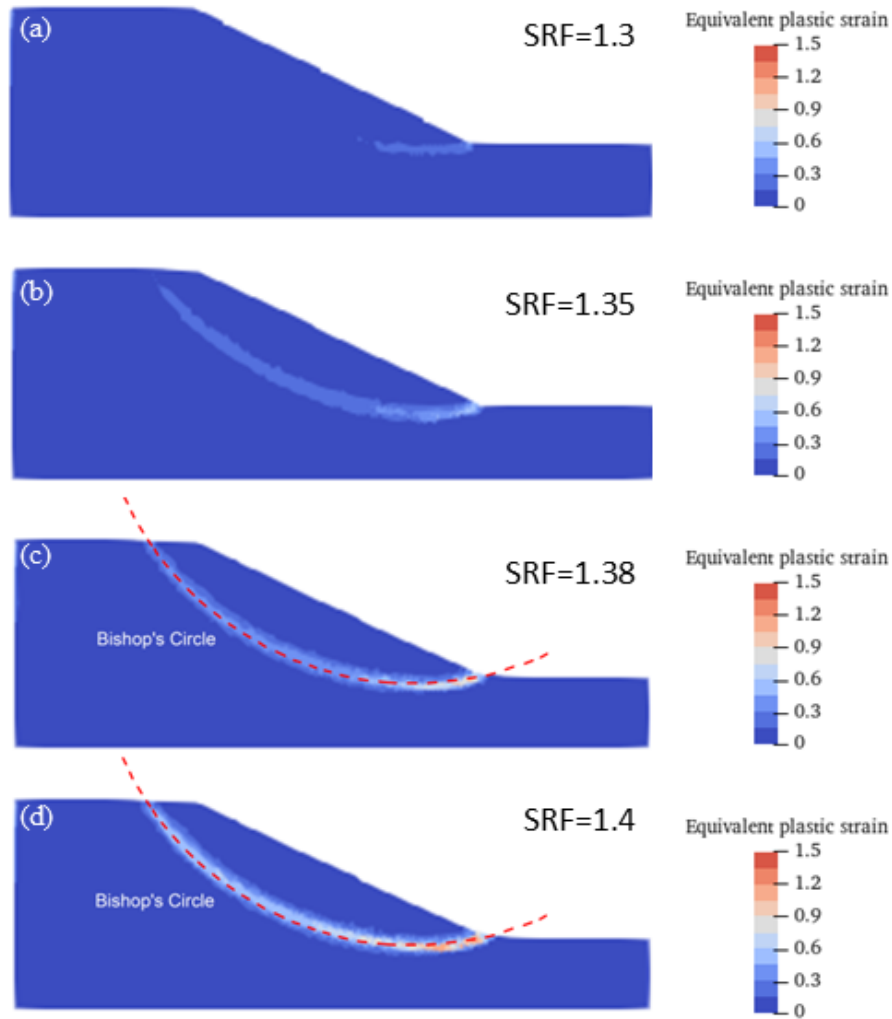
Fig. 3.3 Final equivalent plastic strain invariant contour of the cohesive soil slope for different SRFs (the dashed line denotes the Bishop's circle obtained by the limit equilibrium method)

Fig. 3.4 presents the results of slope stability analysis by shear strength reduction method. Fig.3. 4a shows the development of the kinetic energy of the slope with time. Although the kinetic energy curve in each case has two peaks, there are some discrepancies that cannot be ignored. For those cases with larger shear strength (SRF=1.25,1.3,1.35), the kinetic energy curve reaches a quite similar second peak, approximately 3kJ. However, once the SRF exceeds 1.35, the second peak increases rapidly, which indicates that the soil slope has failed. Fig. 3.4b describes the average total displacement variation of the slope with time. For the case of SRF=1.25 and SRF=1.3, the displacement curves start growing but they approach to a stable value in a short time. While this nearly horizontal displacement is not observed in the simulation of SRF=1.35. It is worth noting that the displacement growth rate is decreasing, which means that a convergent numerical solution can be

obtained in subsequent simulation. Furthermore, when SRF is greater than 1.35, the displacement curve grows with an increasing growth rate, causing the numerical solution to be non-convergent. As analyzed above, the sudden change in the curves of the total kinetic energy and the average displacement of the slope can be considered as an indicator of the slope entering a critical state because this abrupt variation is associated with the large deformation of the slope. Therefore, the detected FOS is 1.38, which is slightly lower than the prediction value of Fig. 3.3 but basically in line with the results of the FEM analysis (FOS=1.4) and the limit equilibrium analysis (FOS=1.37). Furthermore, combined with the equivalent plastic strain development in Fig. 3.3, the predicted FOS using the developed SPH model is 1.4. The above results demonstrate that the accurate FOS needs to be determined by multi-level stability analysis.
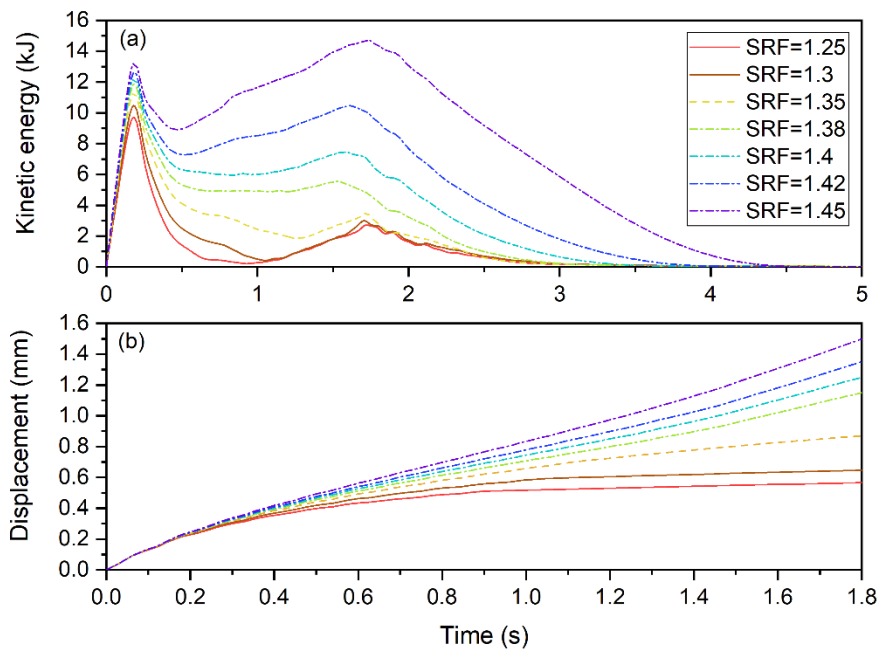
Fig. 3.4 Convergent/non-convergent analyses via SRF in SPH model

The above analyses demonstrate that the proposed SPH model can efficiently predict the potential failure surface as well as the FEM and LEM models. When it comes to large deformation problems, FEM is always limited because it suffers from severe mesh distortion near to the slip surface. On the contrary, our SPH model works properly and is able to reproduce the post-failure process of the slope. Fig. 3.5 shows the simulated total displacement of the slope with SRF=1.6. The slope reaches a new

equilibrium state shortly after the occurrence of slope failure. The maximum accumulated displacement appears at the slope toe is approximately 3.5 m.

Fig. 3.5 Accumulated displacement in the cohesive soil slope obtained by SPH model (SRF=1.6)

3.3.2 Retrogressive failure of a sensitive clay slope

In the second benchmark case, a numerical test on the failure process of a sensitive clay slope is conducted to verify the capability of our model in predicting the retrogressive failure of roto-translational lan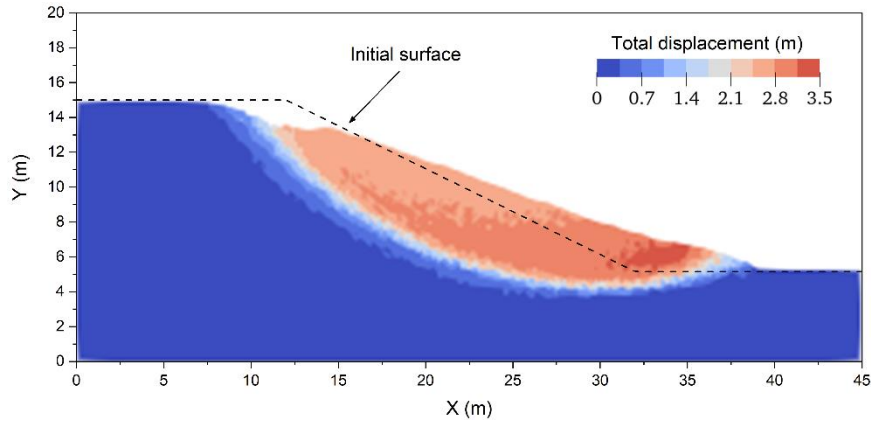dslides. In this simulation, a strain softening model is considered. Fig. 3.6 shows the initial geometry and the boundary condition of this case study. The slope is 5 m high with an inclination angle of 45°. The crest of the slope is 20 m long. The fully fixed boundary is imposed on the slope base, and the free-slip boundary is set on the left wall. The slope material is modeled by 11225 SPH particles with a smoothing length of 0.14 m. It is assumed that the slope is composed of uniform sensitive clay. The simulation parameters for this case are listed in Table 3.2. The undrained parameters are used in our simulation because the retrogressive landslides in sensitive clays are usually occurred in the undrained condition (Jin et al., 2020a; Locat et al., 2013). The simulation is run in two steps. The initial stress field is first generated under gravity. Subsequently, the slope collapse is initialized by applying a strength reduction factor of 1.65.
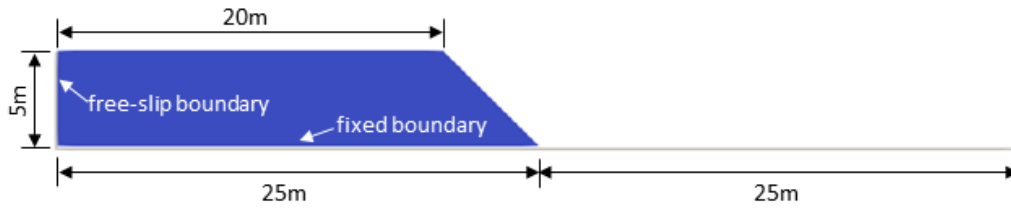
Fig. 3.6 Initial geometry and boundary conditions of the sensitive clay slope in SPH simulation

Table 3.2 Simulation parameters for modeling the sensitive clay slope failure

Parameters	Value
Material density (ρ)	2000 kg/m^3
Young's modulus (E)	10 MPa
Poisson's ratio (ν)	0.33
Internal frictional angle (ϕ)	0
Peak cohesion (c_p)	20 kPa
Residual cohesion (c_r))	4 kPa
Softening coefficient (η)	5
Dilatancy angle (ψ)	0

The simulated retrogressive failure process of the sensitive clay slope is illustrated in Fig. 3.7. At t = 0.6 s, the first slip surface (S1) occurs. This slip surface includes a horizontal band and a curved band. After 0.4s, the sliding body 1 (C1) disintegrated and a V-shaped shear band is generated. When t = 2.6 s, the second slip surface (S2) appears behind S1. Meanwhile, the graben-shaped clay block is formed because of the development of the V-shaped plastic shear band. The sliding body C1 is decomposed into 5 pieces at t = 3.4 s. Subsequently, the sliding body 2 (C2) is broken down into 3 pieces and the exposed back scarp emerges, resulting in the formation of the third slip surface (S3) (t = 5.6 s). It can be seen from t = 6.6s that the disturbed clay slope is reshaped into a series of grabens and horsts. Similar failure processes are repeated until a new stable slope configuration is formed (t = 15 s). At this stage, the exposed scarp is stable because the material in front of it provides enough support to resist further collapse. The final run-out distance is around 18.6 m, and the retrogression distance of the slope crest is 12.6 m.
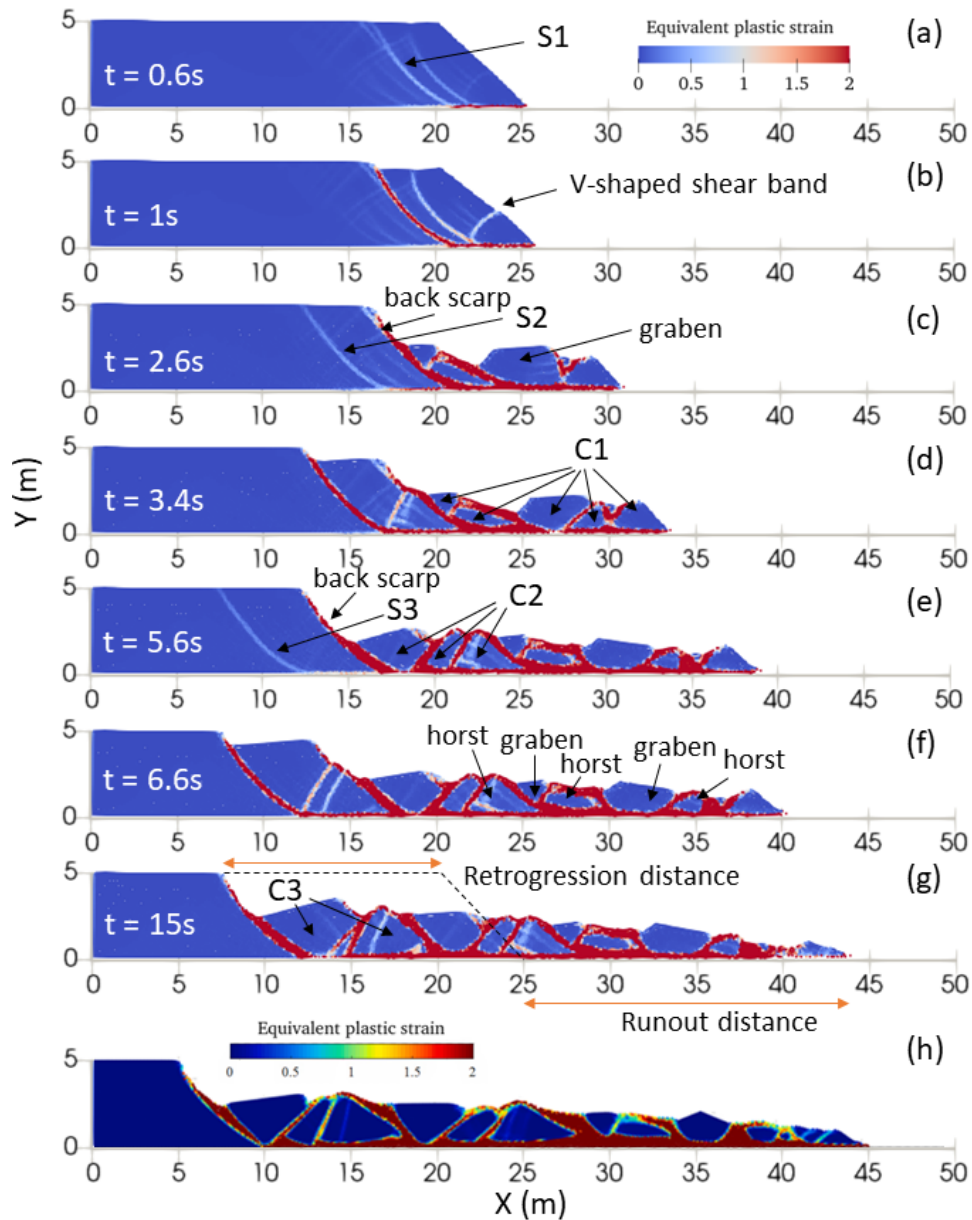
Fig. 3.7 Retrogressive failure of the sensitive clay slope in SPH simulation (Si and Ci represent the ith shear band and the ith clay block, respectively. Fig. 3.7h illustrates the final deposit configuration in the SPH model of Bui and Nguyen, 2021)

The simulation results of this case study by our model are compared with those from Bui and Nguyen (2021). It shows that the shape of the landslide deposit and final run-out distances obtained by us (Fig. 3.7g) and those obtained by Bui and Nguyen (2021) (Fig. 3.7h) are very close, indicating that our model can simulate the progressive failure behavior of the sensitive clay slope well. Furthermore, the retrogression distance of the slope crest corresponded to each failure and the final run-out distance of the two models are listed in Table 3.3. The results of these values in this study are slightly lower than those obtained by Bui and Nguyen (2021). A possible reason for this difference is that different kernel

functions and time-step integration methods are used in the two models.

Table 3.3 Comparison of retrogression and run-out distance of two SPH models

Parameters	SPH model (Bui and Nguyen, 2021)	SPH model in this study
1st retrogression distance (m)	5	4.6
2nd retrogression distance (m)	9.8	8
3rd retrogression distance (m)	15	12.6
Final run-out distance (m)	20	18.6

The maximum horizontal and vertical velocities of the slope at different times are shown in Fig. 3.8. The maximum vertical velocity of the slope significantly fluctuates three times, showing three local peak values (t=1.6 s, 3.7 s and 7.1 s), which is possibly associated with the three collapse processes of the sliding body (C1, C2 and C3). During each collapse process, the sliding body first accelerates along the sliding surface and then decelerates until it becomes stable again. The acceleration of the sliding body is attributed to the transformation of gravitational potential energy into kinetic energy. The deceleration process is related to plastic dissipation. However, only two waves are found in the maximum horizontal velocity curve. It is worth noting that the time of the second peak matches well with the third peak in the maximum vertical velocity curve. The discrepancy between the horizontal and vertical velocity curves may be related to the constraint of the motion direction in the vertical direction.
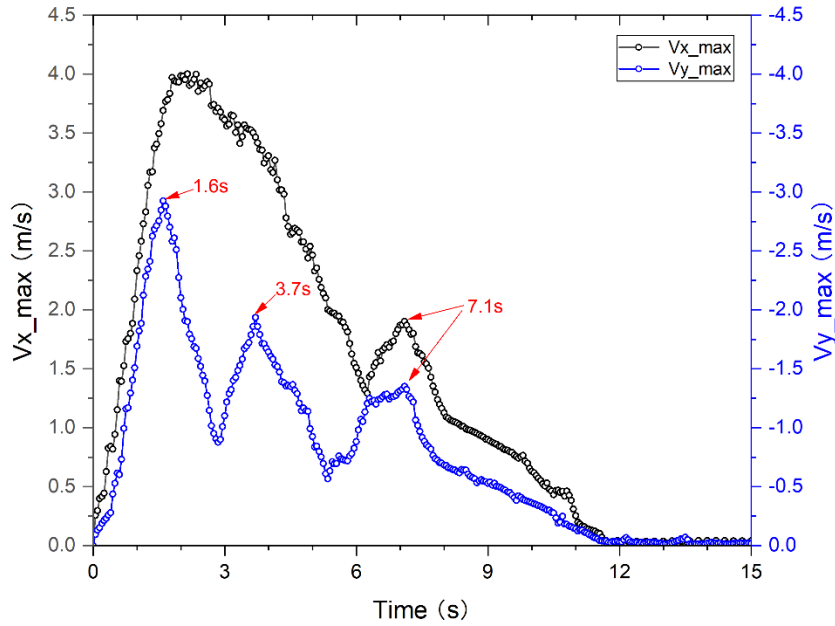
Fig. 3.8 Maximum horizontal and vertical velocities of the slope

To better understand the changes of the horizontal and vertical velocities of the slope throughout the failure process, three specific times are selected to present the velocity contour maps of the slope. The horizontal and vertical velocity maps are presented in Fig. 3.9. These times correspond to the times of the three peaks of the maximum vertical velocity curve in Fig. 3.8. As shown in Fig. 9b, the maximum vertical velocity is found among the sliding blocks marked by the red line. In particular, the vertical velocity (Vy) of the upper blocks is significantly larger than that of the lower triangular block at each moment. For each collapse, once the retrogressive failure is triggered, the upper blocks move downwards of a considerable distance due to the release of the gravitational potential energy, whereas the lower triangular block moves upwards slightly under the pushing effect of the upper blocks. On the other hand, the horizontal velocity (Vx) of the upper blocks is lower than that of the triangular block at the slope toe. A reasonable explanation is that the forward horizontal direction of the slope is unconstrained, which makes the block near the slope toe always move faster than that at the tail. Furthermore, the blue curves in Fig. 3.9 show the horizontal and vertical velocities along the cross-section of Y = 1 m. As seen in Fig. 3.9b, the maximum vertical velocity always corresponds to the blocks that belong to current collapse. But in Fig. 3.10a, the same pattern is only observed in the horizontal velocity curve at t = 7.1 s. As for curves at t = 1.6 s and t = 3.7 s, the maximum value

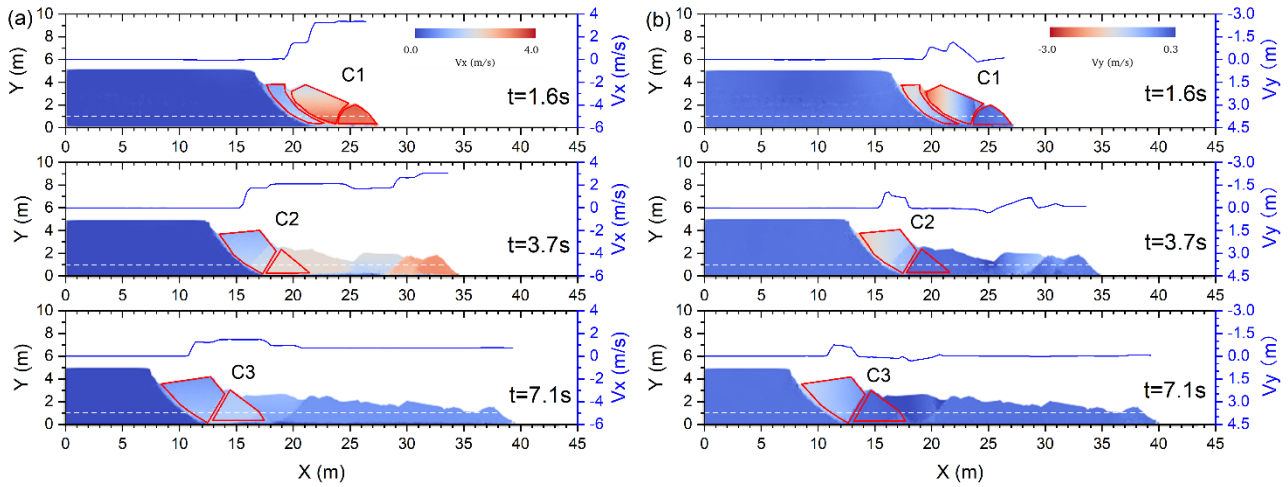emerges in the front of the slope. These results are consistent with those results reflected in Fig. 3.8.

Fig. 3.9 Contours of (a) the horizontal velocity, Vx, and (b) the vertical velocity, Vy, at different times. The blue curves correspond to values of Vx and Vy along the cross-section Y = 1 m

The residual cohesion is a significant parameter in determining the retrogressive failure pattern of the slope. Six simulations with different residual cohesion are carried out to investigate the influence of the residual cohesion on the slope failure process. The simulated retrogression distance and run-out distance in each case are shown in Fig. 3.10. The simulated retrogression distance curves are in step-like shape (Fig. 3.10a). The occurrence time of each surge in retrogression distance represents that formation time of a new back scarp. When the slope is under a relatively high strength condition (Cr = 8 kPa), only one collapse is triggered, and soon the slope becomes stabilized again. For those cases with medium shear strength (Cr=5, 6 and 7 kPa), the curves show a similar two-step feature. In addition, the first step is almost overlapping, whereas the second step can be easily distinguished. The greater the residual cohesion, the later the second back scarp is formed. When the slope strength is further decreased to 4 kPa, the third step appears, which means that the slope reaches a stable state after three retrogressive failures. As shown in Fig. 3.10b, all run-out distance curves present a similar pattern with time: the run-out distance increases gradually until reaches a stable value. The final run-out distance shows a negative correlation with the residual cohesion.
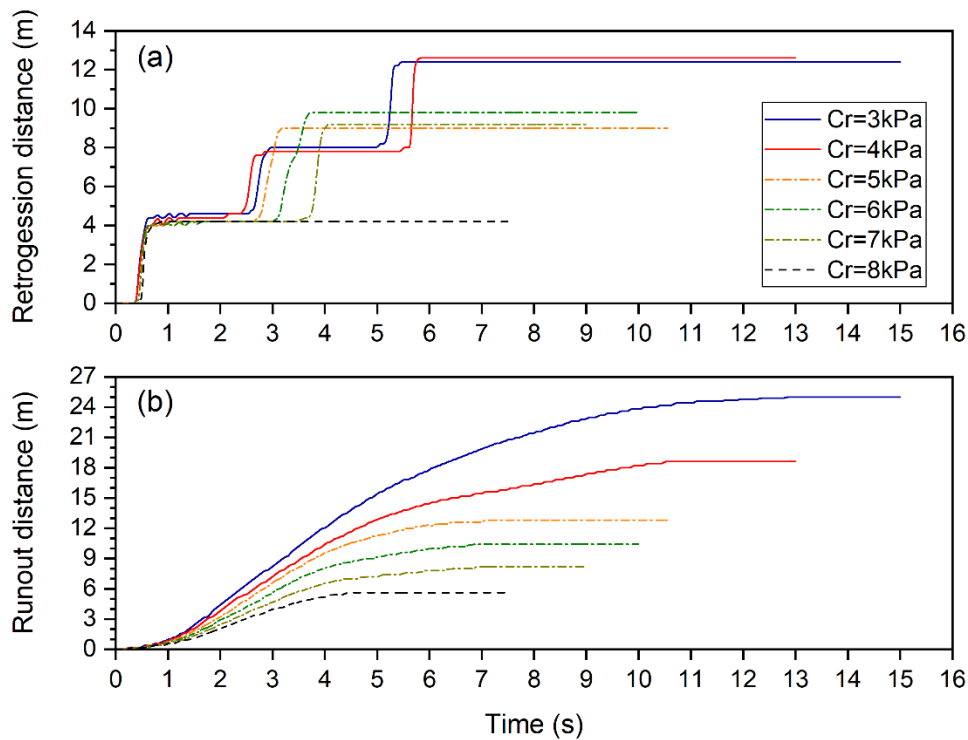
Fig. 3.10 (a) Retrogression distance curve and (b) run-out distance curve of the sensitive clay slope simulations with different residual cohesion

3.4 Simulation of the Caijiapo landslide

3.4.1 Overview of the Caijiapo landslide

The Caijiapo landslide is a typical roto-transitional landslide that occurred on the north side slope of the Baoji Loess Plateau, Qishan County, Shaanxi Province, China (Fig. 3.11a). The left and right boundaries of the Caijiapo landslide are connected to the boundaries of the other two landslides, while the back scarp and front of the landslide can be clearly distinguished from the surrounding environments (Fig. 3.11b). The back scarp is about 30 m high and 50 m wide, with an average slope of 38 ° (Fig. 3.11c). The landslide tongue comprises a series of steep ridges with visible shear bands (Fig. 3.11d). The landslide shows triangular shape in the plane view (Fig. 3.11e). The main sliding direction is SSW195° and the average slope of the landslide zone is around 22°. The landslide mass is about 470 m long in the main sliding direction, and the landslide tongue is 500 m wide. Due to the multi-stage sliding, a series of tensile cracks formed in the middle and the front parts of the landslide. The height of these cracks is 7~15 m, and the extension length of the cracks is 20~30 m.

The geological map of A-A' profile (in Fig. 3.11e) is shown in Fig. 3.11f. The main strata in the landslide area are Quaternary loess and Neogene mudstone. The landslide mass is mainly composed of silty clay and the thickness ranges from 20 m to 60 m. The landslide is a typical roto-translational landslide with a slip surface in "L" shape. The rear part of the slip surface is arc-shaped, with an averaged dip angle of 60°, while the middle and the front parts are nearly horizontal, with a dip angle of approximately 6°. The rotational slip surface develops in the loess layer and the translational slip surface beds on the Neogene mudstone belonging to the Sanmen Formation.

Since the 1960s, after the construction of the drain canal, the loess slope where the Caijiapo landslide was located on became unstable. Although the slope has experienced multiple slips, the potential energy has not been completely released and is still in the creep deformation stage.
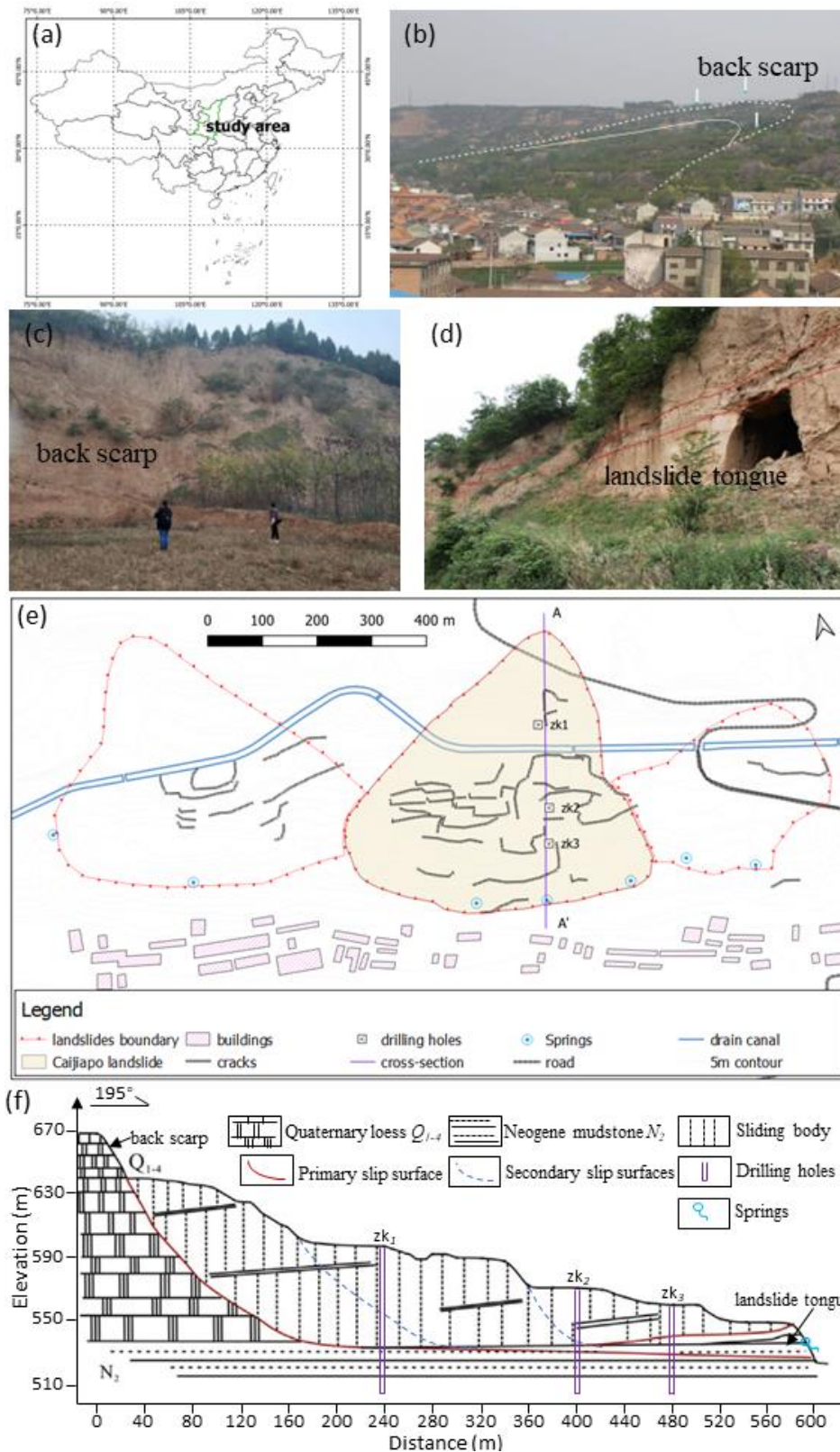
Fig. 3.11 (a) Location of the study area, (b) panorama of the Caijiapo landslide, (c) back scarp and (d) front of the landslide, (e) plane view of the landslide zone and (f) geological cross-section of A-A'

3.4.2 Numerical modeling

In order to investigate the failure mechanism of the Caijiapo landslide, a simplified SPH model (Fig. 3.12) of this landslide is established according to the geological profile in Fig. 3.11f. According to previous studies (Shi et al., 2016), landslides in the study area are multiple loess landslides controlled by clay strata and faults. The fault activity on the northern edge of the Wei River in the Loess Plateau produced a weak structural plane which formed the back scarp of the landslide. Therefore, the initial slope in the simulation is composed of loess with a structural plane (the dashed line in Fig. 3.12). The pre-failure topography is estimated based on the surrounding slopes without landslides. The left and bottom boundaries of the model are free-slip and fixed boundaries, respectively. The simulation parameters adopted in this simulation are determined by laboratory tests, and are listed in Table 3.4. Note that the loess on both sides of the structural plane has different strength parameters. The strength of the loess on the right side of the structural plane is relatively weak due to the influence of the tectonic movement and to the effect of groundwater.
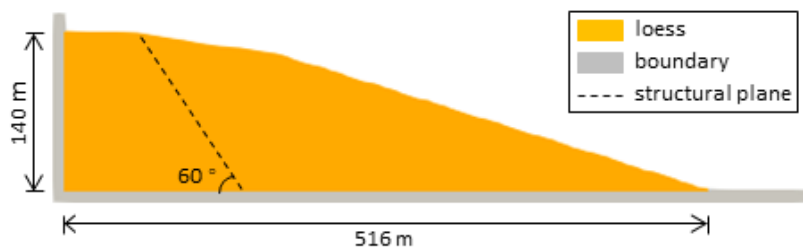
Fig. 3.12 Pre-failure slope of the Caijiapo landslide for SPH modeling

Table 3.4 Parameters for simulating the Caijiapo landslide adopted in the SPH model

Materials	Loess on the left	Loess on the right
Density (kg/m³)	2050	2050
Young's modulus (MPa)	15	1
Poisson's ratio	0.35	0.33
Peak frictional angle (°)	28	24
Residual frictional angle (°)	23	7.2
Peak cohesion (kPa)	30	20
Residual cohesion (kPa)	21	4.8
Softening coefficient	1.5	6

The simulated final displacement in the Caijiapo landslide is shown in Fig. 3.13. The simulated topography of the landslide deposit agrees generally well with that measured in the field. The run-out distance of the landslide is slightly underestimated in our simulation. As illustrated by the displacement contour in the landslide, 3 slip surfaces are formed in the landslide. The primary slip surface follows the structural plane caused by tectonic movement. The simulated locations and shapes of the primary slip surface (1st slip surface at the back scarp) and the 2nd slip surface are in good line with the field observations, while the simulated location of the 3rd slip surface is approximately 30 m closer to the back scarp than that obtained by the field investigation.
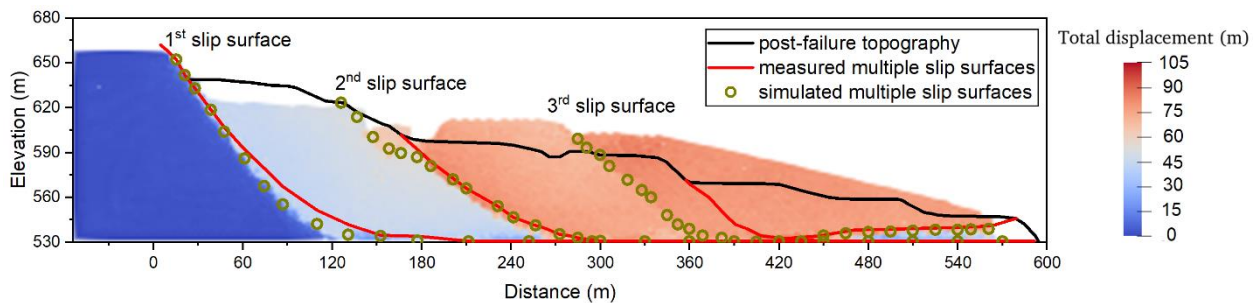
Fig. 3.13 Simulated displacement in the final deposit of the Caijiapo landslide

The simulated failure process of the Caijiapo landslide is shown in Fig. 3.14. At t = 19 s, the 1st slip surface develops in the silty clay layer and the shear outlet is visible at the landslide front. This is consistent with that observed in the field (Fig. 3.11f). After the formation of the 1st slip surface, the sliding body moves forward as a whole block (Fig. 3.14a). Then, the sliding body divides into two parts due to the development of the 2nd slip surface. Meanwhile, the block behind the 2nd slip surface also breaks because the shear failure occurs in the block, forming two smaller blocks in the shape of a graben and a horst (Fig. 3.14b). The 3rd slip surface is shown in Fig. 3.14c. The block separated by the 2nd and the 3rd slip surfaces remains intact until the end of the run-out process. The formation processes of the three scarps in the landslide mass and the landslide tongue are well simulated (Fig. 3.14d). In addition, the soil in the shear bands (materials in red) is fully yielded, whereas the soil blocks outside the failure band (materials in blue) are slightly disturbed.
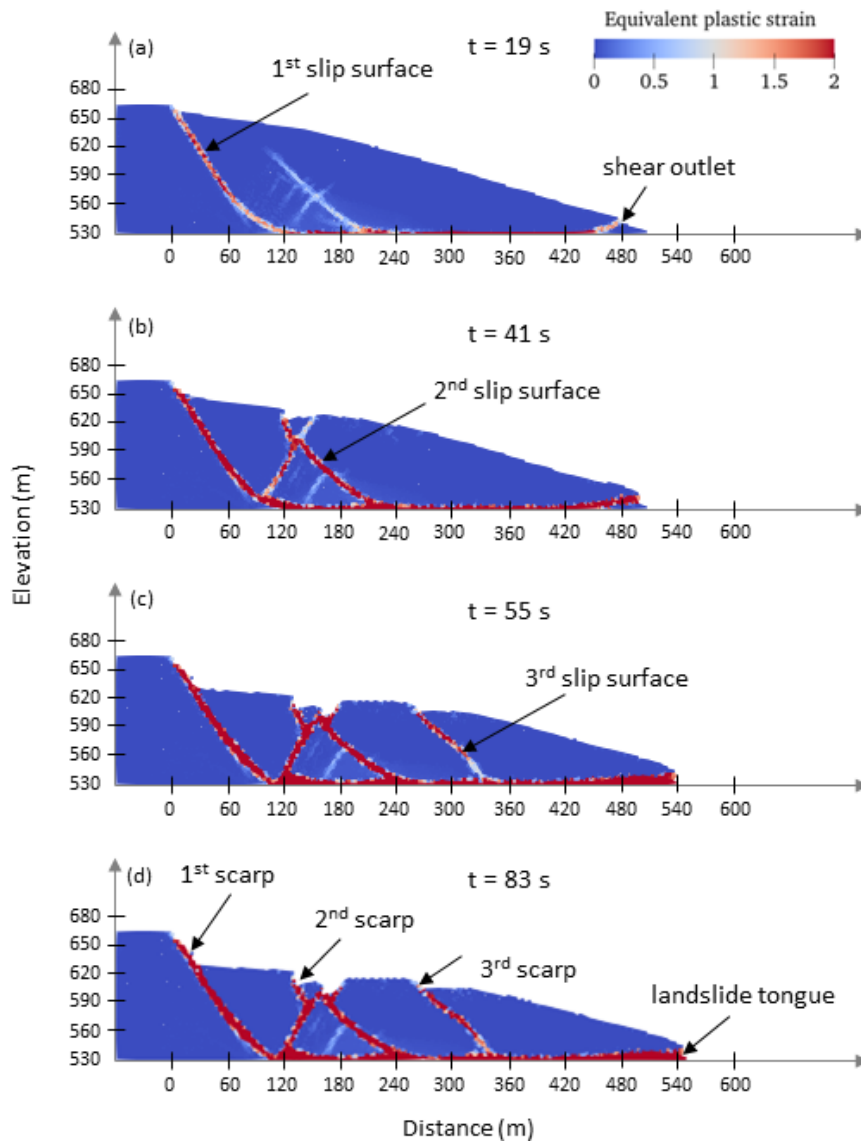
Fig. 3.14 Multiple sliding processes of the Caijiapo landslide simulated by the SPH model at (a) t = 19 s, (b) t = 41 s, (c) t = 55 s, and (d) t = 83 s

The velocities in the sliding mass at several times coresponding to the occurrence of each slip surface the Caijiapo landslide are also intereasting. During each faliure process of the landslide, the velocity vectors are generally parallel to the slip surface (Fig. 3.15 (a-c)). The three slip surfaces of the landslide are in the "L" shape and consist of a rotational slip zone and a translational slip zone, which are common in roto-translational landslides (Xin et al., 2018; Yenes et al., 2009). In the rotational slip zone, the gravitational potential energy of the landslide is transformed into kinematic energy, resulting in relatively high velocitiy. The moving direction of the landslide in the translational slip zone is almost horizontal. Furthermore, the masses involved in a previous failure are almost static

or have a relatively low velocity when a new slip surface emerges, while the sliding mass involved in the recent slip surface moves forward at a higher velocity. For the Caijiapo landslide, the maximum velocity occurs in the 2nd slip (Fig. 3.15b).
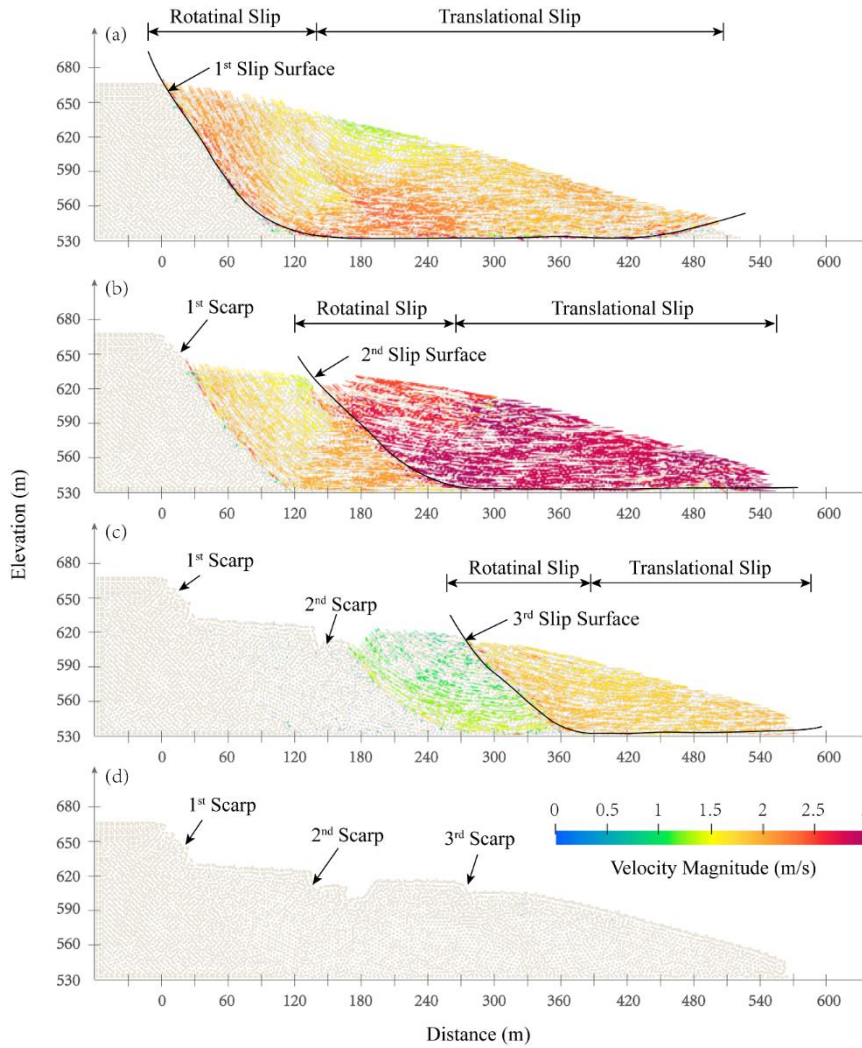
Fig. 3.15 Velocity vectors of the Caijiapo landslide, at (a) t = 19 s, (b) t = 41 s, (c) t = 55 s, and (d) t = 83 s. The black solid lines indicate the multiple slip surfaces

3.5 Conclusions

In this study, the strain softening elastic-plastic constitutive law is incorporated into the original SPH code to extend its application in modeling the roto-translational landslides. Two benchmark cases are used to validate the capability of the proposed SPH model in capturing the dynamic failure

process and post-failure behavior of the slope. Finally, the failure and run-out process of the Caijiapo landslide are analyzed by the proposed mode. The main conclusions are drawn as follows:

(1) The failure process of the cohesive soil slope without strain-softening can be precisely analyzed by the proposed SPH model considering the elastic-plastic constitutive law. The simulated failure surface agrees well with that obtained by the Bishop's method. The predicted FOS is approximately 1.4, which is in line with that predicted by the LEM and FEM.

(2) The retrogressive failure process of the sensitive clay slope with strain softening effect is well reproduced by the modified SPH model with strain softening. The failure mode can be generally summarized as follows: the first retrogressive failure occurs in the front part of the slope; subsequently, the second retrogressive failure occurs due to the unloading of resistance at the slope toe; and then the third retrogressive failure forms until the final stable back scarp is formed. At each failure, the intact clay block can be further decomposed into several small pieces in the form of horsts and grabens. Additionally, the simulation results of this case study indicate that our model can efficiently predict the failure and run-out processes of a strain softening roto-translational landslide.

(3) The simulation results of the Caijiapo landslide indicate that two secondary slip surfaces are triggered after the occurrence of the primary slip surface. The primary slip surface develops along a pre-existing structural plane at the back scarp the landslide, which controls the failure pattern of this landslide. The two secondary slip surfaces are formed due to the deformation in the sliding mass. These slip surfaces divide the landslide into four blocks. The formation process of the three scarps and the landslide tongue are satisfactory simulated by our model.

4. Interaction between debris flow and structures

Landslide-structure interaction (FEI) plays a significant role in the field of geotechnical engineering, civil engineering, and natural hazard risk assessment. Understanding how landslides interact with structures is crucial for developing resilient infrastructure, ensuring public safety, and mitigating the impacts of landslides on communities and the environment. The knowledge gained from such studies contributes to more effective risk management and sustainable development practices in landslide-prone areas. Therefore, this section is dedicated to study the dynamic impact process of debris flow and its interaction with protective structures.

4.1 Introduction

Debris flows are regarded as the most dangerous mass movements in mountainous areas due to their high mobility and long run-out distance. They usually destroy the nearby infrastructure and pose a significant threat to the safety of the local inhabitants. Various types of prevention structures such as check dams (Shen et al., 2020, 2019; Yu et al., 2020), rigid walls (Armanini et al., 2019; Calvetti et al., 2017; Faug, 2015), flexible barriers (Liu and Liang, 2022; Ng et al., 2017c; Tan et al., 2019), filter dams (Huang et al., 2007) and sectional dams (Bernard et al., 2019) have been installed along the debris flow gullies to mitigate the potential risk from debris flows. A key parameter for designing these structures is the peak impact force of debris flow acting on the structures (Lei et al., 2018; Li et al., 2020; Scheidl et al., 2013). However, this parameter is difficult to obtain because of the complexity of the impact process of debris flow (Ma and Zhang, 2007).

Limited field data related to the impact force of debris flow are available, owning to the difficulties in monitoring real debris flows and their interaction with defense structures (Hong et al., 2015; Suwa et al., 1973; Wendeler et al., 2007). Therefore, physical model tests of debris flow became a popular method to study the impact process of debris flow against structures. Many researchers adopted small-scale flume tests to simulate this process (Choi et al., 2018; Cui et al., 2015; Faug et al., 2008b;

Huang et al., 2022a; Jiang and Towhata, 2013; Moriguchi et al., 2009; Zhang and Huang, 2022; Zhou et al., 2018). Although these small-scale tests are simple and convenient for engineering purposes, they inevitably suffer from the size-effect. To reduce the influence of size-effect, centrifuge flume tests have been carried out to investigate the impact of different geophysical flows on the mitigation measures (Ng et al., 2017c; Zhang and Huang, 2022) (Ng et al., 2019, 2017b; Song et al., 2018, 2017; Zhang and Huang, 2022; Zhang et al., 2022) but the test conditions of the centrifuge tests are still too simple and are very different with the real debris flows. By contrast, numerical modeling is an efficient alternative, due to its low cost and high capacity in simulating complex conditions. Currently, full 3D models such as the Discrete Element Method (DEM) (Calvetti et al., 2017; Ng et al., 2017b; Shen et al., 2018; Zhang and Huang, 2022), Smoothed Particle Hydrodynamics (SPH) method (Dai et al., 2017; He et al., 2018; Huang et al., 2022b; Sheikh et al., 2021) and Material Point Method (MPM) (Cuomo et al., 2021; Li et al., 2020, 2018; Mast et al., 2014) have been applied in studying the interaction between flow-type mass movements and structures. Among these models, DEM is more suitable for simulating dry granular flows, and MPM is mainly devised for solving continuous solid mechanics problems (Jiang et al., 2016; Zhang and Huang, 2022). In comparison, the SPH models have been widely applied in analyzing the dynamic process of plastic or viscoplastic flows and have shown good potential in modeling flow-structure interaction problem (Dai et al., 2017; Han et al., 2019).

One key issue limiting the capacity of the SPH method in simulating debris flow is the rheology law adopted in current the SPH models. The Bingham law is firstly incorporated into the SPH model to simulate debris flows (Dai et al., 2017; Ulrich et al., 2013). However, a numerical divergence problem will arise when the shear strain rate $\dot{\gamma}$ in the Bingham law approaches to 0. Additionally, this model cannot simulate the shear thinning and shear thickening behavior of debris flows because it assumes a linear relationship between shear stress and shear strain rate. Therefore, the HBP constitutive law is commonly adopted to avoid the abovementioned problems. Although the SPH models adopting the HBP law show better performance in simulating the propagation and impact process of debris flows than the SPH models using the Bingham law, the simulated deposit of debris

flow is generally much thinner than the real case because the frictional dissipation of debris flow is not considered in the original HBP law. To overcome this limitation, in this study we proposed a novel SPH model by incorporating a modified HBP law which accounts for the friction dissipation of debris flow to improve the capability of the SPH models in simulating the debris flow-structure interaction problems.

4.2 Methodology

4.2.1 Governing Equations

Debris flows are treated as weakly compressible fluids in this study. Therefore, the momentum equation (Eq. (2.9)) above can be expressed in the following discrete form

$$\frac{dv_i}{dt} = -\sum_{j=1}^{N} m_j \left(\frac{P_i}{\rho_i^2} + \frac{P_j}{\rho_j^2}\right) \nabla_i W_{ij} + g + m_j \left(\frac{\tau_i}{\rho_i^2} + \frac{\tau_j}{\rho_j^2}\right) \nabla_i W_{ij} \qquad (4.1)$$

In Eq. (4.1), the first term on the right side represents the balanced form of the pressure term, the second term indicates the acceleration due to gravity, and the last term denotes the discrete scheme of the shear stress, which will be introduced in detail in Section 4.2.2.

4.2.2 Constitutive model

4.2.2.1 Debris flow rheological laws

According to previous studies, the non-Newtonian rheological laws (such as Bingham law, HB law and HBP law) are more suitable for modeling debris flows than the Newtonian rheological laws (Rickenmann et al., 2006; Shieh et al., 1996). Many previous studies related to SPH simulation mainly adopted the Bingham law to simulate the rheology of debris flow (Dai et al., 2017; Komatina and Jovanovíc, 1997; Monaghan, 1994; Ulrich et al., 2013; Uzuoka et al., 1998). The Bingham law assumes that the flow-like movement begins only if the shear stress is larger than a critical value

(i.e., the yield strength τ_y), otherwise the material behaves like a solid. The expression of the shear stress $\boldsymbol{\tau}$ is:

$$\boldsymbol{\tau} = \left(\mu + \frac{\tau_y}{2|\dot{\boldsymbol{\gamma}}|}\right)\dot{\boldsymbol{\gamma}} = \mu_{eff}\dot{\boldsymbol{\gamma}} \tag{4.2}$$

where $\dot{\boldsymbol{\gamma}}$ is the shear strain rate tensor, $|\dot{\boldsymbol{\gamma}}|$ is the magnitude of the shear strain rate tensor, μ is the dynamic viscosity of the material with the unit $\mathrm{Pa} \cdot \mathrm{s}$, τ_y is the yield strength of the material, and μ_{eff} is the effective coefficient (Uzuoka et al., 1998).

According to Eq. (4.2), the effective viscosity will approach infinity when the shear rate tends to 0, which may lead to numerical divergence problem. Additionally, the linear relationship assumption between the shear stress and shear rate is inappropriate for debris flow. In fact, due to the complexity of their compositions, debris flows always exhibit either dilatancy or pseudo-plasticity (Major and Pierson, 1992; Parsons et al., 2001; Pudasaini, 2011). Therefore, Herschel-Bulkley (HB) model was proposed (Pasculli et al., 2013). In the HB model, the effective viscosity is given by:

$$\mu_{eff} = \mu|\dot{\boldsymbol{\gamma}}|^{n-1} + \frac{\tau_y}{2|\dot{\boldsymbol{\gamma}}|} \tag{4.3}$$

One extra parameter n is embedded into the equation in comparison with the Bingham model. Particularly, the HB model reduces to the Bingham model when $n = 1$. Although this rheological law can more accurately predict the deformation behavior of debris flow, it still cannot avoid the numerical divergence problem. For this reason, (Papanastasiou, 1987) introduced another constant coefficient m into Eq. (4.3).

$$\mu_{eff} = \mu|\dot{\boldsymbol{\gamma}}|^{n-1} + \frac{\tau_y}{2|\dot{\boldsymbol{\gamma}}|}\left[1 - e^{-m|\dot{\boldsymbol{\gamma}}|}\right] \tag{4.4}$$

The Herschel-Bulkley-Papanastasiou (HBP) law (Eq. (4.4)) is always convergent because it is continuous and does not exhibit a discontinuity at $\tau = \tau_y$. For $n = 1$ and $m = 0$, the HBP model reduces to describe the Newtonian fluid. As $m \to \infty$, the HBP model can approximately represent the HB model, and is further transformed into the Bingham model when $n = 1$. Overall, the HBP law is a general rheological law which can represents a variety of fluids by adopting different m and

n values. The flow can behave as a shear-thinning fluid ($n < 1$) or a shear-thickening fluid ($n > 1$).

4.2.2.2 A modified HBP model considering the material friction

The yield shear strength τ_y is a constant in HBP law. However, for geo-materials, τ_y should be pressure-dependent. Therefore, in this study, we use the Mohr-Coulomb criterion to calculate the τ_y in HBP model, so that the modified HBP model could simulate the frictional dissipation of debris flow. The failure envelope can be written in terms of pressure P and the second invariant of deviatoric stress J_2:

$$\sqrt{J_2} = P \sin \varphi + c \cos \varphi \tag{4.5}$$

where φ and c denote the internal friction angle and the cohesion of the material. The geo-material starts to yield when a critical value of shear stress τ_y is reached.

$$\sqrt{J_2} = \tau_y \tag{4.6}$$

Combining Eq. (4.5) with Eq. (4.6), the yielding stress τ_y of a geo-material which yields under the Mohr-Coulomb criterion can be expressed as

$$\tau_y = P \sin \varphi + c \cos \varphi \tag{4.7}$$

Substituting the above equation into Eq. (4.4), the effective viscosity can be expressed as

$$\mu_{eff} = \mu |\dot{\gamma}|^{n-1} + \frac{P \sin \varphi + c \cos \varphi}{2|\dot{\gamma}|} \left[1 - e^{-m|\dot{\gamma}|} \right] \tag{4.8}$$

Negative pressures will appear when using the EoS (Eq. (2.10)) to determine the pressure based on particle density. In this study, the positive pressures $P_+ = max\{0, P\}$ are used. Thus, the modified HBP law is given by:

$$\tau = \left\{ \mu |\dot{\gamma}|^{n-1} + \frac{P_+ \sin \varphi + c \cos \varphi}{2|\dot{\gamma}|} \left[1 - e^{-m|\dot{\gamma}|} \right] \right\} \dot{\gamma} \tag{4.9}$$

This novel rheological law can mimic a variety of fluids by changing the parameters (c, φ, m, n).

When c, φ and m equal to 0 and $n = 1$, the law describes the Newtonian fluid, while it describes the Bingham-type fluid (purely cohesive material) when $\varphi = 0$ and $c \neq 0$.

4.3 Validation of the model

Two benchmark tests are used to validate the proposed model. The first one is the column collapse test conducted by Bui et al., (2008) which has been widely used to test the accuracy of numerical models in predicting the movement of frictional material (Peng et al., 2021; Solowski and Sloan, 2015; Zhang et al., 2021). The second one is the sand flume experiment conducted by Moriguchi et al. (2009), which is usually used to validate the numerical models for simulating the dynamic impact of debris flow against structures (Cuomo et al., 2021; Dai et al., 2017; Peng et al., 2021).

4.3.1 Simulation of the column collapse test

In the experiment of (Bui et al., 2008), small aluminum bars with a length of 50 mm and a diameter of 1 mm or 1.5 mm were used to form a rectangular region (200 mm×100 mm×50 mm) that simulates a soil column. The column collapse was triggered by quickly removing the supporting wall on the right side of the column.

This experiment was simulated by our modified SPH model and the original HBP-based SPH model. In both simulations, the soil column was modeled by 64000 fluid particles with an initial particle spacing of 2.5 mm. Based on the results of four shear box tests on aluminum bars (Bui et al., 2008), the following material parameters were used in our modified SPH model: density $\rho = 2650\ \mathrm{kg/cm^3}$, internal friction angle $\varphi = 19.8°$ and cohesion $c = 0$ kPa. Substituting the average pressure obtained in the modified SPH model and the shear strength parameters (φ, c) above into Eq. (4.7), the yield shear stress τ_y is estimated to be 0.36 kPa in the original HBP-based SPH model.

The simulation results are shown in Fig. 4.1 and compared with the experiment results in Fig. 4.2. It

shows that the numerical results obtained by our modified SPH model match well with the experimental results not only in terms of the height profile of the deposit but also the yield lines inside the column (Fig. 4.2). In comparison, due to lack of friction in the original HBP-based SPH model, the material moves faster after collapse, resulting in a greater horizontal travel distance and a flatter deposition profile. Overall, our model shows a good capability in simulating frictional flow.
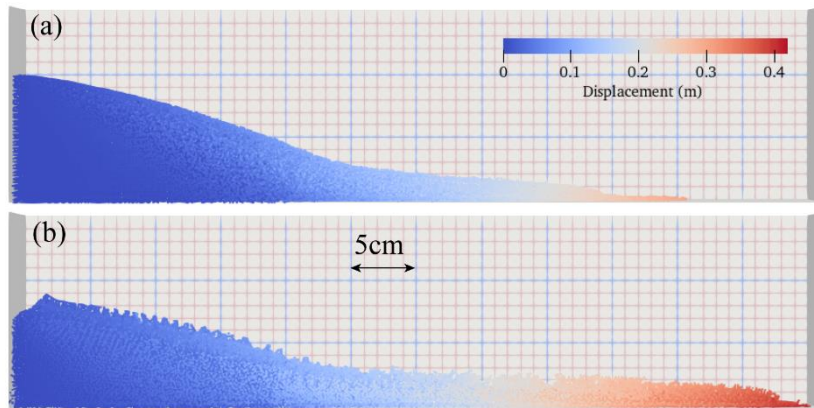
Fig. 4.1 The simulation results of column collapse test of a. the modified SPH model and b. the original HBP-based SPH model
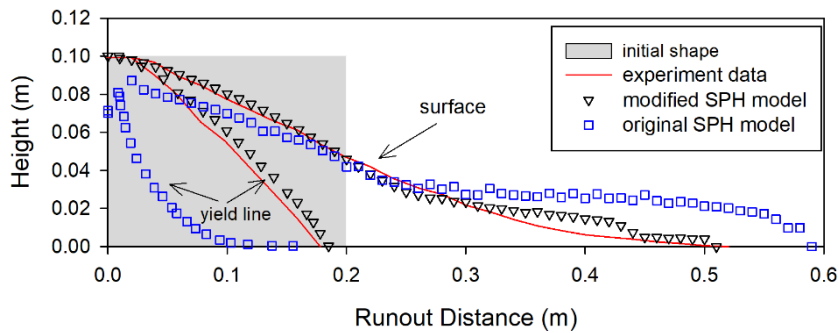
Fig. 4.2 Final surface height profile and yield lines in experiment and simulation

4.3.2 Simulation of the sand flume test

In the sand flume tests conducted by (Moriguchi et al., 2009), sand columns (50 kg sand in each test) were released from a box to the flumes with different slope angles, and the run-out process of the sand flows and their impact process with the load cell were recorded (Fig. 4.3). This experiment was simulated by our modified SPH model. The initial inter-particle distance was 0.005 m, and

consequently 290,675 fluid particles and 270,529 boundary particles participated in the simulation.
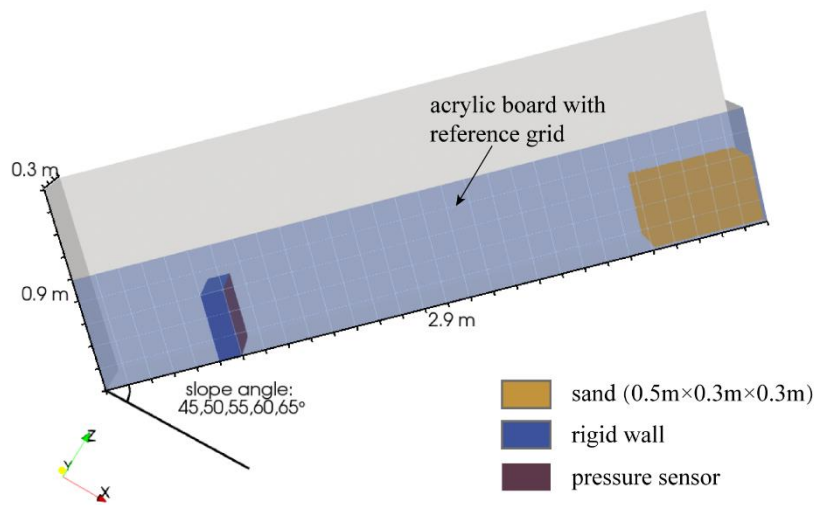
Fig. 4.3 Schematics of the sand flume experiment of Moriguchi et al. (2009)

The flume test with a slope angle of 45° was used to calibrate the rheological parameters using the free surfaces of the sand in this test at four different times (0.4, 0.8, 1.2 and 1.6 s) were provided in (Moriguchi et al., 2009). The simulation results using the parameters listed in Table 4.1 fit well with the experimental data (Fig. 4.4). Adopting these rheological parameters, we conducted the simulations with flume angle of 50°, 55°, 60° and 65° to investigate the impact process of sand flow against the structure. The simulated impact forces and the experimental results are shown in Fig. 4.5. The simulation results are consistent with the impact force curves obtained from the experiments, demonstrating the good applicability of our model in studying the granular flow-structure interaction problems.
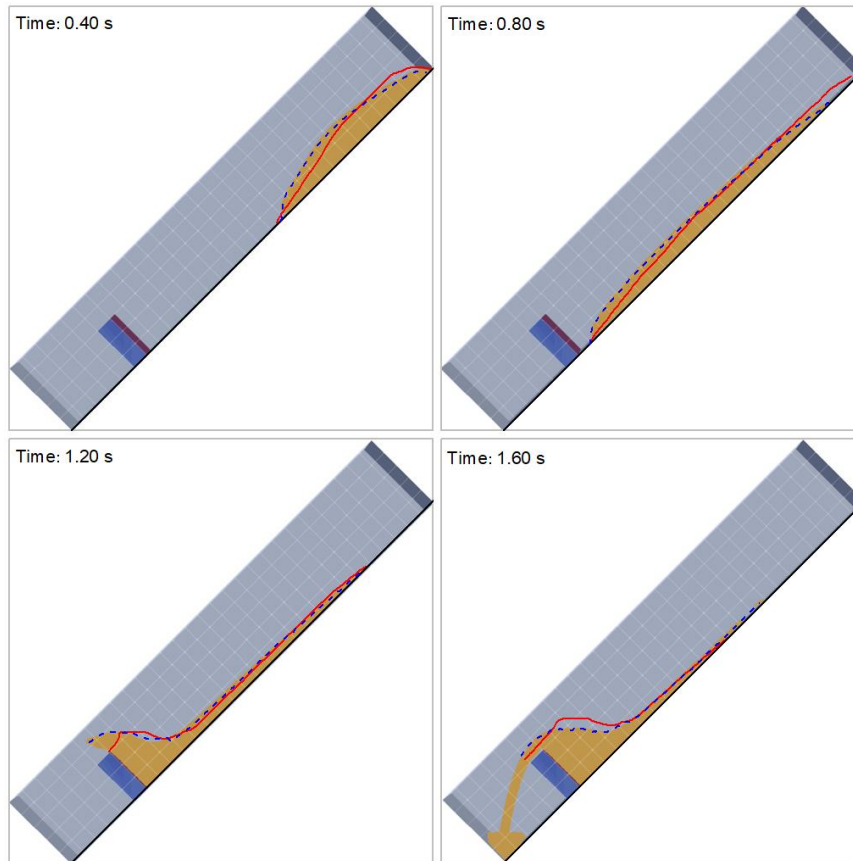
Fig. 4.4 Simulation results of the sand flume tests inclined at 45° of the modified SPH model (red lines represent the experiment results)

Table 4.1 Calibrated HBP model parameters for the test with an inclination of 45°

Parameters	Notion	Unit	Value
Coefficients in HBP law	m	/	100
	n	/	1.05
Fluid density	ρ	kg/m^3	1379
Dynamic viscosity	μ	Pa·s	0.02
Internal friction angle	φ	°	35
Cohesion	c	kPa	0
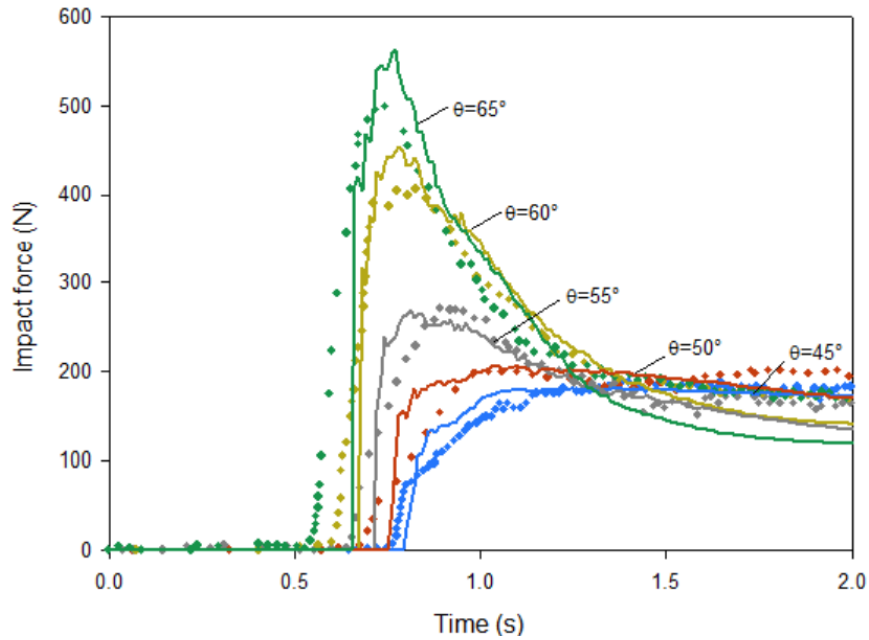
Fig. 4.5 Simulated and the experimental results of the impact forces in different flume dip angle conditions (solid lines represent simulation results and dots represent experimental results)

Fig. 4.6 shows the flow velocity field of sand flow against different times. Four critical times were selected to investigate the flow pattern evolution and impact mechanism in two flumes (inclination 45° and 65°). t1 was define as the time when the particles at the front of the sand flow first touched the rigid wall, and the flow-obstacle interaction was triggered at the same time. After t1, the impact force loaded in the rigid wall started to increase gradually, and when it reached the maximum value, the corresponding time is captured as t2. Afterwards, the impact force began to decrease as a large amount of the incoming flow transported over the obstacle. We estimated the time when the sand flow travels approximately 0.25 m over the obstacle and denoted it as t3. Finally, the time t4 is defined as the final time of numerical simulation, t4=2.0 s.

Two inclination flumes exhibit a very similar flow pattern at the time of t1, which is a parabolic cross-section. However, at the same location of the flume, a steeper inclination will result in a larger flow velocity. Since t1 s, the flow material of both cases was blocked by the wall and gradually reached the top of the wall, which acted as a springboard for the approaching particle. During this period (t1~t2), the impact force applied to the wall rapidly increased. At t2 s, the incoming flow passed smoothly on the surface of the deposited material to detach from the top of the wall. In a low

slope situation, the incoming flow gently ran over the wall and formed a stationary jet while a stronger vertical jet was formed for a high slope. Two different granular patterns resulting from the flow-obstacle interaction are clearly observed at the time of t3. For the 45-slope flume, a large amount of sand was prevented behind the wall, namely the granular bore, while another portion overtopped (transported over) the wall and deposited downstream of the wall. For the 65-slope flume, a large airborne jet was formed downstream of the wall. At t4 s, the flow upstream of the wall basically tended to be the stagnant state. Two completely distinct deposition patterns formed behind the wall. As mentioned above, a granular bore was formed in the 45° flume test while a small wedge with a size of approximately close to wall height was generated for the 65° flume experiment.
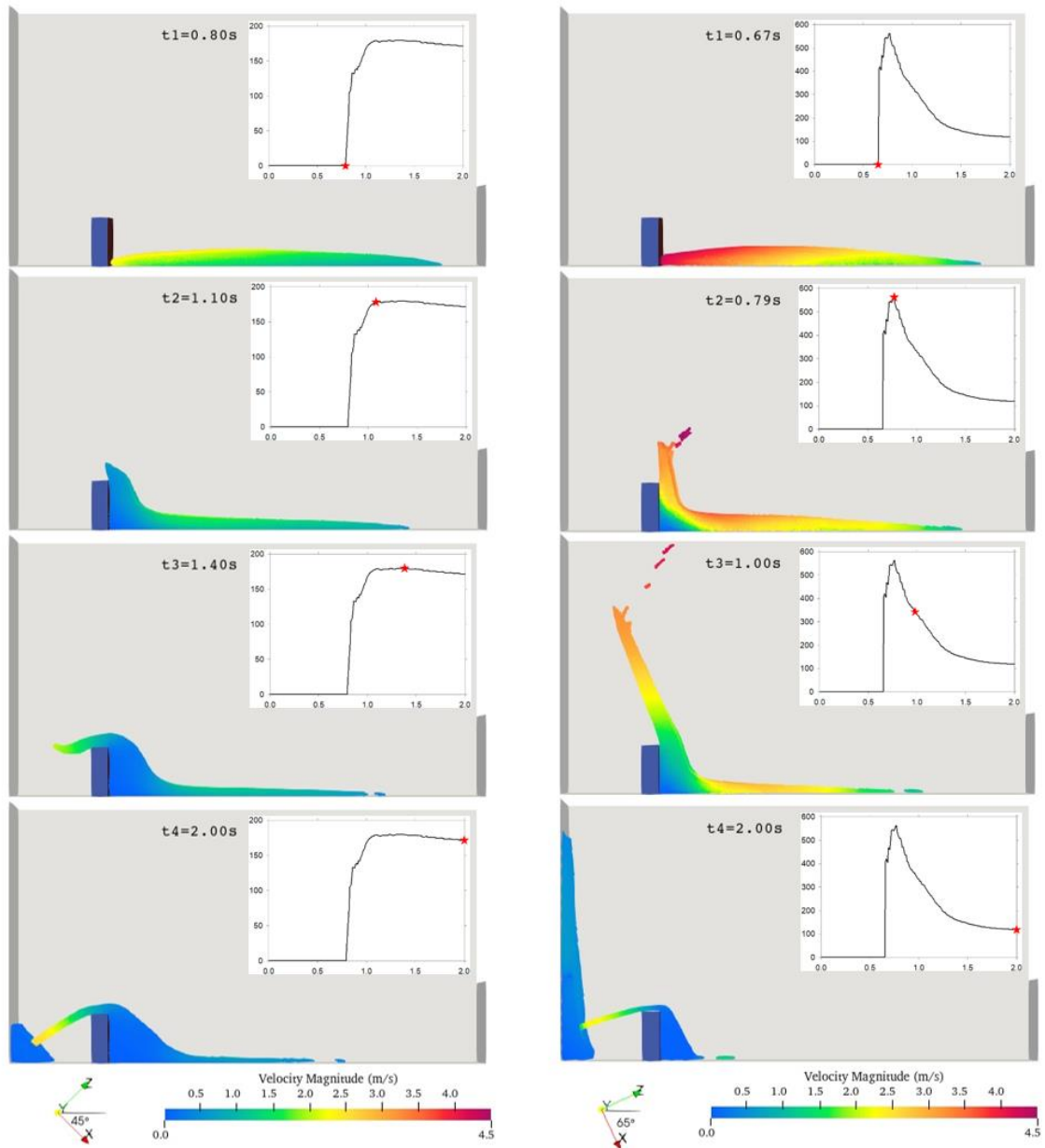
Fig. 4.6 Flow velocity field at four critical times for the flume inclined at 45° and 65°

4.4 Simulation of the Cancia debris-flow event

4.4.1 Introduction of the July 23 debris-flow event

The July 2015 Cancia debris-flow event was selected as a field case to investigate the effect of prevention structures on the propagation of a natural debris flow. The Cancia catchment (Qiao et al., 2023a) is located in the Dolomites region of the northern Italian Alps (Fig. 4.7). The outlet of the catchment is near to the Cancia village. This catchment area is composed of two sub-basins: the

Salvela basin (0.65 km^2) and the Bus de Diau basin (0.99 km^2). Over 27% area of the Salvela basin is covered by vegetation. The area ratio of bare screes in the basin is 22%, which provide a large amount of source materials for debris flows.
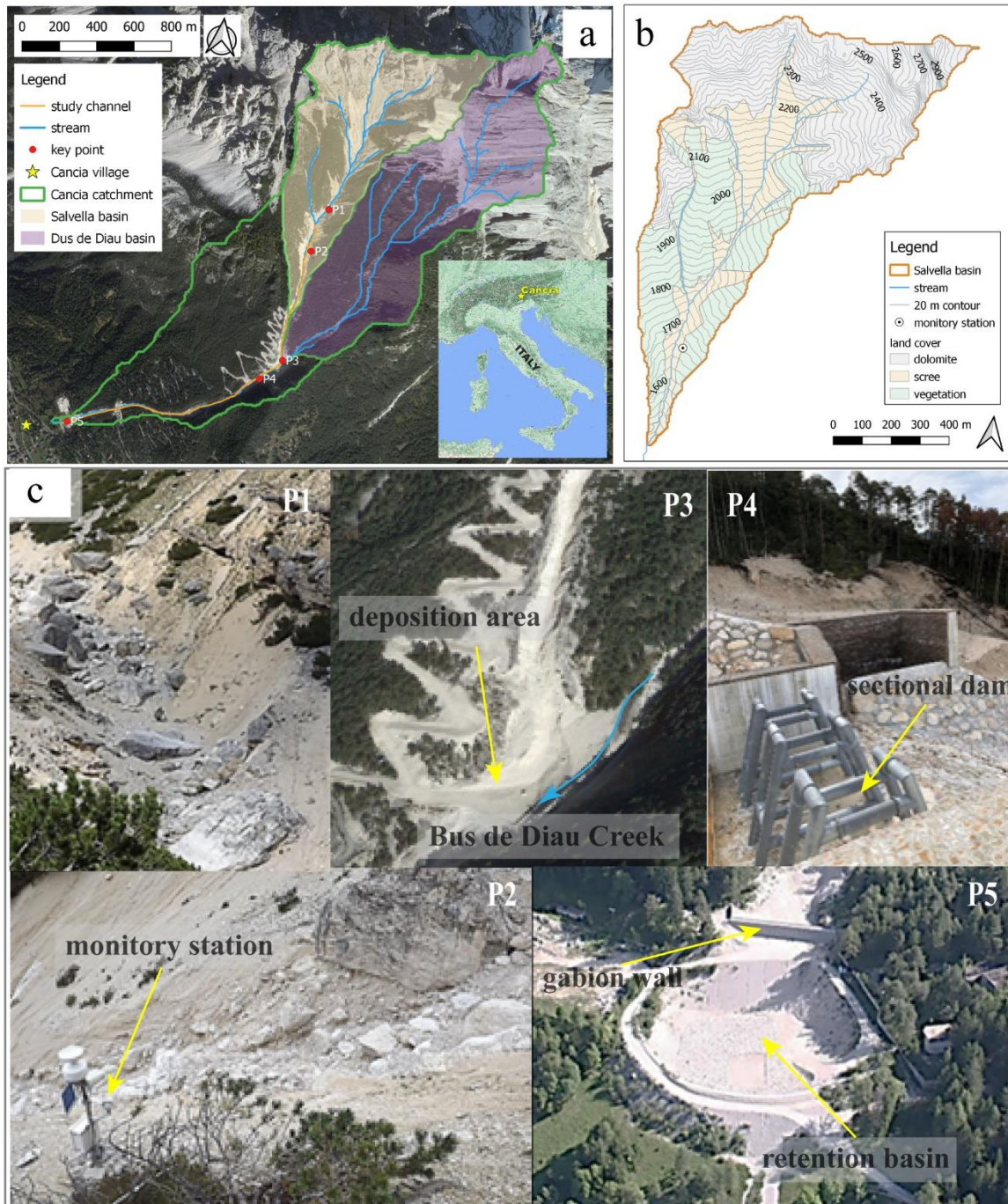
Fig. 4.7 (a) Overview of the Cancia catchment. (b) Schematic geomorphological features of the Salvela basin. (c) Detailed images of some key points along the channel

The July 2015 debris flow was triggered by a heavy rainfall with a maximum intensity of 106 mm/h. A small amount of the debris mass stopped on a deposition area (Bernard et al., 2024) built in the upper part of the channel (zone A in Fig. 4.8), while most parts continued to flow downward. The gabion wall that together with the banks acts as a retention basin. A large portion of the debris flow was intercepted by the gabion wall (Dam 3 in Fig. 4.8) located at the channel outlet, and the rest surpassed the check dam and deposited in the lower retention basin (zone C in Fig. 4.8). The debris flow channel can be divided into three regions: the initiation region, propagation region and deposition region according to the deposition characteristics of the debris flow (Fig. 4.8). The total run-out distance of this debris flow was approximately 2200 m (Qiao et al., 2023a; Simoni et al., 2020).

Fig. 4.8 Layout of the Cancia debris-flow channel and the locations of the check dams and discharge monitoring profiles in simulations

4.4.2 Simulation settings

According to one airborne laser scanning survey performed in 2011 and two series of unmanned

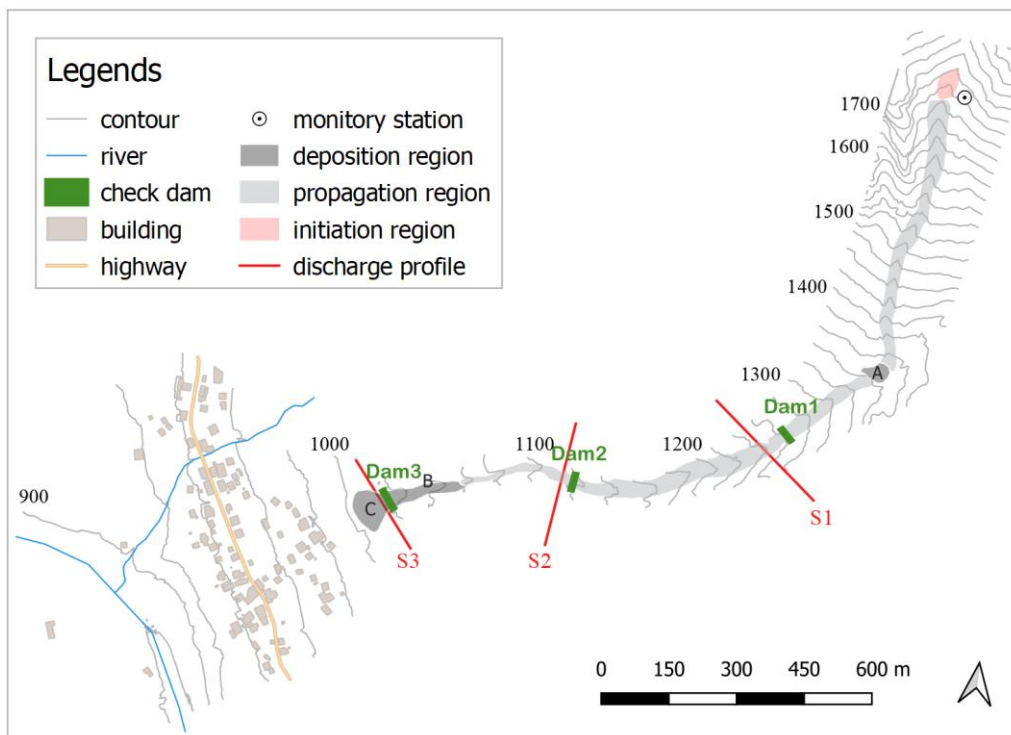aerial vehicle (UAV) aerial photographs taken shortly after the two events, a digital elevation model with a resolution of 1.0 m was obtained to build up the 3D topography of the study area. The debris flow (total volume is 28850 m^3) was discretized into 79029 fluid particles. The computational region was 2131 m long in the x direction and 1663 m wide in the y direction. The maximum time step for simulating this case was 0.02 s. Eight groups of simulations G0-G7 were carried out to study the influence of check dams (Dam1-Dam3 in Fig. 4.8) on the propagation and deposition process of the debris flow (Table 4.2). Dam3 corresponds to the gabion wall at the outlet of the channel which was constructed before the July 2015 debris-flow event. Dam1 and Dam2 are two imaginary check dams which are used to investigate the influence of check dam locations on the propagation of debris flow, in which the location of Dam1 corresponds to that of a sectional dam constructed in 2020 (P4 in Fig. 4.7c). The height of each dam is 8 m in these simulations. Meanwhile, three cross-sections (S1, S2, S3 in Fig. 4.8) were selected to investigate the effect of the check dam on the discharge of the debris flow.

Table 4.2 Configurations in different simulation groups

Simulation groups	Check dam settings
G0	Without check dam
G1	Dam1
G2	Dam2
G3	Dam3
G4	Dam1, Dam2
G5	Dam1, Dam3
G6	Dam2, Dam3
G7	Dam1, Dam2, Dam3

The main parameters used in these simulations are listed in Table 4.3. Among them, the initial values of the five key coefficients in the HBP law (m, n, μ, φ, c) were first selected based on the parameters adopted in a study area with similar geological conditions (Armento et al., 2008), and then calibrated by simulation G3 (Table 4.2) to fit the observation results of the debris-flow event.

Table 4.3 The main parameters run in the simulation of July 23, 2015 debris-flow event

Parameters	Notion	Unit	Value
Fluid density	ρ	kg/m³	2000
Inter-particle distance	d_p	m	0.7
Number of fluid particles	N_{pf}	/	79029
Number of boundary particles	N_{pb}	/	2083275
Simulation duration	t	s	450
Initial time interval	Δt	s	0.012
Coefficients in HBP law	m	/	0.15
	n	/	1.05
Dynamic viscosity	μ	Pa·s	97
Internal friction angle	φ	°	20
Cohesion	c	kPa	4

4.4.3 Simulation results

4.4.3.1 Run-out characteristics of the July 23 debris flow event

The simulated velocities and distributions of the July 23 debris-flow event at different times are shown in Fig. 4.9. Overall, the simulated run-out distance and inundated area of the sediments in case G3, which represents the field conditions at the time of the event, agree well with the field observations (Simoni et al., 2020). The simulated maximum average velocity of the flow front is approximately 23 m/s. At around 38 s, the flow front reaches the upper flat deposition area and part of the debris mass deposits here. The rest of the material continues downstream and the front of the debris flow reaches Dam3 at approximately 260 s. Then the flow impacts the dam, and a great amount of debris mass is intercepted by the dam. Finally, after around 30s, the debris flow surpasses Dam 3 and accumulates in the retention basin.
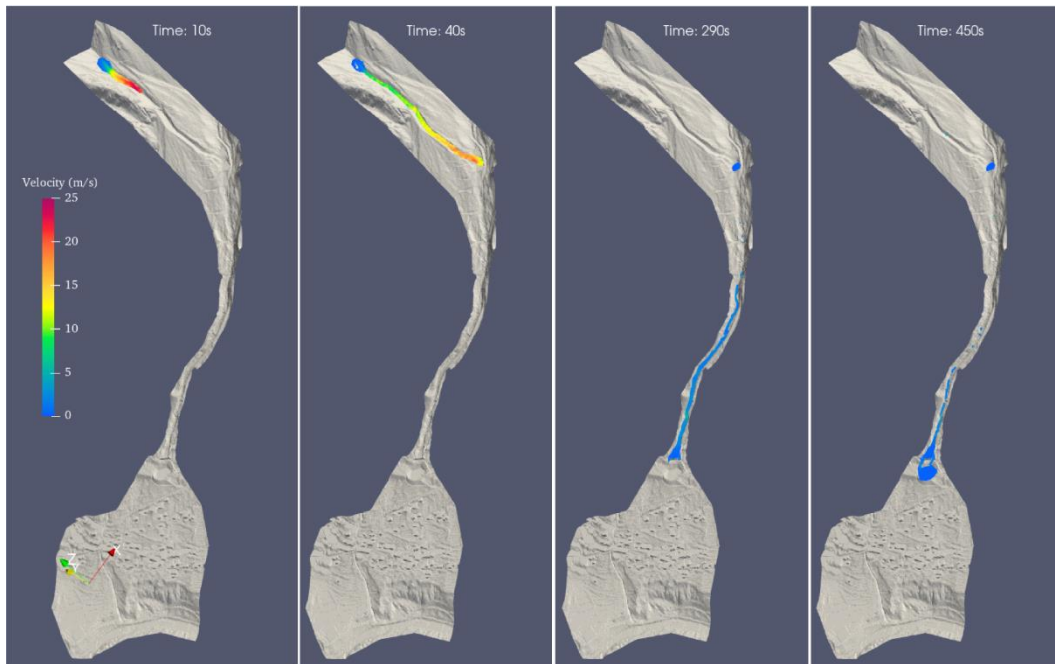
Fig. 4.9 The simulated propagation process of July 23, 2015 debris flow

Further details on the run-out characteristics of the debris flow, the average velocity and displacement of the flow front are presented in Fig. 4.10. As can be seen, the prevention structures in the main channel (i.e., the flat deposition area, Dam3 and the retention basin) have significant influences on the run-out process of this debris flow. As the flow front approaches these structures, the flow front velocity appears to drop sharply and the increasing of displacements becomes correspondingly slower. Additionally, the complicated 3D topography of the flow channel can cause the velocity fluctuations of the debris flow.

Fig. 4.10 Average velocity and displacement of the flow front in G3 simulation (t1, t2 and t4 are the time when the debris flow reaches the flat deposition area, Dam3 and the retention basin, respectively. t3 is the time when the debris flow surpasses over Dam3.)

4.4.3.2 Influences of the check dams on the run-out process of debris flow

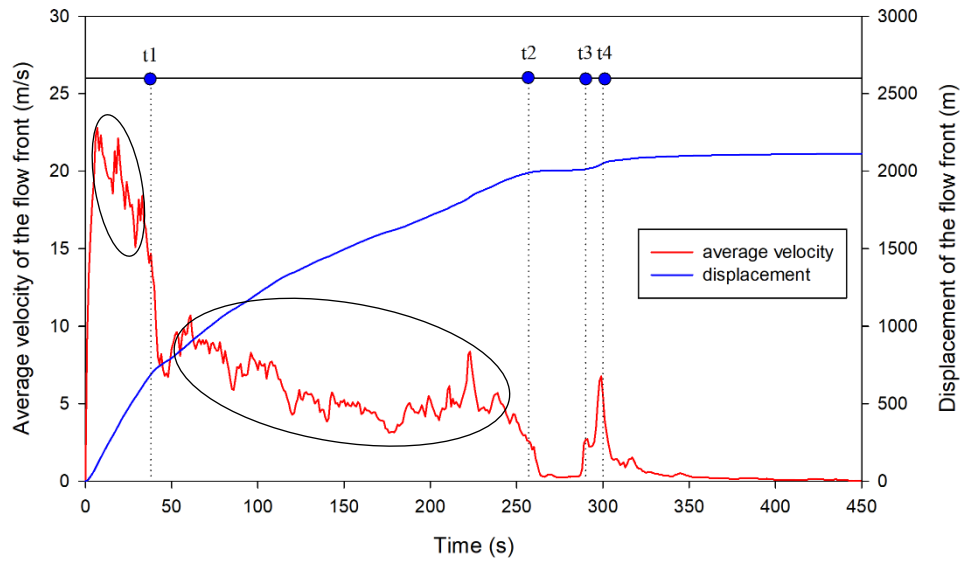The simulated final depth distributions of the debris flow in different check dam conditions are shown in Fig. 4.11. In G0 (no check dams present), a large amount of debris mass flows past the retention basin and inundates the Cancia village. Although in G1 the final inundated area is smaller than that of G0, the prevention effect is significantly lower than that of G3, which means that only setting a check dam in the upper part of the channel may not prevent a debris flow like the July 23 event. This is probably caused by two reasons. Firstly, the width of upstream channel is narrower than downstream, and it has a relatively steeper slope than the downstream channel. Therefore, the capacity of reservoir upstream tends to be smaller. The second reason is that the velocity of flow front is relatively high when it impacts Dam1, so more debris mass jumps over the check dam. The simulation results of G4 and G6 also indicate that check dams constructed downstream are more effective than those constructed upstream. The average deposition thickness in the retention basin in G3, G6 and G7 is about 0.8 m, 1.7 m and 2.4 m less than that in G0. This illustrates that the prevention effect could be enhanced by building multiple dams along the flow path.
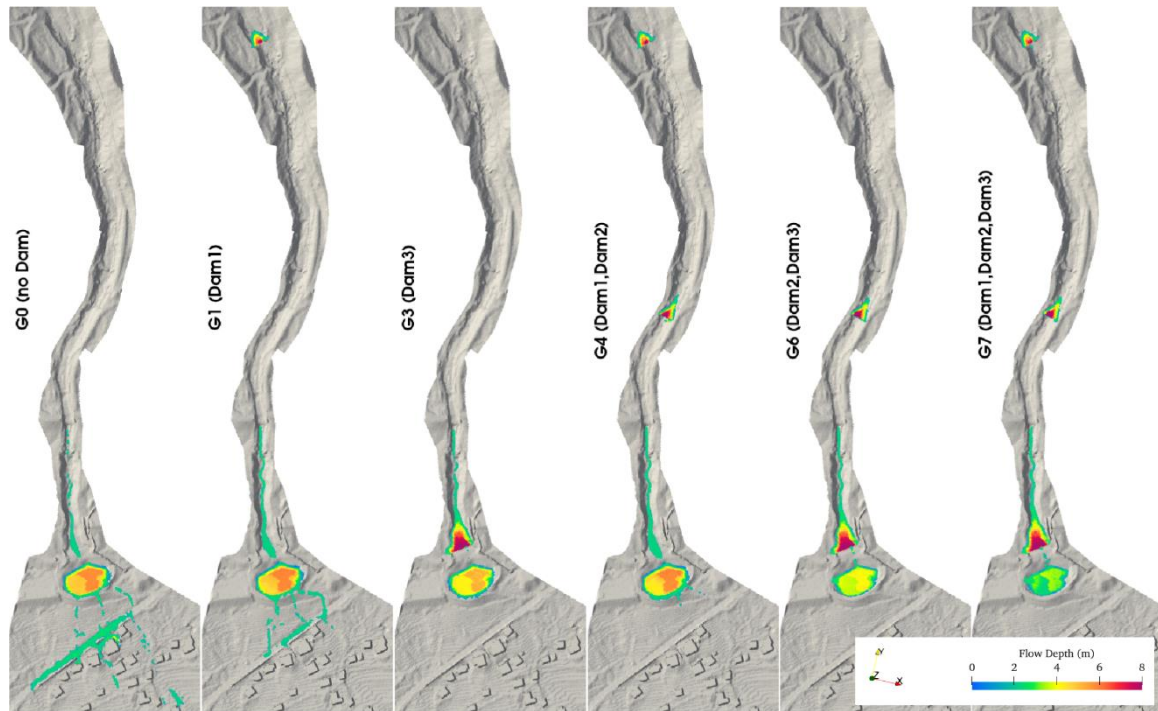
Fig. 4.11 Comparison of the final flow depth distributions in different simulation groups

Three cross-sections (S1, S2 and S3 in Fig. 4.8) just downstream of the check dams (Dam1-Dam2-Dam3) are selected to investigate the effect of check dam location on the discharge of the debris flow. Two characteristic parameters (the peak discharge Q_m and the time t_0 when the flow front arrives at the cross-section) are defined to compare the influence of the check dam on the discharge of debris flows in different simulation groups. Fig. 4.12a shows that the time t_0 increases noticeably due to the impeding effect of Dam1, and similar variations are only observed in S3 (Fig. 4.12b). Meanwhile, a peak value drop is also observed in these cases. Also in this case, the performance of Dam3 (Fig. 4.12b) is significantly better than Dam1 (Fig. 4.12a) because of the lower flow velocity and the gentler topography downstream. Fig. 4.12c and Fig. 4.12d illustrate the results in the case of two and three dams along the flow path, respectively. As can be seen, the performance of multiple dams is better than that of single dam. The estimated characteristic values of all simulation groups are listed in Table 4.4.

Fig. 4.12 Influence of the check dam on discharge time series in three sections (S1, S2 and S3)

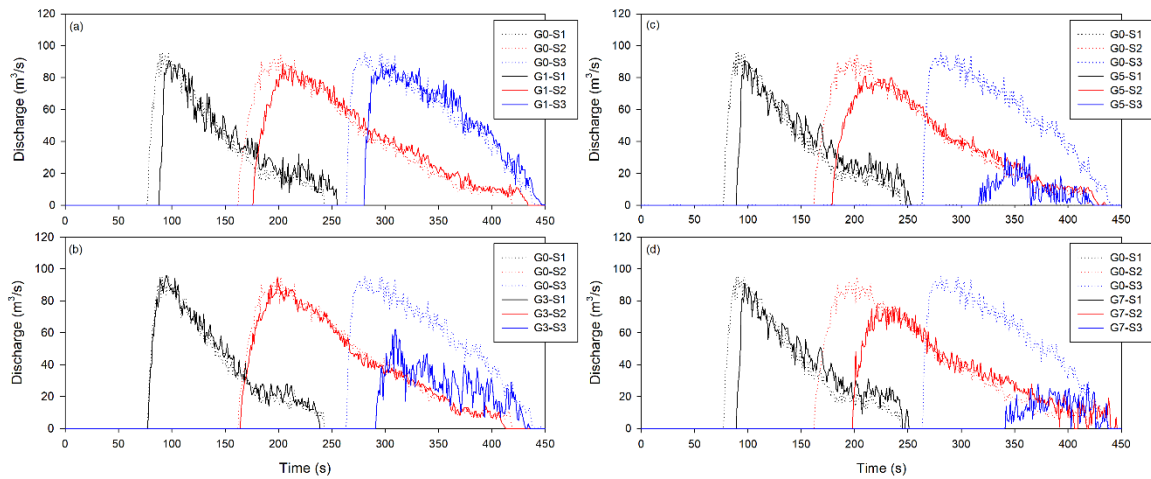**Table 4.4** The estimated characteristic values in all simulation groups

Simulation groups	The peak values Q_m (m³/s)			The initial time t_0 (s)		
	S1	S2	S3	S1	S2	S3
G0	95.866	95.061	96.009	78	163	264
G1	90.909	88.8658	88.924	89	177	281
G2	95.866	85.100	86.029	78	180	282
G3	95.866	95.021	62.096	78	165	292
G4	90.909	79.041	84.005	89	194	300
G5	90.922	81.086	32.971	90	179	317
G6	95.866	82.005	30.052	78	183	317
G7	90.922	77.094	28.048	90	199	342

A series of pressure monitoring points were set on the surface of three check dams to record the average impact pressure of debris flow on the check dam. The simulated impact pressures are shown in Fig. 4.13. The impact pressure curves at the three dams are very different. The impact pressure curves of Dam1 and Dam2 consist of obvious three stages (acceleration, deceleration and stabilization stages), while the deceleration stage of the impact pressure curves at Dam3 is not obvious. Additionally, the acceleration limb and the deceleration limb of Dam2 are significantly gentler than those of Dam1. These results suggest that the check dams upstream are likely to suffer from higher impact force, and this is because the flow velocity upstream is relatively larger than that downstream. Furthermore, it also shows that the upstream check dam can slightly reduce the

peak impact pressure of the debris flow acting on the downstream check dam.
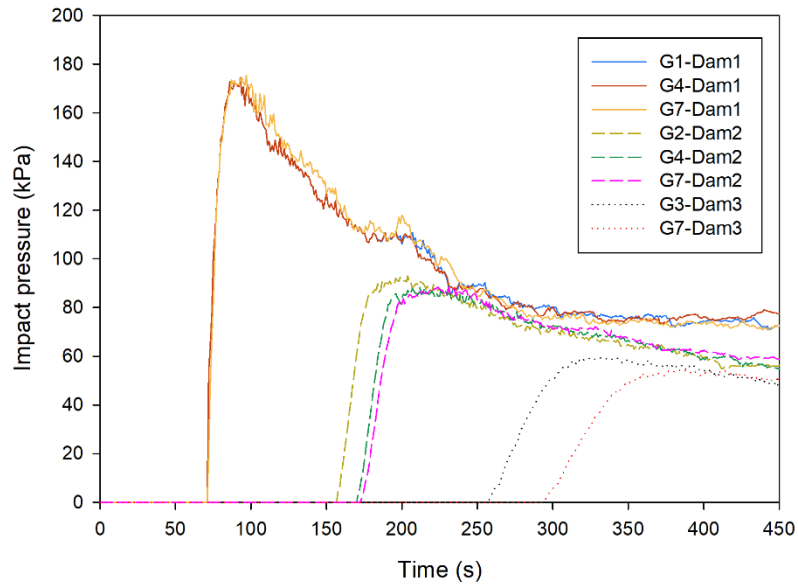
Fig. 4.13 The estimated impact pressure time series in the different simulation groups

4.5 Discussion

The simulation results unambiguously demonstrate the significant effectiveness of check dams in reducing the flooded area, debris flow speed, and peak discharge. In Cancia, these structures were employed in conjunction with other preventative measures, such as a flat deposition area and a retention basin, to achieve optimal results. The use of multiple structures in debris flow basins is a common practice to effectively mitigate risks. In order to investigate the interaction mechanisms of these structures on the propagation of debris flow, we carried out additional numerical flume tests in eight different conditions. The schematic diagram of the numerical tests is shown in Fig. 4.14. P1 and P2 are the locations along the flow path where prevention structures may be installed While the simulation setups are listed in Table 4.5.
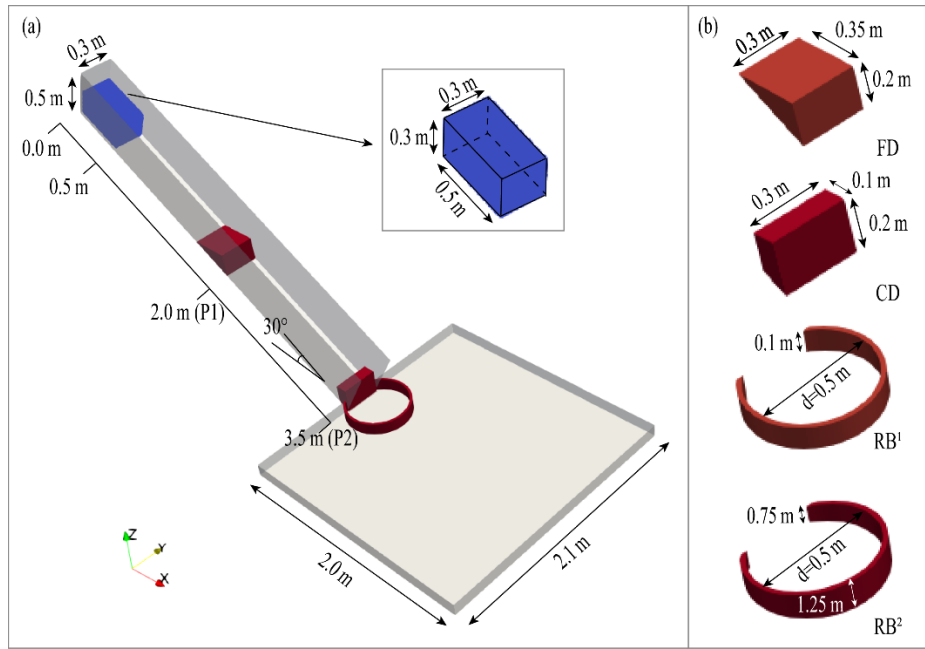
Fig. 4.14 Schematic diagram of (a) the flume model and (b) structures (FD: Flat Deposition area; CD: Check Dam; RB^1: Retention Basin with same retaining wall height; RB^2: Retention Basin with increased retaining wall height)

Table 4.5 Structure settings for different simulation groups (FD=flat deposition area; CD=check dam; RB=retention basin)

Simulation Groups	Structure settings
C0	No structure
C1	FD in P1
C2	CD in P1
C3	CD in P2
C4	RB^1 in P2
C5	RB^2 in P2
C6	FD in P1 and CD in P2
C7	FD in P1 and RB^1 in P2

In these simulations, the SPH particle spacing was 0.01m, corresponding to 35235 flow particles. The density of the debris flow was 2000 kg/cm^3, and the other parameters used in the simulation are listed in Table 4.6. The yield stress τ_y used in the original SPH model was calibrated by ensuring that the flow reaches the outlet of the flume at the same time as the modified SPH model.

Table 4.6 The main parameters in the dynamic simulation

Parameters	Original SPH model	Modified SPH model

	Notation	Value	Notation	Value
Coefficients in HBP law	m	100	m	100
	n	1.05	n	1.05
Dynamic viscosity	$\mu(\mathrm{Pa}\cdot\mathrm{s})$	1	$\mu(\mathrm{Pa}\cdot\mathrm{s})$	1
Yield strength	$\tau_y(\mathrm{kPa})$	1.3	$\varphi(°)$	28
			$c(\mathrm{kPa})$	0

4.5.1 Performance of the modified SPH model in simulating debris flow deposition

The original SPH model and the modified SPH model are used to simulate the run-out process of a numerical debris flow test in condition C1. The simulated final flow depths are shown in Fig. 4.15, where the deposit of the debris flow simulated by the original SPH model is thinner and flatter than that simulated by our modified SPH model. The flat deposition area stops more debris mass in the modified SPH model. The simulation results of the modified SPH model fit better with the real debris flow in which the frictional dissipation in the flow is non-ignorable.
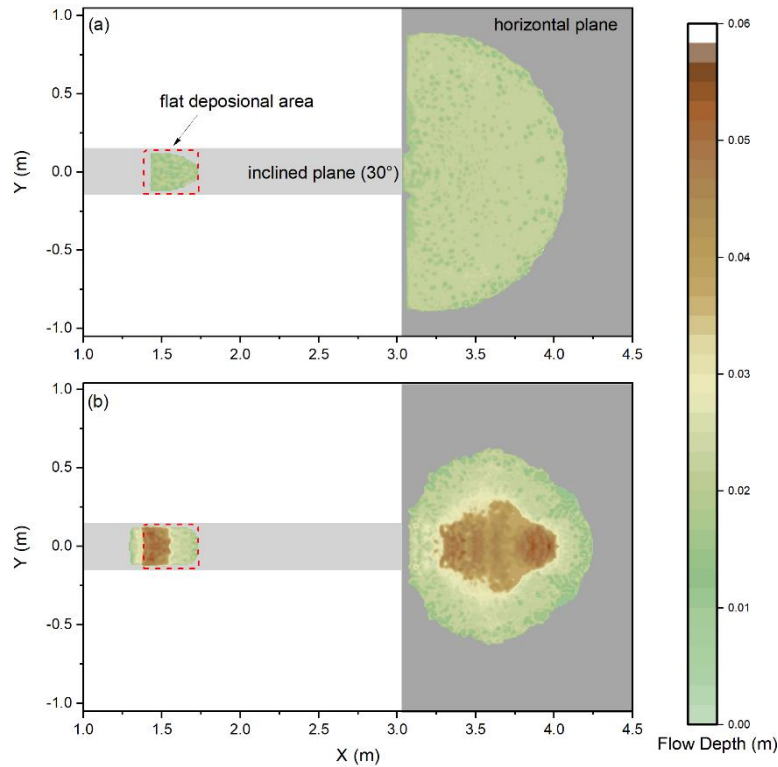
Fig. 4.15 Flow depth of final deposition obtained by (a) the original SPH model and (b) the modified SPH model

4.5.2 Influence of different structures on debris flow propagation

The average velocity of the flow front and the discharge of the flow at the outlet of the flume in C0-C2 are illustrated in Fig. 4.16. Results show that both the flat deposition area and check dam contribute to decreasing the kinetic energy of the flow and reducing the peak discharge. The two types of structures achieve these results through different mechanisms. In a check dam (C2), the kinetic energy of the flow front is mainly lost due to the collision of the flow front and the dam. Meanwhile, the discharge dramatically reduces because a large amount of debris mass is intercepted by the dam. In a flat deposition area (C1), the decrease of the average velocity of the flow front is mainly caused by the friction dissipation in the flow, although a small part of the flow material is deposited there.

Fig. 4.16 (a) Average velocity of flow front and (**b**) discharge time series at the outlet of the flume

The impact forces acting on the check dams in different simulation groups are shown in Fig. 17. The magnitude of impact force acting on the check dam is rela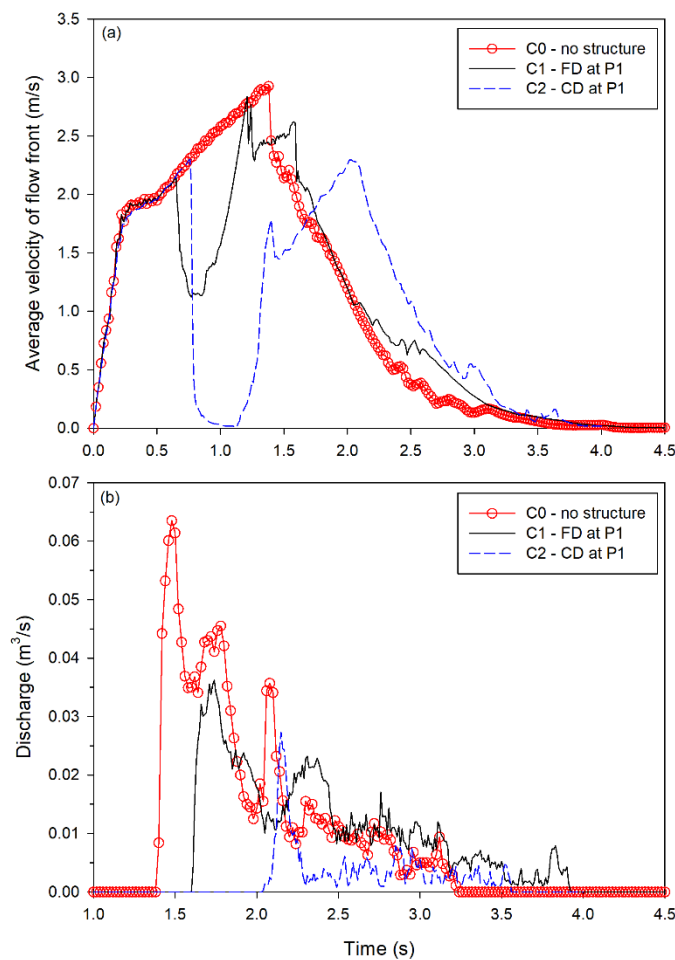ted to the velocity of the flow front. Since the flow is accelerating from P1 to P2 (Fig. 16a), the peak impact force of C3 is greater than that in C2. In each simulation, the impact force eventually converges to the same stable value at around 100 N. If a flat deposition area is installed in front of the check dam (C6), part of the kinetic energy of the flow is lost before impacting the check dam. Thus, the peak impact force exerted on the check dam can be significantly reduced.
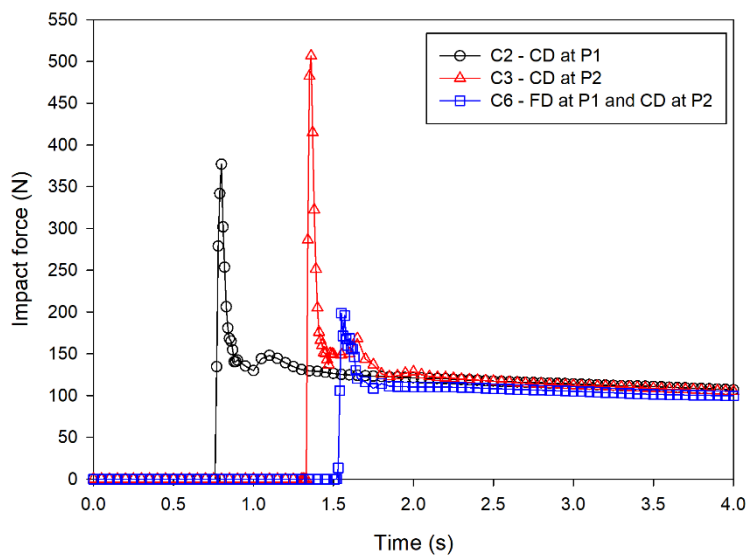
Fig. 4.17 Comparison of impact force time series for different simulation groups

The simulated inundating areas of the groups with and without the retention basin (C0 vs C4 and C1 vs C7) are presented in Fig. 4.18. It can be concluded that the retention basin has the ability to reduce the affected area and shorten the run-out distance. In addition, the comparison of C0 and C1 (or C4 and C7) shows that the flat deposition area also contributes to reducing the run-out of the flow front (Fig, 4.18b), but has little effect on the reduction of the inundating area (Fig, 4.18a) in the specific case considered. To further study the influence of retention basin dimension on debris flow propagation, we modified the height of the retaining wall of the retention basin as shown in Fig. 4.14b. Compared with the results of C4, a smaller inundated area and a shorter run-out distance are observed in simulation C5. It indicates that the improved retention basin is more effective in

debris flow mitigation when the engineering quantity is similar. Based on the analysis above, the main function of retention basin is to adjust the inundating area and delay the arrival time of the debris flow.
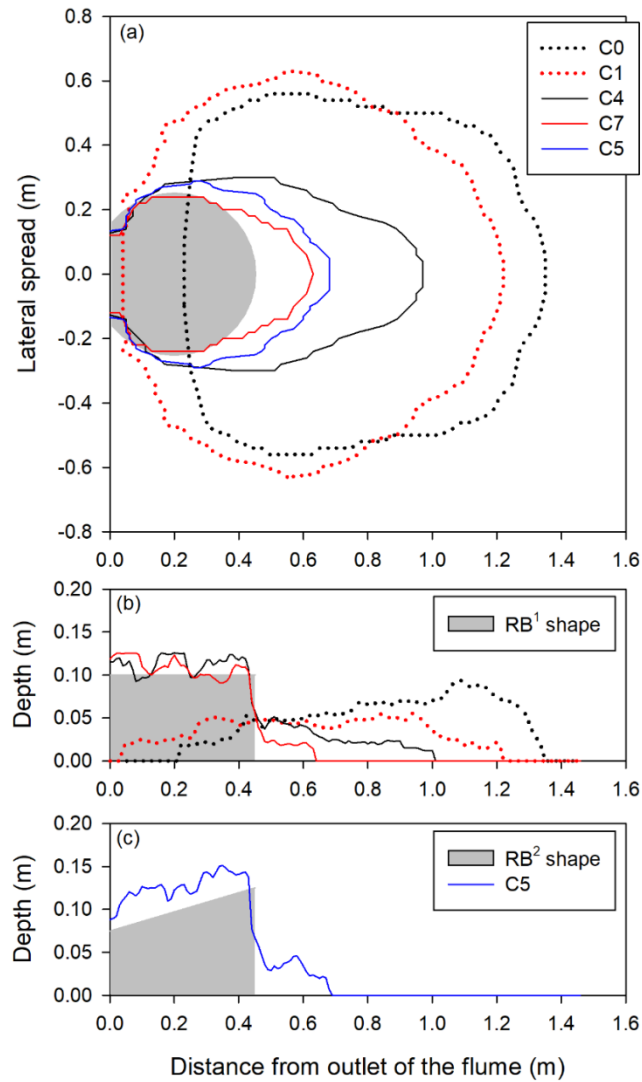
Fig. 4.18 Simulation results of the final debris flow deposition: (**a**) Plan view; (**b**) and (**c**) profile view

In summary, the three different structures exhibit different behavior. Each one has a significant advantage in mitigating the debris flow. Flat deposition areas are often constructed along the debris flow channel with high slopes, providing a gentler area for the flow to spread out and dissipate the kinetic energy. Check dams are mainly used to reduce debris flow intensity (peak discharge and debris flow volume). Since the impact force acting on check dams is related to the kinetic energy of

the flow front. Retention basins are usually built at the outlet and upstream of the outlet before an open check dam to reduce the impact area of the debris flow and prevent it from causing damage to downstream infrastructures. Additionally, the shape of retention basin can be designed based on the flow direction to improve its performance in mitigating debris flow.

4.6 Concluding remarks

A novel SPH model adopting the modified HBP constitutive law was established in this study to simulate debris flow-structures interaction. Two benchmark experiments were used to validate our model. Furthermore, a real debris-flow event was analyzed using the model and the prevention mechanisms of various structures are discussed. The following conclusions can be obtained:

(1) The simulation results of column collapse and flume experiments demonstrated that our modified model, which introduces friction into a HBP rheological law, can more accurately predict deposition process of debris flow. And the simulation results of flume experiments illustrated the effectiveness of the modified model in predicting the interaction between debris flow and structures. A peak impact force is observed in the steeper flume slopes (55°, 60° and 65°), excepting the two flatter flume slopes of 45° and 50° where the impact force appears to increase continuously to a stable impact value. Moreover, two totally different impact mechanisms are observed in the sand flume models of 45° and 65°. The impact mechanism of the 45° inclination flume resembles a granular bore regime while it becomes an airborne jet in the 65° flume.

(2) The simulation results of the July 23 debris-flow event in the Cancia basin (Italian Alps) show that the peak impact pressure varies with the location of check dam. The impact pressure in the upper part of the channel appears to be greater than that downstream, which can be explained by the steeper terrains and faster flow velocity upstream compared to downstream.

(3) Different prevention structures have different mechanisms when they interact with debris flows. The flat deposition areas mainly contribute to decreasing the flow front velocity and are usually built in the upper part of the channel. The main function of check dams is to reduce the discharge downstream by intercepting the debris mass. Retention basins are often constructed at the outlet of the channel and upstream of the outlet before an open check dam to prevent debris flows from flooding the surrounding infrastructures, and a better mitigation effect can be achieved if we consider the flow direction when designing the shape of the retention basin. Our modified SPH model has the potential to be utilized in guiding the optimization design of these prevention structures in debris flow gullies.

5. Entrainment mechanism of flow-like landslides

The term "entrainment" in the context of landslides refers to the process by which additional material, such as rocks, soil, or debris, is mobilized and incorporated into the moving mass of the landslide. Bed material entrainment during a landslide plays a significant role in determining the mobility and dynamics of the landslide. Researchers and engineers use mathematical models, field measurements, and laboratory experiments to study and quantify bed entrainment in order to make informed decisions about river management, sediment transport, and ecosystem health. This section aims at offering new insights into the mechanisms and effects of entrainment processes in loess landslides with the help of advanced numerical simulations.

5.1 Introduction

Flow-like landslides typically entrain the erodible bed material, which has significant influence on the mobility of landslides (Hungr and Evans, 2004; McDougall and Hungr, 2004; Sovilla et al., 2006; Sovilla and Bartelt, 2002). Entrainment could either accelerate or decelerate the flow (i.e., increase or decrease its mobility) depending on the properties of the erodible material as well as on the depth of the bed material and on the dynamics of the flow (Mangeney et al., 2010). Bed material entrainment alters the speed and hence the run-out distance of flow-like landslides. In the last two decades, field measurements (Berger et al., 2011; Sovilla and Bartelt, 2002), physical model tests (Bates et al., 2016; Bates and Ancey, 2017; Crosta et al., 2017; Egashira et al., 2001; Farin et al., 2014; Iverson et al., 2010; Mangeney et al., 2010) and numerical simulations (Baggio et al., 2021; Choi and Nikooei, 2023; Guo et al., 2022; McDougall and Hungr, 2005; Nikooei and Manzari, 2021; Qiao et al., 2023a; Shen et al., 2019a; Sovilla et al., 2006) have been used to understand the entrainment process of flow-like landslides. However, the entrainment phenomenon involved in the landslide run-out process is sophisticated and not yet well understood.

Numerical modelling has become a powerful tool for investigating the interactions between the

landslide and the bed materials due to its ability to capture internal deformations. In the last two decades, several particle-based numerical models have been developed to study the entrainment of bed material due to their advantages in dealing with large deformation problems in geomechanics. For instance, a two-phase numerical model based on Smoothed Particle Hydrodynamics (SPH) was applied to simulate liquid-sediment scour (Fourtakas and Rogers, 2016). The interaction between a flowing granular material with an entrainable granular bed was numerically studied, with mixing of the material at the flow-bed interface (Nikooei and Manzari, 2021). A 2D SPH model incorporated with a regularized viscoplastic (Herschel–Bulkley) rheology was developed to study the viscoplastic surges over mobile beds (Goodwin et al., 2023). Various erosion and entrainment behaviors in snow avalanches are analyzed based on the material point method (MPM) and an elastoplastic constitutive law developed for snow (Li et al., 2022). A bed softening model was embedded into 3D MPM model to effectively simulate debris flow entrainment (Vicari et al., 2022). And an PFEM model was developed to model bed erosion problems (Oñate et al., 2006). A novel PFEM that can successfully predict the local scouring of an erosion material in the presence of fluid flow was proposed by Galano et al., (2021). These works mainly focused on the bed entrainment caused by debris flows and snow avalanches, and most of the studies are simulations at the experimental level. To the best of our knowledge, few numerical models addressed entrainment issues of flow-like loess landslides.

It is known that internal friction angle plays an essential role in the dynamics of loess landslides. Ignoring the effects of the friction dissipation is associated with overprediction of the run-out distance of these phenomena. In this study, the improved SPH model proposed by Qiao et al., (2023b) was used to accurately analyze the entrainment phenomena associated with the Ximiaodian loess landslide (China).

The rest part of this chapter is organized as follows: Section 5.2 briefly overviewed the original SPH model and the improved SPH model used in the following simulations. In Section 5.3, simulations of viscoplastic flow over the erodible beds with different yield strengths were

conducted and then validated by the experimental results. In Section 5.4, the Ximiaodian landslide, a typical flow-like loess landslide, was selected to analyze the entrainment process and discuss the influence of the internal friction angle on the terrace entrainment. Finally, some insightful conclusions were drawn in Section 5.5.

5.2 Methodology

In this research, we select two distinct flows to study the entrainment phenomena. As far as we are concerned, the HBP constitutive model is more suitable to accurately mimic the rheology behavior of a viscoplastic flow. Thus, we performed a simulation of viscoplastic flow over the erodible beds using the SPH model combined with the HBP rheology model. However, an improved HBP law considering friction dissipation is adopted to simulate the interaction between the loess deposits and the terrace sediments. Both models were introduced in the previous chapter (see Section 4.2). Fig. 5.1 illustrates the differences of the two models in solving the momentum equation.
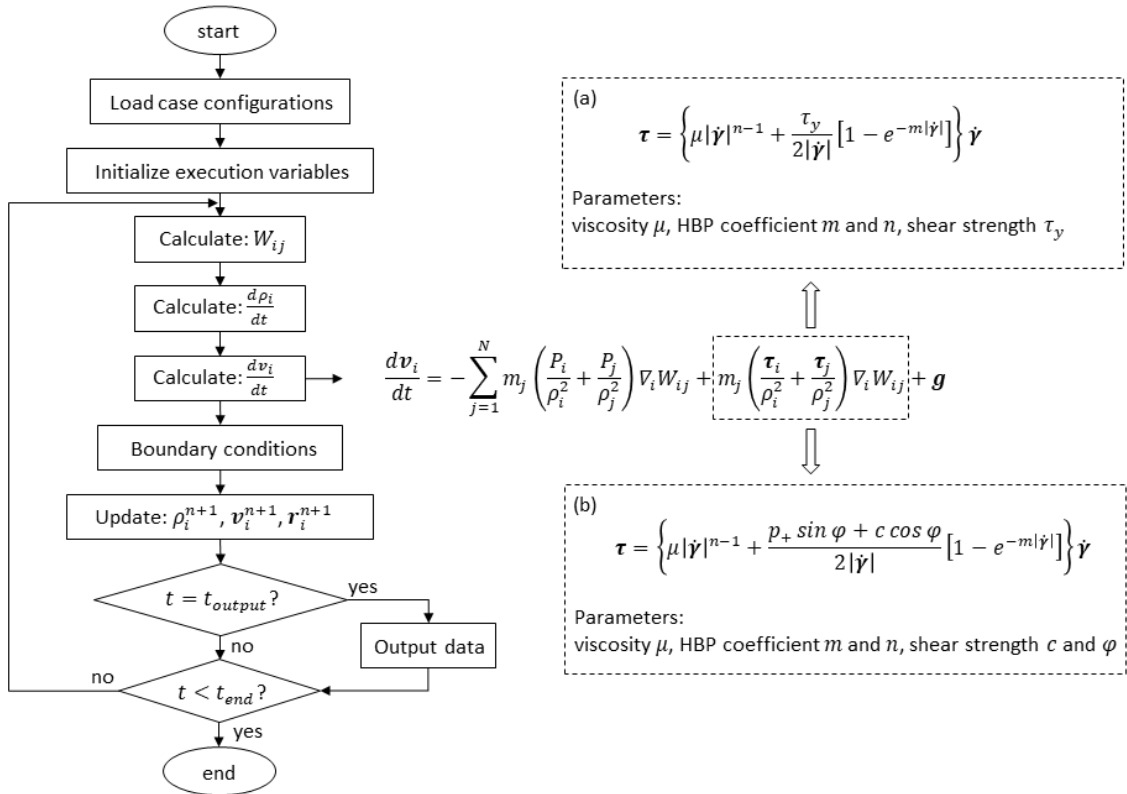

Fig. 5.1 Calculation process of the SPH model coupled with (**a**) the original HBP law and with (**b**) improved HBP

5.3 Simulation of viscoplastic flow over the erodible beds

5.3.1 Model verification

In the experiment of (Bates and Ancey, 2017), a viscoplastic gel called Carbopol Ultrez 10 was released onto different inclined flumes with an erodible bed to study basal entrainment of viscoplastic fluid. Experiments 20-6Ca and 20-6Ra were used to validate the performance of the SPH model in simulating the basal entrainment phenomenon. Fig. 5.2 schematically shows the geometric configuration of experiments 20-6Ca and 20-6Ra of (Bates and Ancey, 2017). The flume is inclined at 20° with a region of erodible bed 6 mm deep by 300 mm long. The distance between the initial flow and the erodible bed l_{step} is set to 900 mm to ensure that the viscous force is greater than the inertial force when the flow interacts with the erodible bed. The flow volume per unit width was 0.03 m^2, and the density ρ was 1000 kg/m^3.

According to (Bates and Ancey, 2017), a Herschel–Bulkley constitutive is fitted to the rheological data of experimental fluid. Therefore, rheological parameters are adopted in the simulation are as follows: yield stress is $\tau_y = 58$ Pa, viscosity is $\mu = 35$ Pa·s^n, and $n = 0.33$. In this study, we adopted HBP model with $m = 100$ to avoid the numerical divergence problem when shear strain rate $\dot{\gamma}$ in HB model approaches 0 (Fig. 5.3).
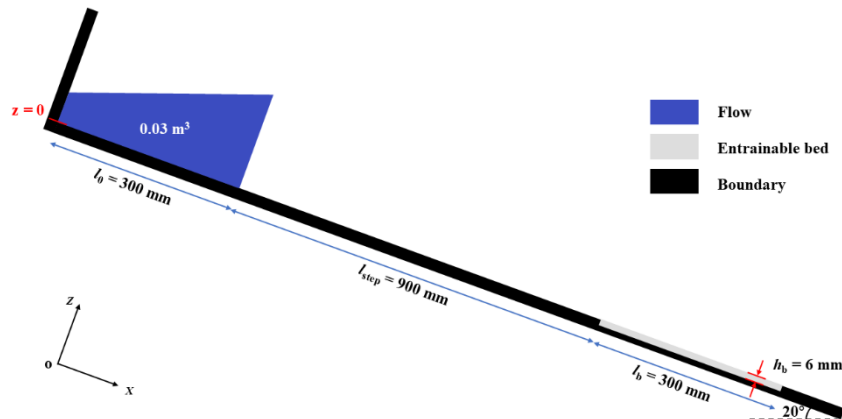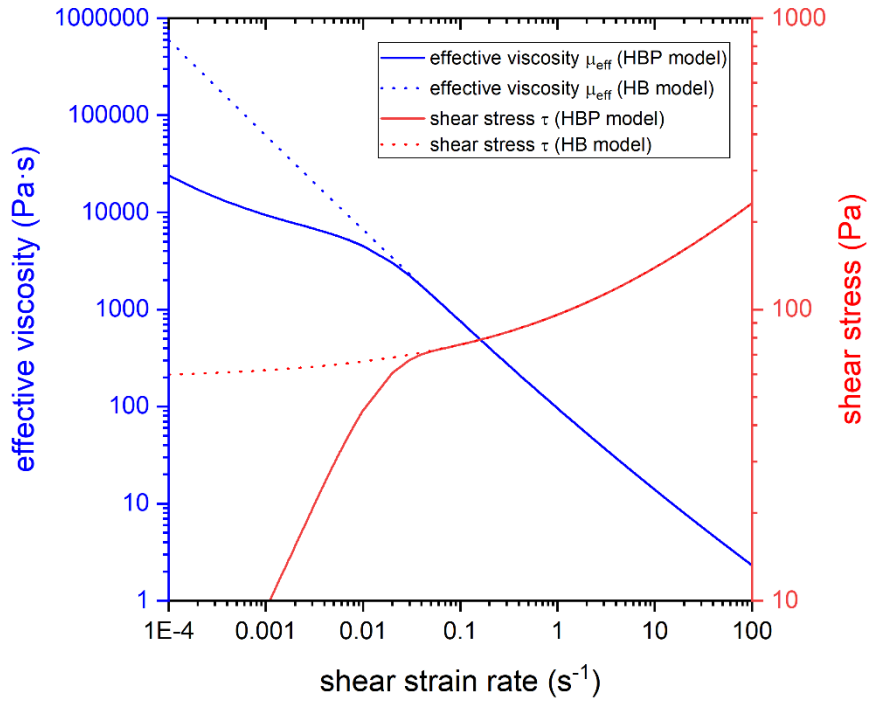
Fig. 5.3 The HBP rheological model used in numerical simulation of experiment 20-6Ca

In our simulations, the initial flow and the erodible bed were modeled by 29755 and 1794 fluid particles with an initial particle spacing of 1 mm. According to Bates 2017, the same materials were chosen in experiments 20-6Ra and 20-6Ca. Note that the flow and the erodible material of experiment 20-6Ca are rhodamine-tagged seeds. However, in experiment 20-6Ra, only the flow is labeled to observe the flow-bed interface.

Fig. 5.4 compares the flow-bed interface between experiment 20-6Ra and numerical results from our SPH model. The maximum downward penetration of the flow is detected at approximately 12 mm from the step in the simulation, which is in good agreement with experimental results. However, the maximum depth of the flow-bed interface obtained by simulation (2.67 mm) is slightly less than that observed in the experiment (about 3 mm). Both images show the intersection of the flow-bed interface and the free surface (point K) at $x \approx 60$ mm, and the mixing flow front (point F) at $x \approx 105$ mm.
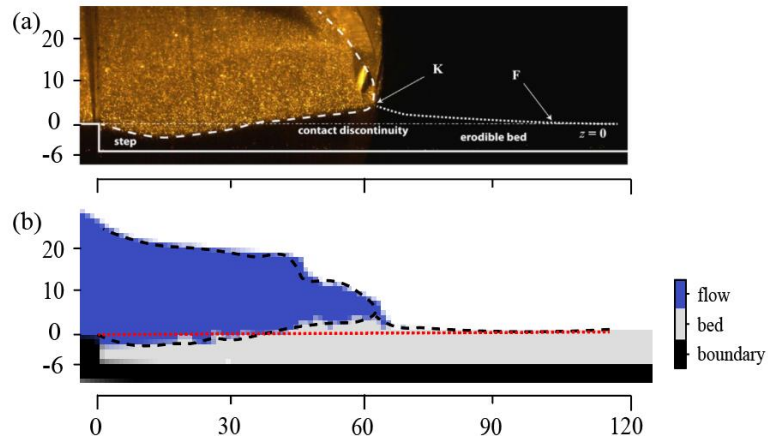
Fig. 5.4 Comparison of experimental and simulated results of the flow-bed interface

Fig. 5.5 shows that the numerical model reproduces the geometry characteristics of the mixing flow relatively well. Intersection point K moves forward to $x \approx 135$ mm, which corresponds to the "dimple" at the free surface upstream of the combined flow front. Compared with Fig. 5.4, greater amounts of bed materials are entrained by the incoming flow, resulting in farther reach of the mixing flow (point F). Additionally, the flow-bed interface near the step ($x < 60$ mm) becomes almost horizontal, while a significantly inclined interface is observed in the $60 \leq x < 135$ mm region.
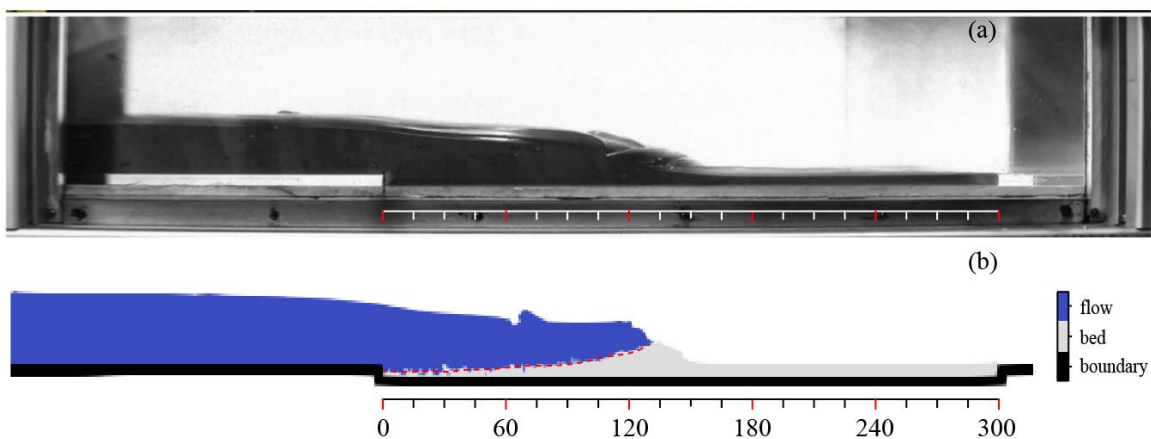
Fig. 5.5 Comparison of free surface between experiment 20-6Ca and numerical simulation

5.3.2 Influence of the erodible bed on flow mobility

To investigate the influence of the erodible bed on dynamics of viscoplastic flow, six tests are simulated using the resent SPH model. As listed in Table 5.1, the same incoming flow over four different beds is investigated. It is worth noting that we set $\tau_y = 999\ \text{Pa}$ to represent a rigid bed in the simulation. Fig. 5.6 compares the position of the mixing flow front in different bed conditions. The front position $x_{F(\text{erodible})}$ (Flow front position with entrainment) has been plotted as a function of the position $x_{F(\text{rigid})}$ (Flow front position in the absence of entrainment). In G1, both flow and bed are made of the fluid with the same shear strength ($\tau_{y,flow} = \tau_{y,bed} = 58\ \text{Pa}$), the erodible bed slightly accelerates the flow relative to the rigid case (G0). For beds with lower strength (G2 and G3), the erodible bed significantly accelerates the flow relative to G0. However, beds with higher yield strengths (G4 and G5) exhibit a significant mobility reduction relative to G0. As illustrated by Fig. 5.6, when the flow front of G0 reaches the end of the erodible layer, the flow fronts of G1, G2 and G3 have left the erodible zone, whereas the flow fronts of G4 and G5 still stay in the erodible zone. The distances from the flow front of G1-G5 to the end of the erodible zone (x=1.5 m) are 2.1 cm, 6.6 cm, 11.6 cm, -3.9 cm and -4.5 cm respectively. These results indicate that whether the bed increases or reduces the mobility of the flow depends on the strength of the erodible bed material with which the flow interacts. Moreover, it can be seen that once the flow front passes through the erodible zone and interacts with the rigid bed, the development trend of curves (G1, G2 and G3) can be approximately regarded as parallel to the dashed black reference line.

Table 5.1 Strength parameters of materials in different simulation groups

Yield stress of materials τ_y (Pa)	Simulation Groups					
	G0	G1	G2	G3	G24	G5
Flow	58	58	58	58	58	58
Bed	999	58	38	18	78	98
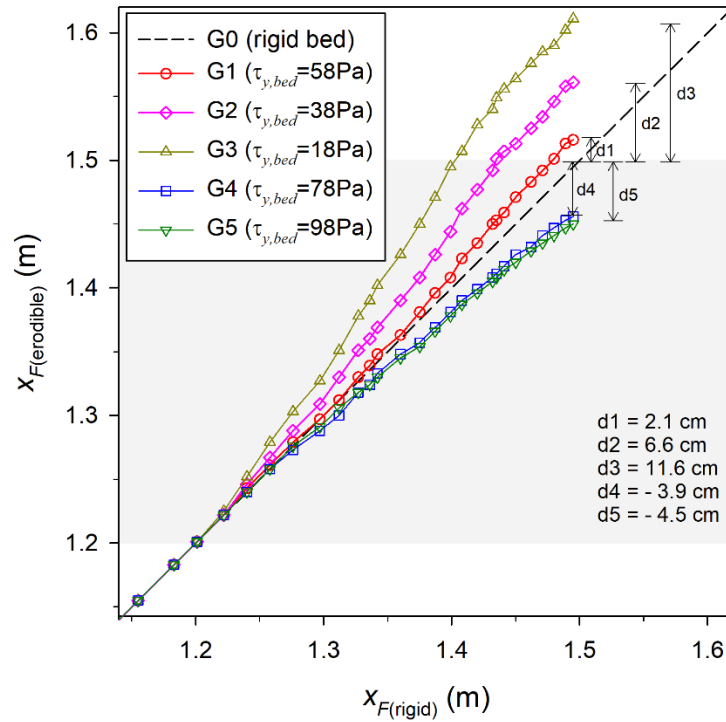
Fig. 5.6 Comparison of the flow front position under different simulation conditions (The dashed black reference line corresponds to flows over a rigid bed. The grey area indicates the erodible bed 300 mm long and 6 mm deep.)

Fig. 5.7 compares the average velocity evolution curves of the flow and the bed in G0, G1, G2 and G4. For each case, the curve will stop when the flow front reaches the end of the erodible bed. It is worth noting that when t=15 s, the flow front of G4 has not yet reached the end of the erodible bed. The average velocity curve of the bed in G0 is horizontal during the interaction, indicating that the bed is rigid in G0. The average velocity of the erodible bed (G1, G2 and G4) significantly increases starting from around t=4.5 s, corresponding to the time when the flow begins interacting with the erodible bed. As shown in Fig. 5.7, the average velocity of the flow (solid lines) is decreasing while that of the bed (dotted lines) is increasing, demonstrating that the kinetic energy is transferred from the flow to the bed during the interaction. As the yield strength of the bed decreases, the kinetic energy transferred from the flow to the bed increases significantly.

Fig. 5.7 Average velocity evolution of the flow and the bed in the different simulation groups (The curve stops when the flow front reaches the end of the erodible bed.)

The main direction of the mixing flow is along the x direction. Therefore, the horizontal velocity field (v_x) of the flow and the bed in G0, G1, G2 and G4 are presented in Fig. 5.8. The simulation results at three special times (t = 6 s, 8.4 s, 14 s) are presented. These times corre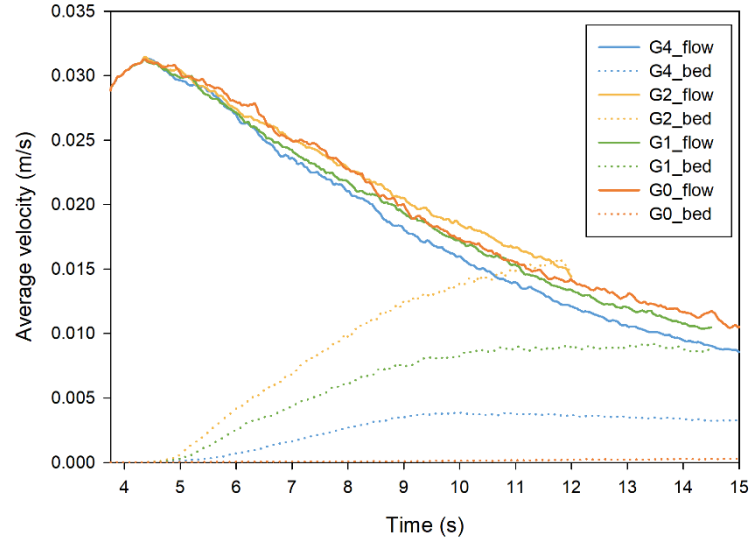spond to three stages of the interaction: early (6 s), middle (8.4 s) and late (14 s) stage, For the rigid bed case, the flow velocity increases slightly during downstream motion and the horizontal flow-bed interface demonstrates that the bed of G0 is effectively rigid and immobile. In the early interaction stage, the flow of G1 and G2 entrained a small portion of the bed material, causing a bulge composed of bed material to form in front of the flow. In the middle and late stages of the interaction, the bulge becomes significantly larger due to more bed material entrained by the flow (Fig. 5.8b and c). It can be seen from Fig. 5.8d that the flow-bed interface is approximately parallel to the bottom of the bed at t=6 s. When t=8.4 s, the front of the flow-bed interface tilts upward slightly, and a similar flow-bed interface also appears at t=14s, which indicates that the entrainment is relatively difficult under this bed condition. In addition, the simulated results illustrate that the mixing flow will travel faster and further if the yield strength of the erodible bed is very low (Fig. 5.8c), which indicates the entrainment increases mobility. In contrast, the motion of the mixing flow will be restricted when it travels over an erodible bed with higher yield strength. Therefore, the strength of the bed material is a very important factor in controlling the mobility of the flow.
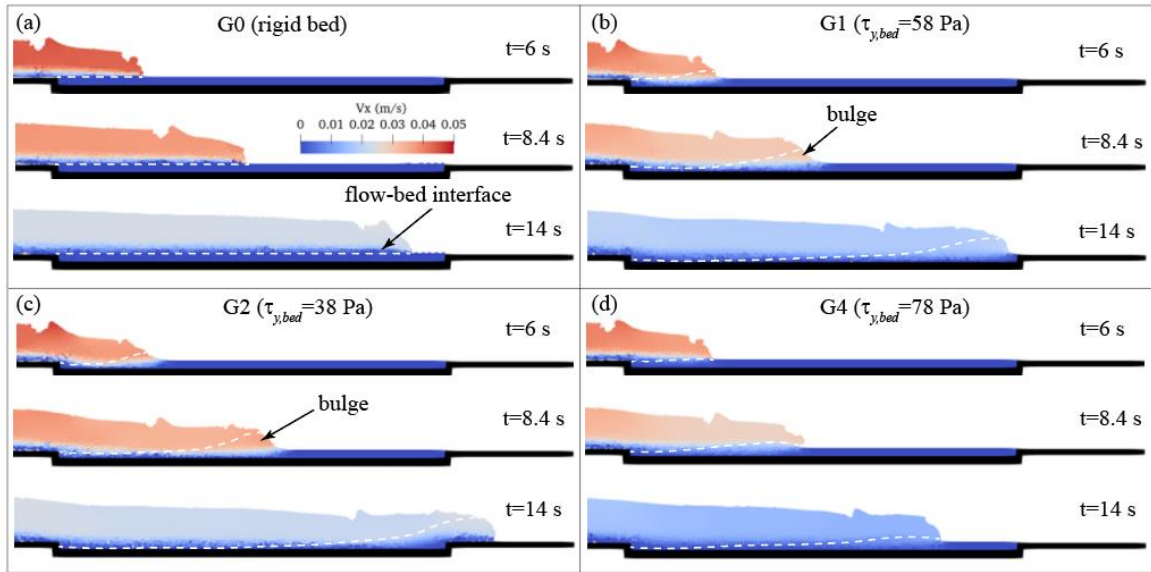
Fig. 5.8 Interaction process of the flow and the bed under different bed conditions (The dashed white line indicates the interface between the flow and the bed.)

5.4 Simulation of the Ximiaodian landslide

Different from the viscous flow mentioned above, the friction parameter is non-negligible in the simulation of loess landslides. In this section, the SPH model considering the friction of material is adopted to analyze the interaction between the loess deposits and the terrace sediments.

5.4.1 Overview of the Ximiaodian landslide

The study area, the South Jingyang Loess Tableland, is located on the right bank of the Jing River in Jingyang County, Shaanxi Province, China (Fig. 5.9a). In this region, the topography is relatively flat, and the elevation ranges from 420 m to 490 m with the slope angles varying between 40° and 85°. The groundwater level increased due to long-term irrigation activities conducted by residents, and this made the slopes prone to slide. More than 50 landslides have been reported in the study area since 1979, causing 29 casualties and destroying approximately 1.4×10^6 m^2 of farmland (Duan et al., 2021; Hu et al., 2022).

The Ximiaodian landslide (E 108° 45′ 42.81″, N 34° 30′ 9.65″) occurred in July 2015 and is a typical flow-like loess landslide. The panorama view of the Ximiaodian landslide is shown in Fig. 5.9b. It can be seen from the post-failure topography that the loess deposits pushed the terrace forward around 100 m, resulting in some transverse ridges formed on the disturbed terrace zone in the arc-shaped arrangement (Fig. 5.9b). Moreover, the interface between the loess deposits and the terrace is easy to distinguish in the field (Fig. 5.9c). As illustrated in Fig. 5.99d, the pre-failure slope is composed of Quaternary loess (Q1-Q3). It is 63 m high, with an average slope angle of 48°. The original terraces are nearly horizontal, with an average thickness of 4 m. Due to the influence of agricultural irrigation on the tableland, the slope became unstable and began to fail. The loess slid along the failure surface and collided with the terrace. The terraces adjacent to the loess deposits were squeezed, generating an upheaved surface that was average 3.8 m higher than the top of the original terraces, while the terraces far away from the loess deposits remained at the original ground level (Fig. 5.9c).
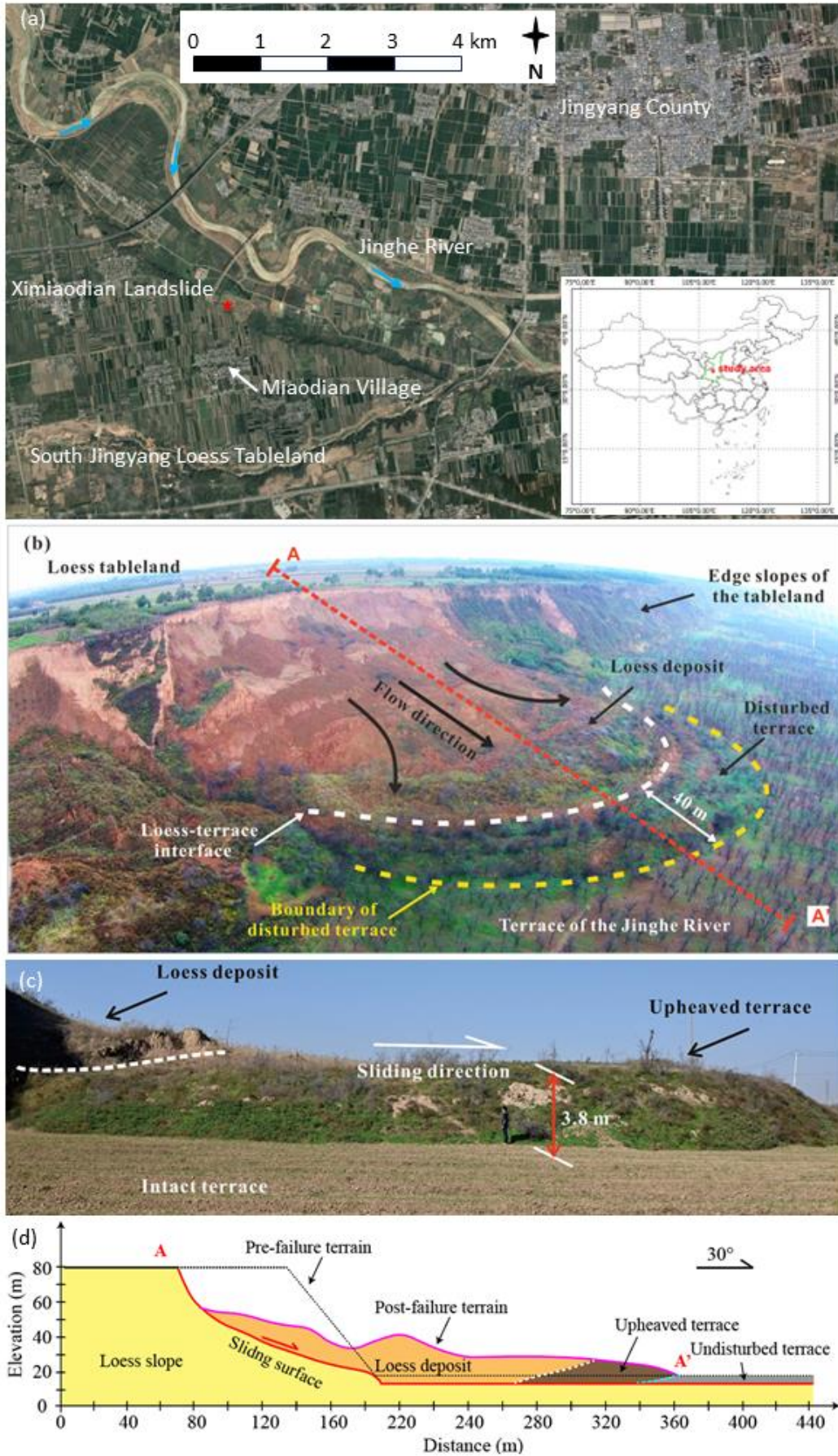
Fig. 5.9 Overview of the Ximiaodian landslide: (**a**) Location and (**b**) Panorama view of the Ximiaodian landslide.

(**c**) Side-view of the upheaved terrace. (**d**) Stratigraphic profile of the Ximiaodian Landslide along the cross-section A-A'.

5.4.2 Run-out process with and without entrainment

To investigate the influence of entrainment on the mobility of the loess landslide, two 2D numerical models as shown in Fig. 5.10 are proposed based on the strata distribution of Ximiaodian landslide (Fig. 5.9d). The loess slopes of the two SPH models are represented by 13184 fluid particles. In a scenario of considering the entrainment (Fig. 5.10a), the terrace is erodible and consists of four colored fluid particles to facilitate observation of the deformation characteristics of the platform during interaction. The terrace sediment in the non-entrainment scenario (Fig. 5.10b) is composed of 4089 fluid particles and has a high yield strength, ensuring that it remains immobile during contact with the loess. Due to the difference in the terrace adopted in the two scenarios, the sliding surface of the second half is different in the two models. The sliding surface in the simulations that accounted for entrainment is located at a depth of 4 m from the top of the terrace, whereas the sliding surface in the simulations without entrainment is located at the top of the terrace.

Fig. 5.10 2D SPH model of Ximiaodian landslide with (**a**) and without (**b**) entrainment consideration

The parameters adopted in the simulations are listed in Table 5.2. The cohesion and density values of loess and terraces were selected based on previous studies in this study area (Duan et al., 2021;

Shen et al., 2019a). In comparison with the simulation considering entrainment, a larger strength value was set to the ri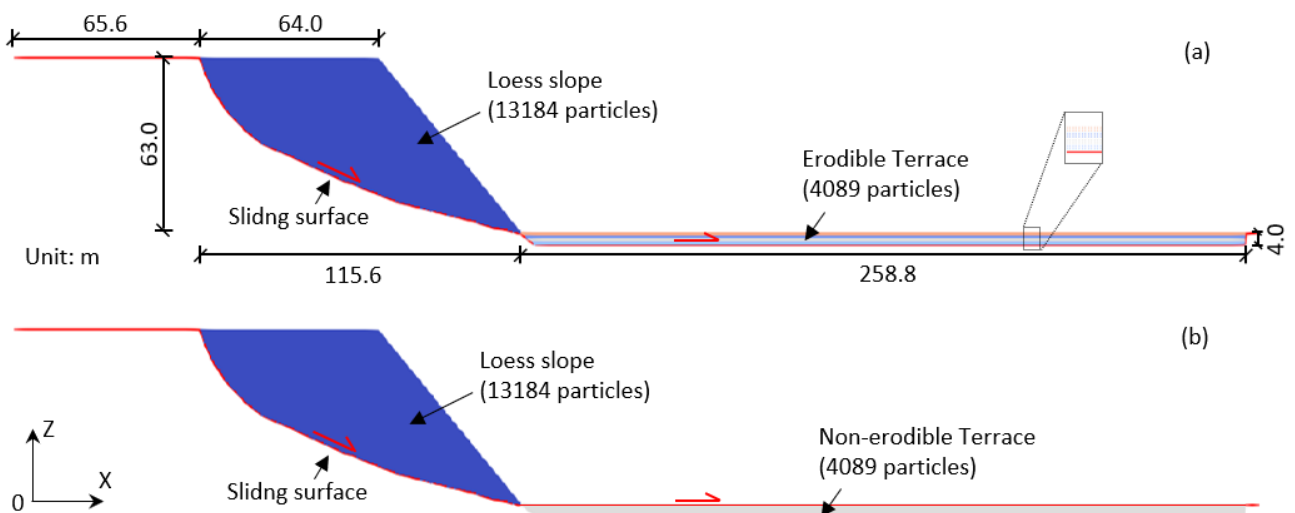gid terrace in the simulation without entrainment. For simplification, the HBP coefficients of the loess and terrace were configured with the same values. In our simulation, we use m=100 and n=1 to simulate the non-Newtonian flow. The internal friction angles φ for both the loess and terrace material (mainly consisting of sandy soils) were lower than the effective internal friction angles suggested by Shen et al., 2019a due to soil liquefaction that may occur during entrainment.

Table 5.2 The parameters used in the simulations of Ximiaodain landslide

Simulation conditions	Materials	Internal friction angle φ (°)	Cohesion c (kPa)	Density ρ (kg/m³)	HBP model coefficient m	HBP model coefficient n
With entrainment	Loess	13.6	15	1800		
	Terrace	11.2	5	2000		
Without entrainment	Loess	13.6	15	1800	100	1
	Terrace	0	1000	2000		

Fig. 5.11 illustrates the interaction between the loess and the terrace during the run-out process. According to the simulation results, the interaction process of the loess deposits and the terrace sediments can be summarized as three stages: 1) colliding stage, 2) shearing stage and 3) traveling stage. At t=2.5 s, the loess at the slope toe collapsed and collided with the nearby terrace sediments, causing the terraces to bend and form a typical geological structure: fold strata as shown in Fig. 5.11a. Under the continuous pushing of the overlying loess, the nearby terrace sediments were sheared upwards and formed a dam-shaped bulge (Fig. 5.11b). This bulge moved forward driven by the loess deposits. Then, a typical "sandwich" structure began to appear in the terrace strata (Fig. 5.11c). Subsequently, the landslide traveled along the sliding surface with a deformation structure similar to Fig. 5.11c until the internal deformation of the landslide becomes stable.

Moreover, three different zones (compressed zone, upheaved zone and undisturbed zone) in the terrace are distinguished as shown in Fig. 5.11 and 5.11e. In the compressed zone, the terrace

sediments are significantly compressed by the overlying loess deposits. As the compression becomes more intense, part of the terrace will be squeezed out. In this case, the maximum upheaved height is 4.2 m from the original terrace surface. During this stage, the terrace strata are generally reversed, creating a "sandwich" structure. In the undisturbed zone, the impact of the loess deposits on the terrace is negligible, causing the terrace to remain on the original surface.
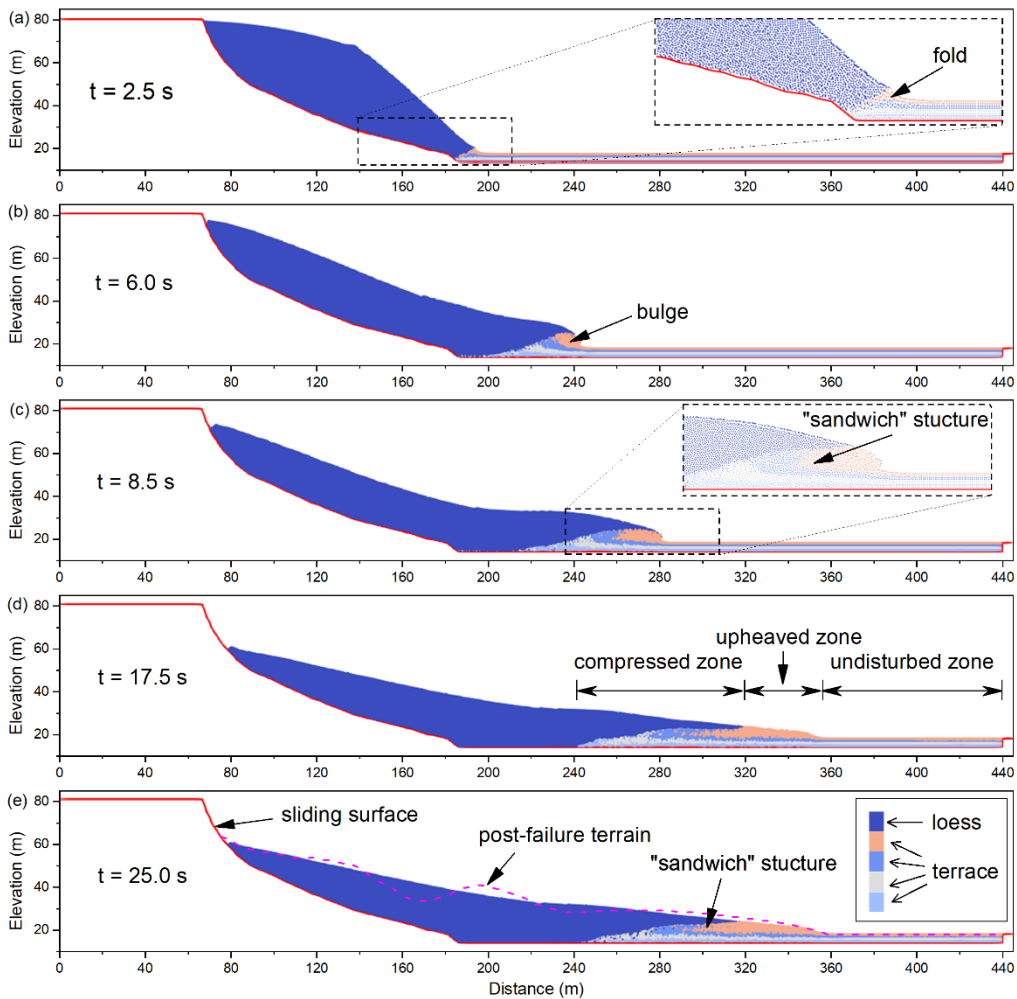
Fig. 5.11 Interaction processes of the loess deposit and the entrained terrace

Fig. 5.12 shows the simulation results without entrainment. The loess deposits propagate along the terrace surface (sliding surface). The terrace sediments are undisturbed during the propagation process, demonstrating the terrace is effectively rigid and immobile. In comparison with the surface obtained by the simulation with entrainment, the run-out distance is significantly underestimated in the simulation without entrainment. As a result, the entrainment is a crucial process in the

simulation of flow-like loess landslides.
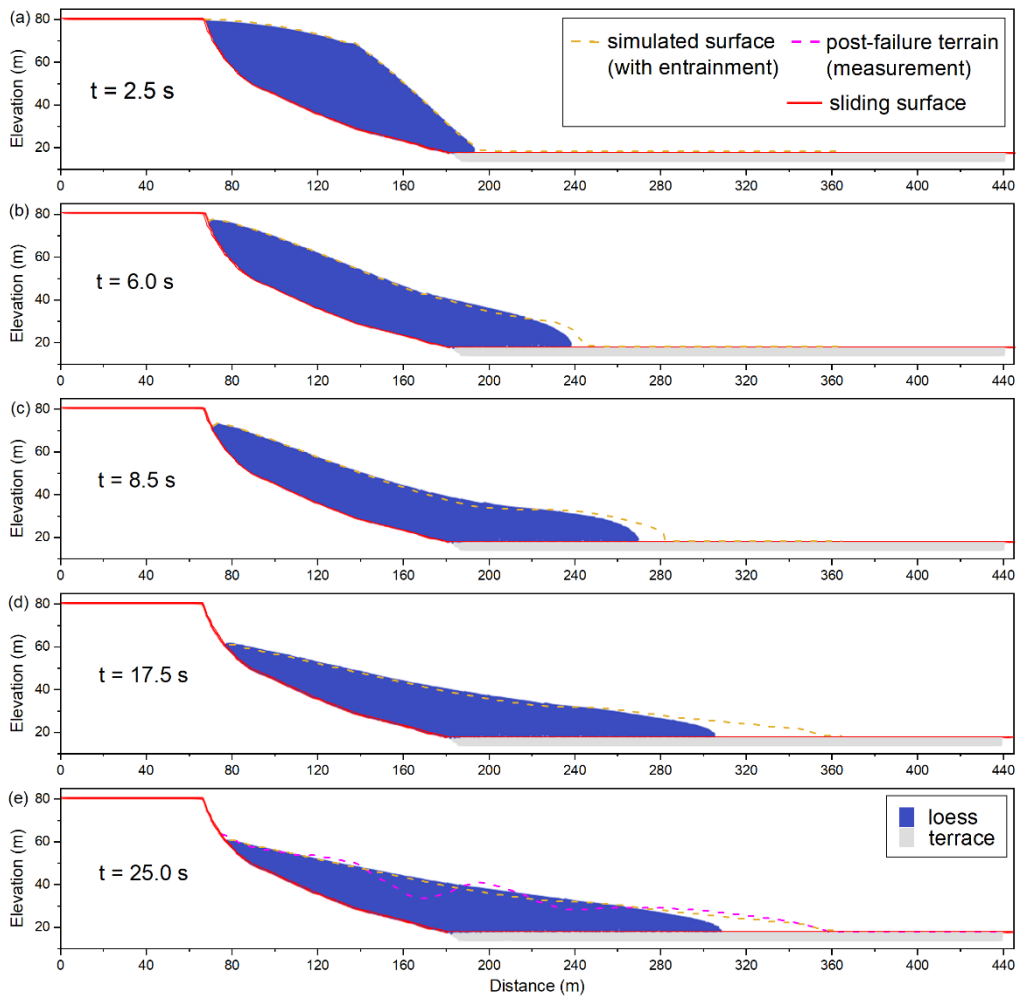
Fig. 5.12 Interaction processes of the loess deposit and the non-entrained terrace

5.4.3 Motion and Deformation analysis

Fig. 5.13 compares the average velocities of the loess deposits and the terrace sediments for the two simulation scenarios. Regardless of the simulation scenario, the horizontal velocity of the material is always greater than the vertical velocity, demonstrating the horizontal direction is the main sliding direction. For the simulation with entrainment, the peak of the loess is lower than that of the terrace, and the peak arrival time of the terrace is later than that of the loess. It indicates that the kinetic energy transfers from the loess deposits to the terrace sediments. Additionally, the simulated results show that entrainment increases the mobility of the loess landslide, potentially leading to

more severe consequences.
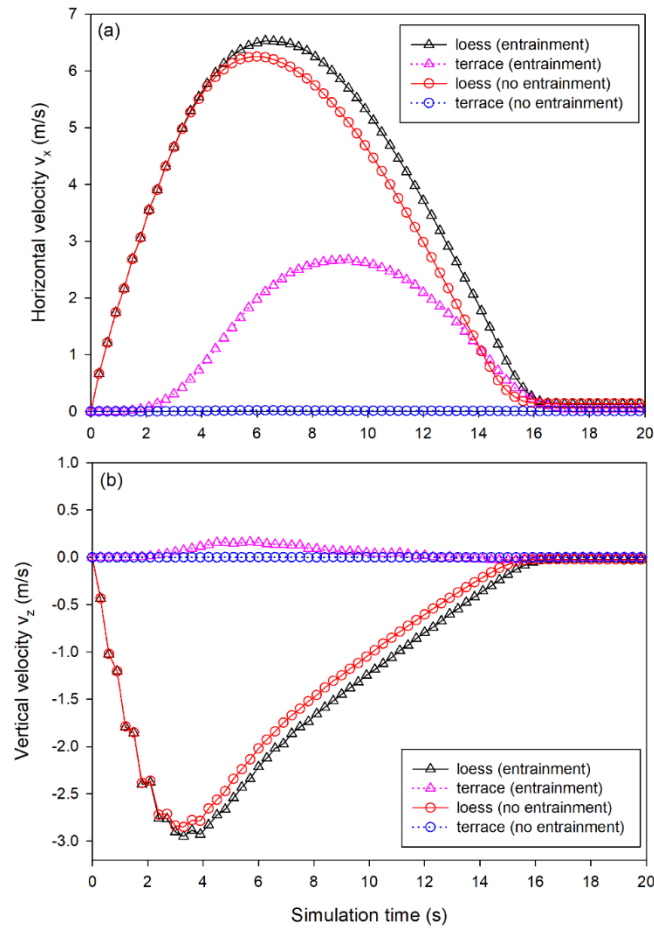
Fig. 5.13 Average (a) horizontal and (b) vertical velocity evolution of the loess deposits and the terrace sediments with and without entrainment

Twenty-two monitoring particles are set during the simulation to study the deformation characteristics of the loess landslide. As shown in Fig. 5.14a, 10 monitoring particles are selected in the loess slope. Among them, 3 monitoring particles (P1-P3) near the sliding surface, 3 monitoring particles (P4-P6) located at the middle of the slope, and 4 monitoring particles (P7-P10) close to the slope surface. Three groups of monitoring particles are also selected in the disturbed terrace. They are located at the rear (P11-P14), middle (P15-P18) and front (P19-P22) of the disturbed terrace.

Fig. 5.14b and Fig. 5.14c show the motion trajectories of these monitoring particles in simulations with and without entrainment, respectively. For simulation considering entrainment, the terrace has a large horizontal displacement due to the push of the loess. As the loess deposits continue to move

forward in their sliding direction, the vertical displacement of the terrace sediments becomes larger. In addition, the horizontal and vertical displacements are more significant near the terrace surface, and the monitoring particles located at the rear part of the terraces (P11-P14) appear to attain larger displacements, indicating that the terraces close to the loess deposits are more susceptible to disturbance. The motion trajectories of monitoring particles in loess slopes vary at the different locations. Monitoring particles near the sliding surface (P1-P3) move along the sliding surface, so the motion trajectories of these particles are parallel to the sliding surface. Other particles in the slope (P4-P10) reveal a roto-translational motion trajectory. However, the motion trajectories of P9 and P10 are slightly convex in the translation segment due to the vertical displacement. For non-entrainment simulation, the monitoring particles in the terrace sediments are almost immobile. The motions of P1-P8 in the non-entrainment simulation are similar to those in the simulation considering entrainment, but the particles located at the slope toe (P9 and P10) present obvious downward vertical displacement in the second half.

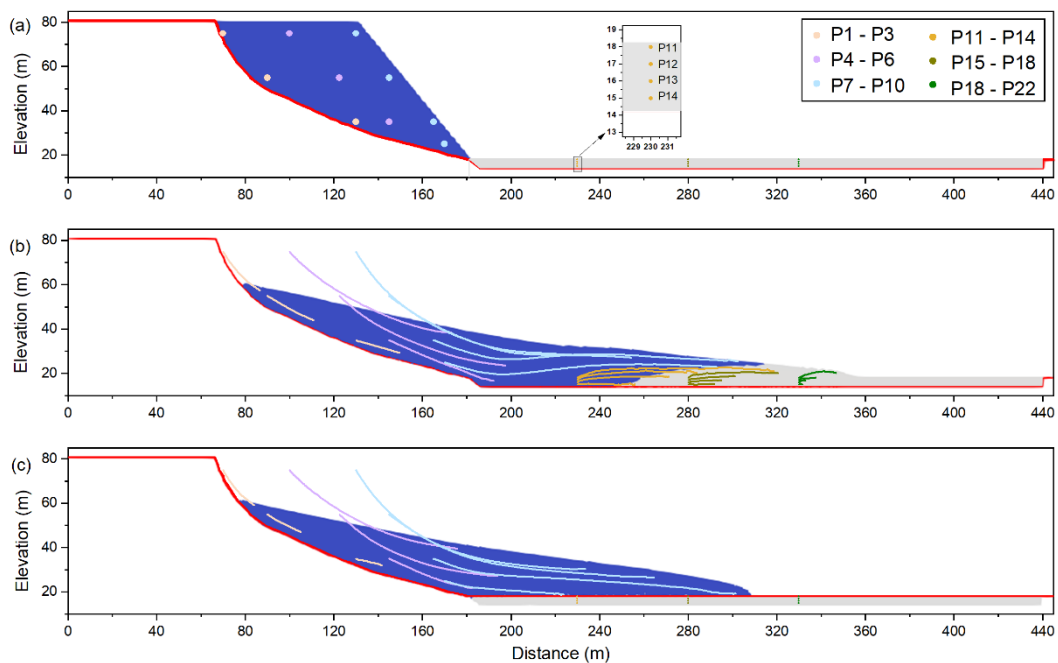**Fig. 5.14 (a)** Distribution of 22 monitoring particles in the loess slope (P1-P10) and the terrace sediments (P11-P22). **(b)** Motion trajectories of these monitoring particles in the simulation with entrainment and **(c)** without entrainment

5.4.4 Influence of internal friction angle on entrainment

Internal friction angle is a key parameter that controls the mechanical behavior of materials. Another 4 simulation groups with different friction parameters were carried out to investigate how the internal friction angle affects the entrainment mechanism of flow-like landslides. Fig. 5.15 illustrates the final deposit morphologies under different friction conditions. The interface between the loess and the terrace tends to be steeper and shorter when the friction coefficient of the loess is larger than that of the terrace (Fig. 5.15a, c and d). On the contrary, the interface will be gentler and longer if the friction coefficient of the loess is lower than that of the terrace, as shown in Fig. 5.15b and Fig. 5.15e. Comparison of Fig. 5.15a, d and e indicates that entrainment becomes more difficult as the internal friction angle of the terrace increases. The interface of the loess and the terrace becomes longer and flatter. On the other hand, it is more difficult for the terrace to be entrained by the loess if the internal friction angle of the loess increases. In this case, the interface of the loess and the terrace is shorter and steeper (Fig. 5.15a b and c). The simulation results show that increasing the friction coefficient of loess or terraces will reduce the runout distance. The difference is that the upheaved zone obtained by increasing the loess friction parameter is larger than that obtained by increasing the terrace friction parameter (Fig. 5.15c and e). Additionally, the simulation results of Fig. 5.15a agree best with the measured post-failure topography, and the simulated fluctuant morphology of the disturbed terrace is also observed in the field (Fig. 5.9b).
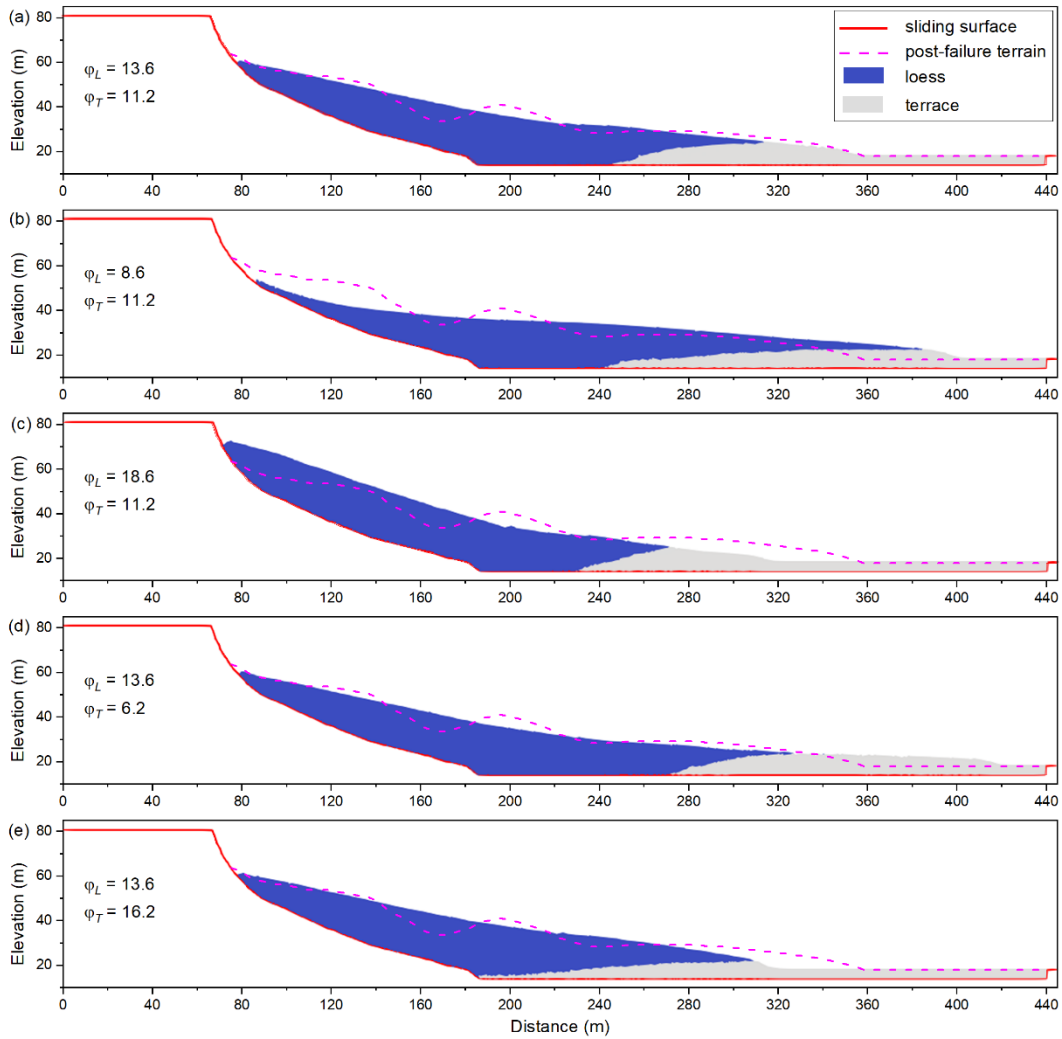
Fig. 5.15 Influence of internal friction angle on the interaction between the loess deposits and the terrace sediments

The front positions of the loess and the terrace are well-reported during the simulations. All curves show the same evolution patterns: concave limb, convex limb and flat limb. As shown in Fig. 5.16a, when the friction parameter of the loess increases, the front position of the loess and the terrace decreases, and the loess front always lags behind the terrace front. Similar conclusions are obtained from Fig. 5.16b. Additionally, as the friction parameter of the loess rises, the distance between the loess front and the terrace front expands. Conversely, this distance shrinks when the friction parameter of the terrace is increased.
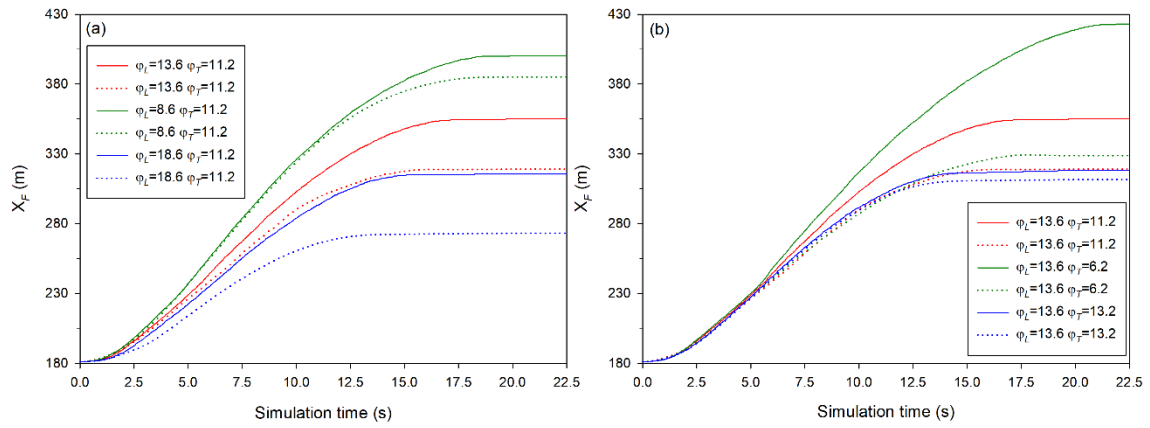
Fig. 5.16 Evolution of the loess deposit front (dotted lines) and terrace sediment (solid lines) front under different friction conditions

Fig. 5.17 shows the kinetic energy evolution of the loess and the terrace in the simulations. It can be seen from Fig. 5.17a that the variation of the loess is larger than that of the terrace. The opposite results are obtained from Fig. 5.17b. The peak arrival time of the terrace in all simulations is later than that of the loess, demonstrating the kinetic energy transformation from the loess to the terrace.
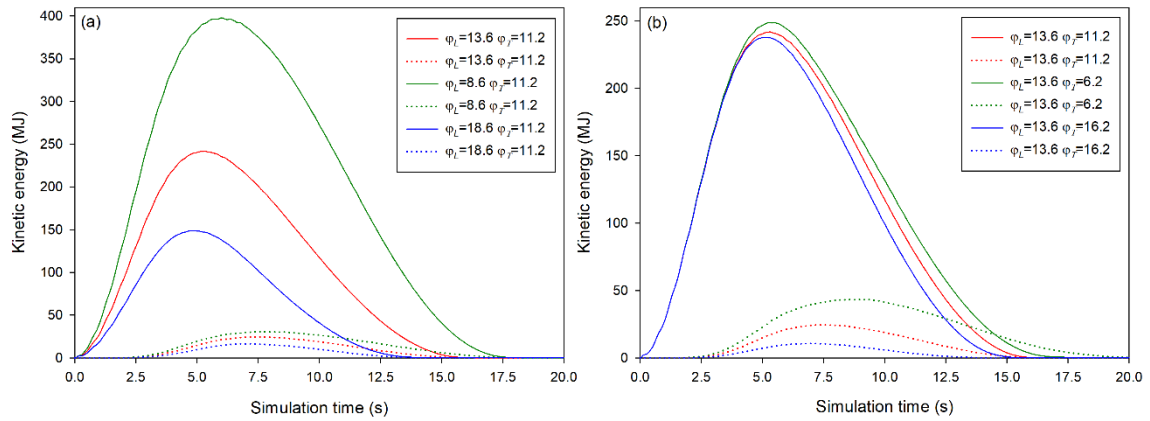
Fig. 5.17 Kinetic energy evolution curves of loess deposits (solid lines) and terrace sediments (dotted lines) under different friction conditions

5.5 Conclusive remarks

In this study, two different flows (the viscoplastic flow and the frictional flow) are simulated adopting the original and the improved SPH models. The complex entrainment phenomena are explained from the perspective of numerical simulation. In addition, we discuss the effect of

entrainment on flow mobility. Some of the main conclusions are summarized below:

(1) The entrainment process of a viscoplastic flow is reproduced using the SPH model incorporating the HBP rheology law. The simulation results are validated by the experimental data provided by Bates and Ancey, 2017. The simulated flow-bed interface shows a satisfactory agreement with the experimental results. Furthermore, we analyze the effects of the bed shear strength on the flow mobility. The bed becomes more susceptible to being entrained by the incoming flow as the shear strength of the bed decreases.

(2) Simulation of a real loess landslide occurred on Jingyang loess plateau showed that the SPH modelling is able to reproduce the observed behavior in the field. Comparison of simulations with and without entrainment indicates the entrainment is a non-negligible process in accurately predicting runout distance. Further, the SPH model can capture the "sandwich" structure and the ground upheaval in the disturbed terrace that observed in the field.

(3) The internal friction angle of the materials has a dominant influence on the entrainment and the run-out distance of the flow-like loess landslide. As the internal friction angle of the loess and the terrace increases, the terrace sediment is more difficult to be entrained by the loess, and the run-out distance of the landslide is farther. Two different loess-terrace interfaces can be obtained by increasing the friction parameter of the loess and the terrace. Specifically, increasing the friction parameter of the loess will result in a short-steep interface and a wide upheaval zone, whereas increasing the friction parameter of the terrace will obtain a long-flat interface and a narrow upheaval zone.

6. Conclusions and future works

In this thesis, I have investigated three key aspects of flow-like landslides (slope initial failure, landslide-structure interaction (FSI) and bed entrainment) using improved SPH models based on the open access code: DualSPHysics. According to the simulation results, the following questions are answered.

Q1: Can we deepen our knowledge of complex slope failure mechanisms using SPH models? Will the slope failure mechanisms differ depending on their distinct characteristics and geological conditions?

To answer these two questions, an improved SPH model with strain softening elastic-plastic constitutive law was developed to study the failure modes of different slopes. The shear band development on a cohesive soil slope was captured using the SPH model without considering strain softening, and the simulated failure surface was in line with Bishop's circle obtained by the limit equilibrium method. The improved SPH model with strain softening then well reproduced the retrogressive failure pattern and post-failure behavior commonly observed in a sensitive clay slope. This type of failure mode is characterized by the backward movement of the failure surface. Finally, the improved model was applied to the failure of the Caijiapo landslide. The simulated topography of the landslide deposit and the sliding surfaces agreed generally well with the field measurements. The primary slip surface generated along the pre-existing structural plane at the back scarp the landslide, and the other two secondary slip surfaces were triggered after the formation of the primary slip surface, dividing the landslide into four blocks.

The above simulation results showed that the failure modes of the three slopes are different. For a cohesive soil slope without strain-softening, only one arc-shaped shear surface was generated during the entire failure process. However, multiple failure surfaces were formed in the failure process of a clay slope and a loess slope due to the strain-softening properties of slope soils. The

failure of clay slopes followed the typical retrogressive failure patterns: the landslide or mass movement retrogresses or moves backward into the slope, usually against the direction of the slope's natural inclination. However, the failure of the loess slope in our case consisted of typical primary and secondary sliding because of the existing of the structural plane. Secondary slip surfaces were developed within the sliding mass after the primary sliding.

Q2: How to correctly predict the impact force of fast flowing front on protective structures? Are the interaction mechanisms between different types of protective structures and debris flows different?

The impact force exerted by landslides on the structures can be predicted utilizing various methods such as field monitoring, laboratory experiments and numerical modelling. The accuracy of impact forces plays a dominant role in deciding the effect mitigation strategies. With the dual considerations of cost and accuracy, Numerical modelling method is selected to estimate the interactions between landslides and structures. An advanced SPH model coupled with a modified HBP law that accounts for friction dissipations was proposed to improve the capability of the SPH models in handling landslide-structure interaction (FSI) problems. The improved model was verified through two benchmarks. It demonstrated that the improved model can effectively analyze FSI issues. Simulation results of case study indicated that the check dams can dramatically diminish the discharge and the frontal flow velocity of the debris flow, and the peak impact force of debris flow generally decreases with gentler channel slope.

Furthermore, different types of structures were tested along the flow path to investigate the influence of structure shape on the movement of landslides. Simulation results stated that different structures show different mechanisms during interaction. The mitigation effect of a flat deposition areas, for example, is mainly manifested by reducing the flow front velocity. Thus, this type of mitigation structure is usually installed in the upper part of the channel. Check dams mainly contribute to diminishing downstream discharges. Retention basins are often built at the outlet of the channel to facilitate landslide deposition. In practical applications, optimized mitigation

decisions can be made by combining terrain characteristics and mechanisms of various structures, and the performance of these combined structures can be properly analyzed using the proposed approach.

Q3: What is the entrainment mechanism of loess landslide? How does the friction coefficient affect the entrainment pattern?

To address this question, I improved the SPH model considering friction dissipations along the bed. This model was used to simulate the Ximiaodian landslide. The loess and the terrace were simply represented by two different single-phase materials. Results showed that the post-topography obtained by the field survey can be satisfactorily fitted by considering entrainment in the model. Neglecting the effects of entrainment, the run-out distance was dramatically underestimated. The entrainment process of the Ximiaodian landslide can be roughly divided into three stages: 1) colliding stage, 2) shearing stage and 3) traveling stage. Two main entrainment mechanisms (colliding and shearing) are involved during this process. In the early stage of interaction between loess and terraces, colliding is a main mechanism. The terraces were pushed forward because of the collision of the loess. In the middle and last stages, the shear failure occurring in the terraces plays a dominant role in terrace deformation. Meanwhile, three distinguished zones (compressed zone, upheaved zone and undisturbed zone) are formed within the terraces accompanied by entrainment.

The internal friction angle is resulted to be an important coefficient in the dynamic analysis of loess landslides. When the internal friction angle of the material increases, whether it is loess or terraces, entrainment becomes more difficult. Moreover, we obtained two totally different loess-terrace interfaces when increasing the friction coefficient of the loess or the terrace: a shorter and steeper interface was observed in the simulation with a higher loess friction coefficient, while a longer and flatter interface was predicted in the simulation with a higher terrace friction coefficient.

Although the improved models extended the application of DualSPHysics to address some

significant phenomena associated with flow-like landslides, there are still certain limitations when studying issues such as particle inverse grading involved in debris flows, the dewatering effects of debris flows and rock fragmentations. It is necessary to develop two-phase numerical models to analyze these solid-fluid interaction issues. In the future, I plan to develop a two-phase SPH model, where the solid phase consists of solid particles of different sizes, and the fluid phase is either water or a mixture of water with very fine soil particles to improve the simulation performance of flow-like landslides.

Notations

The following conventions are used in this thesis:

(1) Greek indices denote coordinates.

(2) Latin indices denote particles.

(3) Vectors will be written in Bold.

(4) The Einstein summation rule is used.

The main symbols used in this thesis are as follows:

Symbol	Description
m	Mass
ρ	Density
V	Volume
Ω	Support domain
$\boldsymbol{r}$	Position vector
h	Smoothing length
dp	Particle spacing
W	Interpolating kernel function
W_{ij}	$W(\boldsymbol{r}_i - \boldsymbol{r}_j, h)$
$\boldsymbol{r}_{ij}$	$\boldsymbol{r}_i - \boldsymbol{r}_j$
r	Distance of particle i and j, $\|\boldsymbol{r}_{ij}\|$
δ	Dirac distribution
q	A non-dimensional distance between particles, $q = r/h$
α_D	Coefficient of kernel function
$\boldsymbol{v}$	Velocity vector
$\boldsymbol{g}$	Gravity acceleration
P	Pressure
$\boldsymbol{\tau}$	Viscous stress tensor
∇	Differential operator
$\dfrac{d}{dt}$	Total derivative operator (with respect to t)
$\langle \cdot \rangle$	Approximation
Δt	Time step

N	Total number of particles
C_s	Speed of sound
ρ_0	Reference density
γ	A dimensionless constant of EoS equation $\gamma = 7$
D	Density diffusion term
Γ	Momentum dissipation term
ψ_{ij}	Neumann–Richtmeyer artificial dissipation
Π_{ij}	Artificial viscosity
v_0	Kinetic viscosity
$\boldsymbol{\sigma}$	Cauchy stress tensor
p	Isotropic hydrostatic pressure
$\boldsymbol{s}$	Deviatoric shear stress tensor
$\dot{\boldsymbol{\sigma}}$	Stress rate tensor
$\dot{\boldsymbol{\varepsilon}}$	Strain rate tensor
$\dot{\boldsymbol{\omega}}$	Spin rate tensor
G	Shear modulus
K	Elastic bulk modulus
E	Young's modulus
ν	Poisson's ratio
$\dot{\lambda}$	The rate of plastic multiplier λ
f	Plastic yield function
g	Plastic potential function
I_1	The first invariant of the stress
J_2	The second invariant of the deviatoric stress
φ	Internal friction angle
c	Cohesion
α_φ	Coefficient of the Drucker-Prager yielding criterion
k_c	Coefficient of the Drucker-Prager yielding criterion
ψ	Dilatancy angle
$\bar{\varepsilon}^p$	The equivalent plastic strain
$\dot{\boldsymbol{e}}_p$	The deviatoric plastic strain rate tensor
$\dot{\boldsymbol{\gamma}}$	The shear strain rate tensor
$|\dot{\boldsymbol{\gamma}}|$	The magnitude of the shear strain rate tensor
μ	Dynamic viscosity
τ_y	Yield shear stress
μ_{eff}	Effective coefficient of the HBP law
P_+	Positive pressures $P_+ = max\{0, P\}$

References

Abdelrazek, A.M., Kimura, I., Shimizu, Y., 2016. Simulation of three-dimensional rapid free-surface granular flow past different types of obstructions using the SPH method. Journal of Glaciology 62, 335–347. https://doi.org/10.1017/jog.2016.22

Altomare, C., Tafuni, A., Domínguez, J.M., Crespo, A.J.C., Gironella, X., Sospedra, J., 2020. SPH simulations of real sea waves impacting a large-scale structure. J Mar Sci Eng 8, 1–21. https://doi.org/10.3390/jmse8100826

Armanini, A., Rossi, G., Larcher, M., 2019. Dynamic impact of a water and sediments surge against a rigid wall. Journal of Hydraulic Research 58, 314–325. https://doi.org/10.1080/00221686.2019.1579113

Armento, M.C., Genevois, R., Tecca, P.R., 2008. Comparison of numerical models of two debris flows in the Cortina d' Ampezzo area, Dolomites, Italy. Landslides 5, 143–150. https://doi.org/10.1007/s10346-007-0111-2

Baggio, T., Mergili, M., D'Agostino, V., 2021. Advances in the simulation of debris flow erosion: The case study of the Rio Gere (Italy) event of the 4th August 2017. Geomorphology 381, 107664. https://doi.org/10.1016/j.geomorph.2021.107664

Bates, B.M., Ancey, C., 2017. The dam-break problem for eroding viscoplastic fluids. J Nonnewton Fluid Mech 243, 64–78. https://doi.org/10.1016/j.jnnfm.2017.01.009

Bates, B.M., Andreini, N., Ancey, C., 2016. Basal entrainment by Newtonian gravity-driven flows. Physics of Fluids 28. https://doi.org/10.1063/1.4947242

Bentley, M.J., Foster, J.M., Potvin, J.J., Bevan, G., Sharp, J., Woeller, D.J., Take, W.A., 2023. Surface displacement expression of progressive failure in a sensitive clay landslide observed with long-term UAV monitoring. Landslides 20, 531–546. https://doi.org/10.1007/s10346-022-01995-4

Berger, C., McArdell, B.W., Schlunegger, F., 2011. Direct measurement of channel erosion by debris flows, Illgraben, Switzerland. J Geophys Res Earth Surf 116, 1–18. https://doi.org/10.1029/2010JF001722

Bernard, M., Barbini, M., Boreggio, M., Biasuzzi, K., Gregoretti, C., 2024. Deposition areas: An effective solution for the reduction of the sediment volume transported by stony debris flows on the high-sloping reach of channels incising fans and debris cones. Earth Surf Process Landf 49, 664–683. https://doi.org/10.1002/esp.5727

Bernard, M., Boreggio, M., Degetto, M., Gregoretti, C., 2019. Model-based approach for design and performance evaluation of works controlling stony debris flows with an application to a case study at Rovina di Cancia (Venetian Dolomites, Northeast Italy). Science of the Total Environment 688, 1373–1388. https://doi.org/10.1016/j.scitotenv.2019.05.468

Bishop, A.W., 1955. The use of the slip circle in the stability analysis of slopes. Géotechnique 7–16.

Blanc, T., Pastor, M., Drempetic, M.S., Drempetic, V., Haddad, B., 2011. Depth integrated modelling of fast landslide propagation. European Journal of Environmental and Civil Engineering 15, 51–72. https://doi.org/10.1080/19648189.2011.9695304

Bui, H.H., Fukagawa, R., Sako, K., Ohno, S., 2008. Lagrangian meshfree particles method (SPH) for large deformation and failure flows of geomaterial using elastic–plastic soil constitutive model. Int J Numer Anal Methods Geomech 32, 1537–1570. https://doi.org/10.1002/nag

Bui, H.H., Fukagawa, R., Sako, K., Wells, J.C., 2011. Slope stability analysis and discontinuous slope failure simulation by elasto-plastic smoothed particle hydrodynamics (SPH). Géotechnique 61, 565–574. https://doi.org/10.1680/geot.9.P.046

Bui, H.H., Nguyen, G.D., 2021. Smoothed particle hydrodynamics (SPH) and its applications in geomechanics: From solid fracture to granular behaviour and multiphase flows in porous media. Comput Geotech 138, 104315. https://doi.org/10.1016/j.compgeo.2021.104315

Calvetti, F., di Prisco, C.G., Vairaktaris, E., 2017. DEM assessment of impact forces of dry granular masses on rigid barriers. Acta Geotech 12, 129–144. https://doi.org/10.1007/s11440-016-0434-z

Chen, H.X., Li, J., Feng, S.J., Gao, H.Y., Zhang, D.M., 2019. Simulation of interactions between debris flow and check dams on three-dimensional terrain. Eng Geol 251, 48–62. https://doi.org/10.1016/j.enggeo.2019.02.001

Chen, W., Qiu, T., 2012. Numerical Simulations for Large Deformation of Granular Materials Using Smoothed Particle Hydrodynamics Method. International Journal of Geomechanics 12, 127–135. https://doi.org/10.1061/(asce)gm.1943-5622.0000149

Chen, Z., Dai, Z., Huang, Y., Bian, G., 2013. Numerical simulation of large deformation in shear panel dampers using smoothed particle hydrodynamics. Eng Struct 48, 245–254. https://doi.org/10.1016/j.engstruct.2012.09.008

Chen, Z., He, S., Shen, W., Wang, D., 2021. Effects of defense-structure system for bridge piers on two-phase debris flow wakes. Acta Geotech. https://doi.org/10.1007/s11440-021-01296-5

Choi, C.E., Nikooei, M., 2023. Revealing the physics of sediment ploughing by geophysical mass flows: Depth-averaged approach. Comput Geotech 154. https://doi.org/10.1016/j.compgeo.2022.105119

Choi, S.K., Lee, J.M., Kwon, T.H., 2018. Effect of slit-type barrier on characteristics of water-dominant debris flows: small-scale physical modeling. Landslides 15, 111–122. https://doi.org/10.1007/s10346-017-0853-4

Crespo, A.J.C., Domínguez, J.M., Rogers, B.D., Gómez-Gesteira, M., Longshaw, S., Canelas, R., Vacondio, R., Barreiro, A., García-Feal, O., 2015. DualSPHysics: Open-source parallel CFD solver based on Smoothed Particle Hydrodynamics (SPH). Comput Phys Commun 187, 204–216. https://doi.org/10.1016/j.cpc.2014.10.004

Crespo, A.J.C., Gómez-Gesteira, M., Dalrymple, R.A., 2007. Boundary conditions generated by

dynamic particles in SPH methods. Computers, Materials and Continua 5, 173–184.

Crosta, G.B., De Blasio, F. V., De Caro, M., Volpi, G., Imposimato, S., Roddeman, D., 2017. Modes of propagation and deposition of granular flows onto an erodible substrate: experimental, analytical, and numerical study. Landslides 14, 47–68. https://doi.org/10.1007/s10346-016-0697-3

Cui, P., Zeng, C., Lei, Y., 2015. Experimental analysis on the impact force of viscous debris flow. Earth Surf Process Landf 40, 1644–1655. https://doi.org/10.1002/esp.3744

Cuomo, S., Di Perna, A., Martinelli, M., 2022. Analytical and numerical models of debris flow impact. Eng Geol 308, 106818. https://doi.org/10.1016/j.enggeo.2022.106818

Cuomo, S., Di Perna, A., Martinelli, M., 2021. Material point method (Mpm) hydro-mechanical modelling of flows impacting rigid walls. Canadian Geotechnical Journal 58, 1730–1743. https://doi.org/10.1139/cgj-2020-0344

Dai, Z., Huang, Y., Cheng, H., Xu, Q., 2017. SPH model for fluid–structure interaction and its application to debris flow impact estimation. Landslides 14, 917–928. https://doi.org/10.1007/s10346-016-0777-4

Dai, Z., Huang, Y., Cheng, H., Xu, Q., 2014. 3D numerical modeling using smoothed particle hydrodynamics of flow-like landslide propagation triggered by the 2008 Wenchuan earthquake. Eng Geol 180, 21–33. https://doi.org/10.1016/j.enggeo.2014.03.018

Dalrymple, R.A., Rogers, B.D., 2006. Numerical modeling of water waves with the SPH method. Coastal Engineering 53, 141–147. https://doi.org/10.1016/j.coastaleng.2005.10.004

Deb, D., Pramanik, R., 2013. Failure Process of Brittle Rock Using Smoothed Particle Hydrodynamics. J Eng Mech 139, 1551–1565. https://doi.org/10.1061/(asce)em.1943-7889.0000592

Dey, R., Hawlader, B., Phillips, R., Soga, K., 2015. Large deformation finite-element modelling of progressive failure leading to spread in sensitive clay slopes. Geotechnique 65, 657–668. https://doi.org/10.1680/geot.14.P.193

Domínguez, J.M., Fourtakas, G., Altomare, C., Canelas, R.B., Tafuni, A., García-Feal, O., Martínez-Estévez, I., Mokos, A., Vacondio, R., Crespo, A.J.C., Rogers, B.D., Stansby, P.K., Gómez-Gesteira, M., 2021. DualSPHysics: from fluid dynamics to multiphysics problems. Comput Part Mech. https://doi.org/10.1007/s40571-021-00404-2

Duan, Z., Cheng, W.C., Peng, J.B., Rahman, M.M., Tang, H., 2021. Interactions of landslide deposit with terrace sediments: Perspectives from velocity of deposit movement and apparent friction angle. Eng Geol 280. https://doi.org/10.1016/j.enggeo.2020.105913

Egashira, S., Honda, N., Itoh, T., 2001. Experimental study on the entrainment of bed material into debris flow. Physics and Chemistry of the Earth, Part C: Solar, Terrestrial and Planetary Science 26, 645–650. https://doi.org/10.1016/S1464-1917(01)00062-9

English, A., Domínguez, J.M., Vacondio, R., Crespo, A.J.C., Stansby, P.K., Lind, S.J., Chiapponi, L.,

Gómez-Gesteira, M., 2022. Modified dynamic boundary conditions (mDBC) for general-purpose smoothed particle hydrodynamics (SPH): application to tank sloshing, dam break and fish pass problems. Comput Part Mech 9, 1–15. https://doi.org/10.1007/s40571-021-00403-3

Farin, M., Mangeney, A., Roche, O., 2014. Fundamental changes of granular flow dynamics, deposition, and erosion processes at high slope angles: Insights from laboratory experiments. J Geophys Res Earth Surf 119, 504–532. https://doi.org/10.1002/2013JF002750

Faug, T., 2015. Depth-averaged analytic solutions for free-surface granular flows impacting rigid walls down inclines. Phys Rev E Stat Nonlin Soft Matter Phys 92, 1–14. https://doi.org/10.1103/PhysRevE.92.062310

Faug, T., Chanut, B., Naaim, M., Perrin, B., 2008a. Avalanches overflowing a dam: Dead zone, granular bore and run-out shortening. Ann Glaciol 49, 77–82. https://doi.org/10.3189/172756408787814799

Faug, T., Chanut, B., Naaim, M., Perrin, B., 2008b. Avalanches overflowing a dam: Dead zone, granular bore and run-out shortening. Ann Glaciol 49, 77–82. https://doi.org/10.3189/172756408787814799

Fourtakas, G., Dominguez, J.M., Vacondio, R., Rogers, B.D., 2019. Local uniform stencil (LUST) boundary condition for arbitrary 3-D boundaries in parallel smoothed particle hydrodynamics (SPH) models. Comput Fluids 190, 346–361. https://doi.org/10.1016/j.compfluid.2019.06.009

Fourtakas, G., Rogers, B.D., 2016. Modelling multi-phase liquid-sediment scour and resuspension induced by rapid flows using Smoothed Particle Hydrodynamics (SPH) accelerated with a Graphics Processing Unit (GPU). Adv Water Resour 92, 186–199. https://doi.org/10.1016/j.advwatres.2016.04.009

Fraccarollo, L., Capart, H., 2002. Riemann wave description of erosional dam-break flows. J Fluid Mech 461, 183–228. https://doi.org/10.1017/S0022112002008455

Frank, F., McArdell, B.W., Huggel, C., Vieli, A., 2015. The importance of entrainment and bulking on debris flow runout modeling: Examples from the Swiss Alps. Natural Hazards and Earth System Sciences 15, 2569–2583. https://doi.org/10.5194/nhess-15-2569-2015

Frissane, H., Taddei, L., Lebaal, N., Roth, S., 2019. SPH modeling of high velocity impact into ballistic gelatin. Development of an axis-symmetrical formulation. Mechanics of Advanced Materials and Structures 26, 1881–1888. https://doi.org/10.1080/15376494.2018.1452322

Galano, N., Moreno-Casas, P.A., Abell, J.A., 2021. Extending the Particle Finite Element Method for sediment transport simulation. Comput Methods Appl Mech Eng 380, 1–16. https://doi.org/10.1016/j.cma.2021.113772

Gauer, P., Issler, D., 2004. Possible erosion mechanisms in snow avalanches. Ann Glaciol 38, 384–392. https://doi.org/10.3189/172756404781815068

Ghaïtanellis, A., Violeau, D., Ferrand, M., El, K., Abderrezzak, K., Leroy, A., Joly, A., 2018. Advances in Water Resources A SPH elastic-viscoplastic model for granular flows and bed-load

transport. Adv Water Resour 111, 156–173. https://doi.org/10.1016/j.advwatres.2017.11.007

Gingold, R.A., Monaghan, J.J., 1977. Smoothed particle hydrodynamics: theory and application to non-spherical stars. Mon Not R Astron Soc 181, 375–389.

Goodwin, S.R., Lapillonne, S., Piton, G., Chambon, G., 2023. An SPH study on viscoplastic surges overriding mobile beds: The many regimes of entrainment. Comput Geosci 181. https://doi.org/10.1016/j.cageo.2023.105476

Gray, J.P., Monaghan, J.J., Swift, R.P., 2001. SPH elastic dynamics. Comput Methods Appl Mech Eng 190, 6641–6662. https://doi.org/10.1016/S0045-7825(01)00254-7

Gregoretti, C., Degetto, M., Bernard, M., Boreggio, M., 2018. The debris flow occurred at ru secco creek, venetian dolomites, on 4 august 2015: Analysis of the phenomenon, its characteristics and reproduction by models. Front Earth Sci (Lausanne) 6, 1–20. https://doi.org/10.3389/feart.2018.00080

Griffiths, D. V., Lane, P.A., 1999. Slope stability analysis by finite elements. Geotechnique 49, 387–403.

Guo, J., Cui, Y., Xu, W., Yin, Y., Li, Y., Jin, W., 2022. Numerical investigation of the landslide-debris flow transformation process considering topographic and entrainment effects: a case study. Landslides 19, 773–788. https://doi.org/10.1007/s10346-021-01791-6

Han, Z., Chen, G., Li, Y., Tang, C., Xu, L., He, Y., Huang, X., Wang, W., 2015. Numerical simulation of debris-flow behavior incorporating a dynamic method for estimating the entrainment. Eng Geol 190, 52–64. https://doi.org/10.1016/j.enggeo.2015.02.009

Han, Z., Su, B., Li, Y., Dou, J., Wang, W., Zhao, L., 2020. Modeling the progressive entrainment of bed sediment by viscous debris flows using the three-dimensional SC-HBP-SPH method. Water Res 182, 116031. https://doi.org/10.1016/j.watres.2020.116031

Han, Z., Su, B., Li, Y., Wang, Wei, Wang, Weidong, Huang, J., Chen, G., 2019. Numerical simulation of debris-flow behavior based on the SPH method incorporating the Herschel-Bulkley-Papanastasiou rheology model. Eng Geol 255, 26–36. https://doi.org/10.1016/j.enggeo.2019.04.013

Han, Z., Wang, W., Li, Y., Huang, J., Su, B., Tang, C., Chen, G., Qu, X., 2018. An integrated method for rapid estimation of the valley incision by debris flows. Eng Geol 232, 34–45. https://doi.org/10.1016/j.enggeo.2017.11.007

He, X., Liang, D., Wu, W., Cai, G., Zhao, C., Wang, S., 2018. Study of the interaction between dry granular flows and rigid barriers with an SPH model. Int J Numer Anal Methods Geomech 42, 1217–1234. https://doi.org/10.1002/nag.2782

Hérault, A., Bilotta, G., Vicari, A., Rustico, E., del Negro, C., 2011. Numerical simulation of lava flow using a GPU SPH model. Annals of Geophysics 54, 600–620. https://doi.org/10.4401/ag-5343

Hong, Y., Wang, J.P., Li, D.Q., Cao, Z.J., Ng, C.W.W., Cui, P., 2015. Statistical and probabilistic

analyses of impact pressure and discharge of debris flow from 139 events during 1961 and 2000 at Jiangjia Ravine, China. Eng Geol 187, 122–134. https://doi.org/10.1016/j.enggeo.2014.12.011

Hu, M., Liu, M.B., Xie, M.W., Liu, G.R., 2015. Three-dimensional run-out analysis and prediction of flow-like landslides using smoothed particle hydrodynamics. Environ Earth Sci 73, 1629–1640. https://doi.org/10.1007/s12665-014-3513-1

Hu, S., Wang, X., Wang, N., Yang, D., Wang, D., Ma, S., Song, Z., Cao, M., 2022. Dynamic process, influence, and triggering mechanism of slope remodelling by landslide clusters in the South Jingyang Tableland, China. Catena (Amst) 217, 106518. https://doi.org/10.1016/j.catena.2022.106518

Hu, X.Y., Adams, N.A., 2006. A multi-phase SPH method for macroscopic and mesoscopic flows. J Comput Phys 213, 844–861. https://doi.org/10.1016/j.jcp.2005.09.001

Huang, H., Yang, K., Lai, S., 2007. Impact force of debris flow on filter dam. European Geosciences Union General Assembly 9, 1–32.

Huang, Y., Dai, Z., 2014. Large deformation and failure simulations for geo-disasters using smoothed particle hydrodynamics method. Eng Geol 168, 86–97. https://doi.org/10.1016/j.enggeo.2013.10.022

Huang, Y., Jin, X., Ji, J., 2022a. Effects of Barrier Stiffness on Debris Flow Dynamic Impact—I: Laboratory Flume Test. Water (Switzerland) 14. https://doi.org/10.3390/w14020177

Huang, Y., Jin, X., Ji, J., 2022b. Effects of Barrier Stiffness on Debris Flow Dynamic Impact—II: Numerical Simulation. Water (Switzerland) 14. https://doi.org/10.3390/w14020182

Hübl, J., Nagl, G., Suda, J., Rudolf-Miklau, F., 2017. Standardized Stress Model for Design of Torrential Barriers under Impact by Debris Flow (According to Austrian Standard Regulation 24801). International Journal of Erosion Control Engineering 10, 47–55. https://doi.org/10.13101/ijece.10.47

Hungr, O., 1995. A model for the runout analysis of rapid flow slides, debris flows, and avalanches. Canadian Geotechnical Journal 32, 610–623. https://doi.org/10.1139/t95-063

Hungr, O., Evans, S.G., 2004. Entrainment of debris in rock avalanches: An analysis of a long run-out mechanism. Bulletin of the Geological Society of America 116, 1240–1252. https://doi.org/10.1130/B25362.1

Hungr, O., McDougall, S., Bovis, M., 2007. Entrainment of material by debris flows. Debris-flow Hazards and Related Phenomena 135–158. https://doi.org/10.1007/3-540-27129-5_7

Iverson, R.M., 2012. Elementary theory of bed-sediment entrainment by debris flows and avalanches. J Geophys Res Earth Surf 117, 1–17. https://doi.org/10.1029/2011JF002189

Iverson, R.M., Logan, M., Lahusen, R.G., Berti, M., 2010. The perfect debris flow? Aggregated results from 28 large-scale experiments. J Geophys Res Earth Surf 115, 1–29. https://doi.org/10.1029/2009JF001514

Iverson, R.M., Ouyang, C., 2015. Entrainment of bed material by Earth-surface mass flows: Review and reformulation of depth-integrated theory. Reviews of Geophysics 53, 27–58. https://doi.org/10.1002/2013RG000447

Jiang, C., Schroeder, C., Teran, J., Stomakhin, A., Selle, A., 2016. The Material Point Method for Simulating Continuum Materials, in: Proceedings of the ACM SIGGRAPH 2016 Courses. pp. 1–52.

Jiang, Y.J., Towhata, I., 2013. Experimental study of dry granular flow and impact behavior against a rigid retaining wall. Rock Mech Rock Eng 46, 713–729. https://doi.org/10.1007/s00603-012-0293-3

Jin, Y.F., Yin, Z.Y., Yuan, W.H., 2020a. Simulating retrogressive slope failure using two different smoothed particle finite element methods: A comparative study. Eng Geol 279, 105870. https://doi.org/10.1016/j.enggeo.2020.105870

Jin, Y.F., Yuan, W.H., Yin, Z.Y., Cheng, Y.M., 2020b. An edge-based strain smoothing particle finite element method for large deformation problems in geotechnical engineering. Int J Numer Anal Methods Geomech 44, 923–941. https://doi.org/10.1002/nag.3016

Kennedy, R., Take, W.A., Siemens, G., 2021. Geotechnical centrifuge modelling of retrogressive sensitive clay landslides. Canadian Geotechnical Journal 58, 1452–1465. https://doi.org/10.1139/cgj-2019-0677

Kohv, M., Talviste, P., Hang, T., Kalm, V., 2010. Retrogressive slope failure in glaciolacustrine clays: Sauga landslide, western Estonia. Geomorphology 124, 229–237. https://doi.org/10.1016/j.geomorph.2010.03.007

Komatina, D., Jovanovíc, M., 1997. Experimental study of steady and unsteady free surface flows with water-clay mixtures. Journal of Hydraulic Research 35, 579–590. https://doi.org/10.1080/00221689709498395

Krimi, A., Khelladi, S., Nogueira, X., Deligant, M., Ata, R., Rezoug, M., 2018. Multiphase smoothed particle hydrodynamics approach for modeling soil–water interactions. Adv Water Resour 121, 189–205. https://doi.org/10.1016/j.advwatres.2018.08.004

Lei, Y., Cui, P., Zeng, C., Guo, Y., 2018. An empirical mode decomposition-based signal process method for two-phase debris flow impact. Landslides 15, 297–307. https://doi.org/10.1007/s10346-017-0864-1

Li, X., Sovilla, B., Ligneau, C., Jiang, C., Gaume, J., 2022. Different erosion and entrainment mechanisms in snow avalanches. Mech Res Commun 124, 103914. https://doi.org/10.1016/j.mechrescom.2022.103914

Li, X., Wu, Y., He, S., Su, L., 2016. Application of the material point method to simulate the post-failure runout processes of the Wangjiayan landslide. Eng Geol 212, 1–9. https://doi.org/10.1016/j.enggeo.2016.07.014

Li, X., Xie, Y., Gutierrez, M., 2018. A soft–rigid contact model of MPM for granular flow impact on retaining structures. Comput Part Mech 5, 529–537. https://doi.org/10.1007/s40571-018-0188-5

Li, X., Yan, Q., Zhao, S., Luo, Y., Wu, Y., Wang, D., 2020. Investigation of influence of baffles on landslide debris mobility by 3D material point method. Landslides 17, 1129–1143. https://doi.org/10.1007/s10346-020-01346-1

Li, X., Zhao, J., 2018. A unified CFD-DEM approach for modeling of debris flow impacts on flexible barriers. Int J Numer Anal Methods Geomech 42, 1643–1670. https://doi.org/10.1002/nag.2806

Liang, H., He, S., Liu, W., 2020. Dynamic simulation of rockslide-debris flow based on an elastic–plastic framework using the SPH method. Bulletin of Engineering Geology and the Environment 79, 451–465. https://doi.org/10.1007/s10064-019-01537-8

Libersky, L.D., Petschek, A.G., Carney, T.C., Hipp, J.R., Allahdadi, F.A., 1993a. High strain lagrangian hydrodynamics a three-dimensional SPH code for dynamic material response. J Comput Phys. https://doi.org/10.1006/jcph.1993.1199

Libersky, L.D., Petschek, A.G., Carney, T.C., Hipp, J.R., Allahdadi, F.A., 1993b. High strain lagrangian hydrodynamics a three-dimensional SPH code for dynamic material response. J Comput Phys. https://doi.org/10.1006/jcph.1993.1199

Liu, C., Liang, L., 2022. A coupled SPH–DEM–FEM approach for modeling of debris flow impacts on flexible barriers. Arabian Journal of Geosciences 15. https://doi.org/10.1007/s12517-022-09739-3

Liu, C., Sun, Q., Zhou, G.G.D., 2018. Coupling of material point method and discrete element method for granular flows impacting simulations. Int J Numer Methods Eng 115, 172–188. https://doi.org/10.1002/nme.5800

Liu, M.B., Liu, G.R., 2006. Restoring particle consistency in smoothed particle hydrodynamics. Applied Numerical Mathematics 56, 19–36. https://doi.org/10.1016/j.apnum.2005.02.012

Liu, X., Wang, Y., Li, D.Q., 2019. Investigation of slope failure mode evolution during large deformation in spatially variable soils by random limit equilibrium and material point methods. Comput Geotech 111, 301–312. https://doi.org/10.1016/j.compgeo.2019.03.022

Lo, E.Y.M., Shao, S., 2002. Simulation of near-shore solitary wave mechanics by an incompressible SPH method. Applied Ocean Research 24, 275–286. https://doi.org/10.1016/S0141-1187(03)00002-6

Locat, A., Jostad, H.P., Leroueil, S., 2013. Numerical modeling of progressive failure and its implications for spreads in sensitive clays. Canadian Geotechnical Journal 50, 961–978. https://doi.org/10.1139/cgj-2012-0390

Locat, A., Leroueil, S., Bernander, S., Demers, D., Jostad, H.P., Ouehb, L., 2011. Progressive failures in eastern canadian and scandinavian sensitive clays. Canadian Geotechnical Journal 48, 1696–1712. https://doi.org/10.1139/t11-059

Lucy, L.B., 1977. A numerical approach to the testing of the fission hypothesis. Astron J 82, 1013–1024.

Luo, F., Zhang, G., 2016. Progressive failure behavior of cohesive soil slopes under water drawdown

conditions. Environ Earth Sci 75, 1–12. https://doi.org/10.1007/s12665-016-5802-3

Ma, S., Zhang, X., 2007. Material Point Method for Impact and Explosion Problems. Comput Mech 156–166. https://doi.org/10.1007/978-3-540-75999-7_14

Major, J.J., Pierson, T.C., 1992. Debris Flow Rheology: Experimental Analysis of Fine-Grained Slurries. Water Resour Res 28, 841–857.

Mangeney, A., Roche, O., Hungr, O., Mangold, N., Faccanoni, G., Lucas, A., 2010. Erosion and mobility in granular collapse over sloping beds. J Geophys Res Earth Surf 115, 1–21. https://doi.org/10.1029/2009JF001462

Marrone, S., Antuono, M., Colagrossi, A., Colicchio, G., Le Touzé, D., Graziani, G., 2011. δ-SPH model for simulating violent impact flows. Comput Methods Appl Mech Eng 200, 1526–1542. https://doi.org/10.1016/j.cma.2010.12.016

Marrone, S., Colagrossi, A., Antuono, M., Colicchio, G., Graziani, G., 2013. An accurate SPH modeling of viscous flows around bodies at low and moderate Reynolds numbers. J Comput Phys 245, 456–475. https://doi.org/10.1016/j.jcp.2013.03.011

Mast, C.M., Arduino, P., Miller, G.R., Mackenzie-Helnwein, P., 2014. Avalanche and landslide simulation using the material point method: flow dynamics and force interaction with structures. Comput Geosci 18, 817–830. https://doi.org/10.1007/s10596-014-9428-9

McDougall, S., Hungr, O., 2005. Dynamic modelling of entrainment in rapid landslides. Canadian Geotechnical Journal 42, 1437–1448. https://doi.org/10.1139/t05-064

McDougall, S., Hungr, O., 2004. A model for the analysis of rapid landslide motion across three-dimensional terrain. Canadian Geotechnical Journal 41, 1084–1097. https://doi.org/10.1139/T04-052

Medina, V., Hürlimann, M., Bateman, A., 2008. Application of FLATModel, a 2D finite volume code, to debris flows in the northeastern part of the Iberian Peninsula. Landslides 5, 127–142. https://doi.org/10.1007/s10346-007-0102-3

Michael, W.H., 2000. Bedding parallel shear zones as landslides mechanisms in horizontal sedimentary rocks. Environmental and Engineering Geoscience 95–2113.

Molteni, D., Colagrossi, A., 2009. A simple procedure to improve the pressure evaluation in hydrodynamic context using the SPH. Comput Phys Commun 180, 861–872. https://doi.org/10.1016/j.cpc.2008.12.004

Monaghan, J.J., 2000. SPH without a Tensile Instability. J Comput Phys 159, 290–311. https://doi.org/10.1006/jcph.2000.6439

Monaghan, J.J., 1994. Simulating free surface flows with SPH. J Comput Phys. https://doi.org/10.1006/jcph.1994.1034

Monaghan, J.J., 1988. An introduction to SPH. Comput Phys Commun 48, 89–96. https://doi.org/10.1016/0010-4655(88)90026-4

Monaghan, J.J., Kos, A., 1999. Solitary Waves on a Cretan Beach. J Waterw Port Coast Ocean Eng

125, 145–155. https://doi.org/10.1061/(asce)0733-950x(1999)125:3(145)

Morgenstern, N.R., Price, V.E., 1965. The analysis of the stability of general slip surfaces. Geotechnique 15, 79–93. https://doi.org/10.1680/geot.1965.15.1.79

Moriguchi, S., Borja, R.I., Yashima, A., Sawada, K., 2009. Estimating the impact force generated by granular flow on a rigid obstruction. Acta Geotech 4, 57–71. https://doi.org/10.1007/s11440-009-0084-5

Morris, J.P., Fox, P.J., Zhu, Y., 1997. Modeling low Reynolds number incompressible flows with curved boundaries using SPH. J Comput Phys 136, 214–226. https://doi.org/10.1002/fld.2600

Ng, C.W.W., Choi, C.E., Cheung, D.K.H., Cui, Y., 2019. Effects of dynamic fragmentation on the impact force exerted on rigid barrier: Centrifuge modelling. Canadian Geotechnical Journal 56, 1215–1224. https://doi.org/10.1139/cgj-2018-0092

Ng, C.W.W., Choi, C.E., Goodwin, G.R., Cheung, W.W., 2017a. Interaction between dry granular flow and deflectors. Landslides 14, 1375–1387. https://doi.org/10.1007/s10346-016-0794-3

Ng, C.W.W., Choi, C.E., Goodwin, G.R., Cheung, W.W., 2017b. Interaction between dry granular flow and deflectors. Landslides 14, 1375–1387. https://doi.org/10.1007/s10346-016-0794-3

Ng, C.W.W., Song, D., Choi, C.E., Liu, L.H.D., Kwan, J.S.H., Koo, R.C.H., Pun, W.K., 2017c. Impact mechanisms of granular and viscous flows on rigid and flexible barriers. Canadian Geotechnical Journal 54, 188–206. https://doi.org/10.1139/cgj-2016-0128

Nikooei, M., Manzari, M.T., 2021. Investigating the effect of mixing layer rheology on granular flow over entrainable beds using SPH method. Comput Geosci 155. https://doi.org/10.1016/j.cageo.2021.104792

Nonoyama, H., Moriguchi, S., Sawada, K., Yashima, A., 2015. Slope stability analysis using smoothed particle hydrodynamics (SPH) method. Soils and Foundations 55, 458–470. https://doi.org/10.1016/j.sandf.2015.02.019

Oliver, J., Cante, J.C., Gonzalez, C., 2005. On particle finite element methods in solid mechanics problems. Computational Plasticity: Fundamentals and Applications - Proceedings of the 8th International Conference on Computational Plasticity, COMPLAS VIII 82–85. https://doi.org/10.1007/978-1-4020-6577-4

Oñate, E., Celigueta, M.A., Idelsohn, S.R., 2006. Modeling bed erosion in free surface flows by the particle finite element method. Acta Geotech 1, 237–252. https://doi.org/10.1007/s11440-006-0019-3

Oñate, E., Celigueta, M.A., Idelsohn, S.R., Salazar, F., Suárez, B., 2011. Possibilities of the particle finite element method for fluid-soil-structure interaction problems. Comput Mech 48, 307–318. https://doi.org/10.1007/s00466-011-0617-2

Oñate, E., Idelsohn, S.R., Celigueta, M.A., Rossi, R., 2008. Advances in the particle finite element method for the analysis of fluid-multibody interaction and bed erosion in free surface flows. Comput Methods Appl Mech Eng 197, 1777–1800. https://doi.org/10.1016/j.cma.2007.06.005

Papanastasiou, T.C., 1987. Flows of Materials with Yield. J Rheol (N Y N Y) 31, 385–404. https://doi.org/10.1122/1.549926

Parsons, J.D., Whipple, K.X., Simoni, A., 2001. Experimental study of the grain flow, fluid-mud transition in Debris flows. Journal of Geology 109, 427–447. https://doi.org/10.1086/320798

Pasculli, A., Minatti, L., Sciarra, N., Paris, E., 2013. SPH modeling of fast muddy debris flow:Numerical and experimental comparison of certain commonly utilized approaches. Italian Journal of Geosciences 132, 350–365. https://doi.org/10.3301/IJG.2013.01

Pastor, M., Haddad, B., Sorbino, G., Cuomo, S., Drempetic, V., 2009. A depth-integrated, coupled SPH model for flow-like landslides and related phenomena. Int J Numer Anal Methods Geomech 30, 1303–1336. https://doi.org/10.1002/nag

Peng, C., Bašić, M., Blagojević, B., Bašić, J., Wu, W., 2021. A Lagrangian differencing dynamics method for granular flow modeling. Comput Geotech 137. https://doi.org/10.1016/j.compgeo.2021.104297

Peng, C., Wu, W., Yu, H. sui, Wang, C., 2015. A SPH approach for large deformation analysis with hypoplastic constitutive model. Acta Geotech 10, 703–717. https://doi.org/10.1007/s11440-015-0399-3

Pudasaini, S.P., 2011. Some exact solutions for debris and avalanche flows. Physics of Fluids 23. https://doi.org/10.1063/1.3570532

Qiao, Z., Li, T., Simoni, A., Gregoretti, C., Bernard, M., Wu, S., Shen, W., Berti, M., 2023a. Numerical modelling of an alpine debris flow by considering bed entrainment. Front Earth Sci (Lausanne) 10, 1–17. https://doi.org/10.3389/feart.2022.1059525

Qiao, Z., Shen, W., Berti, M., Li, T., 2023b. An advanced SPH model for protective constructions of debris flows adopting the modified HBP constitutive law. Landslides. https://doi.org/10.1007/s10346-023-02123-6

Quinn, P.E., Diederichs, M.S., Rowe, R.K., Hutchinson, D.J., 2012. Development of progressive failure in sensitive clay slopes. Canadian Geotechnical Journal 49, 782–795. https://doi.org/10.1139/T2012-034

Randles, P.W., Libersky, L.D., 1996. Smoothed particle hydrodynamics: Some recent improvements and applications. Comput Methods Appl Mech Eng 139, 375–408. https://doi.org/10.1016/S0045-7825(96)01090-0

Rickenmann, D., Laigle, D., McArdell, B.W., Hübl, J., 2006. Comparison of 2D debris-flow simulation models with field events. Comput Geosci 10, 241–264. https://doi.org/10.1007/s10596-005-9021-3

Rossi, G., Armanini, A., 2019. Impact force of a surge of water and sediments mixtures against slit check dams. Science of the Total Environment 683, 351–359. https://doi.org/10.1016/j.scitotenv.2019.05.124

Sanvitale, N., Bowman, E., Cabrera, M.A., 2021. Experimental investigation on the impact dynamics

of saturated granular flows on rigid barriers. Environmental and Engineering Geoscience 27, 127–138. https://doi.org/10.2113/EEG-D-20-00033

Scheidl, C., Chiari, M., Kaitna, R., Müllegger, M., Krawtschuk, A., Zimmermann, T., Proske, D., 2013. Analysing Debris-Flow Impact Models, Based on a Small Scale Modelling Approach. Surv Geophys 34, 121–140. https://doi.org/10.1007/s10712-012-9199-6

Schürch, P., Densmore, A.L., Rosser, N.J., McArdell, B.W., 2011. Dynamic controls on erosion and deposition on debris-flow fans. Geology 39, 827–830. https://doi.org/10.1130/G32103.1

Sheikh, B., Qiu, T., Ahmadipur, A., 2021. Comparison of SPH boundary approaches in simulating frictional soil–structure interaction. Acta Geotech 16, 2389–2408. https://doi.org/10.1007/s11440-020-01063-y

Shen, W., Li, T., Li, P., Berti, M., Shen, Y., Guo, J., 2019a. A two-layer numerical model for simulating the frontal plowing phenomenon of flow-like landslides. Eng Geol 259, 105168. https://doi.org/10.1016/j.enggeo.2019.105168

Shen, W., Wang, D., He, S., Li, T., 2020. Numerical assessment of the impeding effect of check dams in the Hongchun debris flow gully, Sichuan Province, China. Bulletin of Engineering Geology and the Environment 79, 2833–2845. https://doi.org/10.1007/s10064-020-01755-5

Shen, W., Wang, D., Qu, H., Li, T., 2019b. The effect of check dams on the dynamic and bed entrainment processes of debris flows. Landslides 16, 2201–2217. https://doi.org/10.1007/s10346-019-01230-7

Shen, W., Zhao, T., Zhao, J., Dai, F., Zhou, G.G.D., 2018. Quantifying the impact of dry debris flow against a rigid barrier by DEM analyses. Eng Geol 241, 86–96. https://doi.org/10.1016/j.enggeo.2018.05.011

Shi, J., Li, B., Wu, S., Wang, T., Xin, P., 2013. Mechanism of Large-Scale Slide At Edge of Loess Plateau on North of Weihe River in Baoji Urban Area, Shaanxi Province. Journal of Engineering Geology 21, 938–949.

Shi, J.S., Wu, L.Z., Wu, S.R., Li, B., Wang, T., Xin, P., 2016. Analysis of the causes of large-scale loess landslides in Baoji, China. Geomorphology 264, 109–117. https://doi.org/10.1016/j.geomorph.2016.04.013

Shieh, C.L., Jan, C.D., Tsai, Y.F., 1996. A numerical simulation of debris flow and its application. Natural Hazards 13, 39–54. https://doi.org/10.1007/BF00156505

Simoni, A., Bernard, M., Berti, M., Boreggio, M., Lanzoni, S., Stancanelli, L.M., Gregoretti, C., 2020. Runoff-generated debris flows: Observation of initiation conditions and erosion–deposition dynamics along the channel at Cancia (eastern Italian Alps). Earth Surf Process Landf 45, 3556–3571. https://doi.org/10.1002/esp.4981

Solowski, W.T., Sloan, S.W., 2015. Evaluation of material point method for use in geotechnics. Int J Numer Anal Methods Geomech 39, 685–701. https://doi.org/10.1002/nag

Song, D., Choi, C.E., Ng, C.W.W., Zhou, G.G.D., 2018. Geophysical flows impacting a flexible
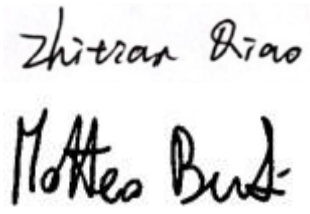
barrier: effects of solid-fluid interaction. Landslides 15, 99–110. https://doi.org/10.1007/s10346-017-0856-1

Song, D., Ng, C.W.W., Choi, C.E., Zhou, G.G.D., Kwan, J.S.H., Koo, R.C.H., 2017. Influence of debris flow solid fraction on rigid barrier impact. Canadian Geotechnical Journal 54, 1421–1434. https://doi.org/10.1139/cgj-2016-0502

Sovilla, B., Bartelt, P., 2002. Observations and modelling of snow avalanche entrainment. Natural Hazards and Earth System Sciences 2, 169–179. https://doi.org/10.5194/nhess-2-169-2002

Sovilla, B., Burlando, P., Bartelt, P., 2006. Field experiments and numerical modeling of mass entrainment in snow avalanches. J Geophys Res Earth Surf 111, 1–16. https://doi.org/10.1029/2005JF000391

Spencer, E., 1967. A method of analysis of the stability of embankments assuming parallel inter-slice forces. Géotechnique 17, 11–26.

Sun, L., Li, C., Shen, F., 2022. Two-surface progressive failure mechanism and stability quantitative evaluation of water-induced weakening retrogressive landslides: case study for clay landslides, China. Bulletin of Engineering Geology and the Environment 81. https://doi.org/10.1007/s10064-022-02860-3

Suwa, H., Okuda, S., Yokoyama, K., 1973. Observation system on rocky mudflow. Bulletin of the Disaster Prevention Research Institute 23, 59–73.

Swegle, J.W., Attaway, S.W., 1995. On the feasibility of using Smoothed Particle Hydrodynamics for underwater explosion calculations. Comput Mech 17, 151–168. https://doi.org/10.1007/BF00364078

Tan, D.-Y., Yin, J.-H., Feng, W.-Q., Zhu, Z.-H., Qin, J.-Q., Chen, W.-B., 2019. New Simple Method for Calculating Impact Force on Flexible Barrier Considering Partial Muddy Debris Flow Passing Through. Journal of Geotechnical and Geoenvironmental Engineering 145, 04019051. https://doi.org/10.1061/(asce)gt.1943-5606.0002133

Trujillo-Vela, M.G., Galindo-Torres, S.A., Zhang, X., Ramos-Cañón, A.M., Escobar-Vargas, J.A., 2020. Smooth particle hydrodynamics and discrete element method coupling scheme for the simulation of debris flows. Comput Geotech 125, 103669. https://doi.org/10.1016/j.compgeo.2020.103669

Ulrich, C., 2013. Smoothed-Particle-Hydrodynamics Simulation of Port Hydrodynamic Problems, Doku.B.Tu-Harburg.De.

Ulrich, C., Leonardi, M., Rung, T., 2013. Multi-physics SPH simulation of complex marine-engineering hydrodynamic problems. Ocean Engineering 64, 109–121. https://doi.org/10.1016/j.oceaneng.2013.02.007

Uzuoka, R., Yashima, A., Kawakami, T., Konrad, J.M., 1998. Fluid dynamics based prediction of liquefaction induced lateral spreading. Comput Geotech 22, 243–282. https://doi.org/10.1016/S0266-352X(98)00006-8
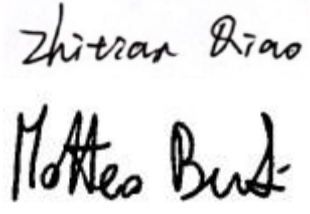
Vardon, P.J., Wang, B., Hicks, M.A., 2017. Slope failure simulations with MPM. Journal of Hydrodynamics 29, 445–451. https://doi.org/10.1016/S1001-6058(16)60755-2

Verlet, L., 1967. Computer experiments on classical fluids. I. Thermodynamical properties of Leonard–Jones molecules. Physical Review 159, 98–103.

Vicari, H., Tran, Q.A., Nordal, S., Thakur, V., 2022. MPM modelling of debris flow entrainment and interaction with an upstream flexible barrier. Landslides 19, 2101–2115. https://doi.org/10.1007/s10346-022-01886-8

Wang, B., Feng, X., Pan, P., Li, S., 2017. Slope failure analysis using the material point method. Yanshilixue Yu Gongcheng Xuebao/Chinese Journal of Rock Mechanics and Engineering 36, 2146–2155. https://doi.org/10.13722/j.cnki.jrme.2017.0314

Wang, B., Vardon, P.J., Hicks, M.A., 2016. Investigation of retrogressive and progressive slope failure mechanisms using the material point method. Comput Geotech 78, 88–98. https://doi.org/10.1016/j.compgeo.2016.04.016

Wang, C., Ye, G., Meng, X., Wang, Y., Peng, C., 2021. A eulerian–lagrangian coupled method for the simulation of submerged granular column collapse. J Mar Sci Eng 9. https://doi.org/10.3390/jmse9060617

Wang, H., Sun, P., Wang, G., Wu, L., 2021. Experimental and numerical study of shallow loess slope failure induced by irrigation. Catena (Amst) 206. https://doi.org/10.1016/j.catena.2021.105548

Wang, H., Sun, P., Zhang, S., Han, S., Li, X., Wang, T., Guo, Q., Xin, P., 2020. Rainfall-induced landslide in loess area, Northwest China: a case study of the Changhe landslide on September 14, 2019, in Gansu Province. Landslides 17, 2145–2160. https://doi.org/10.1007/s10346-020-01460-0

Wang, Y., Qin, Z., Liu, X., Li, L., 2019. Probabilistic analysis of post-failure behavior of soil slopes using random smoothed particle hydrodynamics. Eng Geol 261. https://doi.org/10.1016/j.enggeo.2019.105266

Wendeler, C., Volkwein, A., Roth, A., Denk, M., Wartmann, S., 2007. Field measurements used for numerical modelling of flexible debris flow barriers. International Conference on Debris-Flow Hazards Mitigation: Mechanics, Prediction, and Assessment, Proceedings 681–687.

Wendland, H., 1995. Piecewise polynomial, positive definite and compactly supported radial functions of minimal degree. Adv Comput Math 4, 389–396. https://doi.org/10.1007/BF02123482

Xin, P., Liu, Z., Wu, Shuren, Liang, C., Lin, C., 2018. Rotational–translational landslides in the neogene basins at the northeast margin of the Tibetan Plateau. Eng Geol 244, 107–115. https://doi.org/10.1016/j.enggeo.2018.07.024

Xu, L., Dai, F., Chen, J., Iqbal, J., Qu, Y., 2014. Analysis of a progressive slope failure in the Xiangjiaba reservoir area, Southwest China. Landslides 11, 55–66. https://doi.org/10.1007/s10346-012-0373-1

Yenes, M., Monterrubio, S., Nespereira, J., Santos, G., 2009. Geometry and kinematics of a landslide surface in tertiary clays from the Duero Basin (Spain). Eng Geol 104, 41–54. https://doi.org/10.1016/j.enggeo.2008.08.008

Yenes, M., Monterrubio, S., Nespereira, J., Santos, G., Fernández-Macarro, B., 2015. Large landslides induced by fluvial incision in the Cenozoic Duero Basin (Spain). Geomorphology. https://doi.org/10.1016/j.geomorph.2015.06.022

Yu, X., Chen, X., Wang, H., Jia, C., 2020. Numerical Study on the Interaction Between Debris Flow Slurry and Check Dams Based on Fluid–Solid Coupling Theory. Geotechnical and Geological Engineering 38, 2427–2445. https://doi.org/10.1007/s10706-019-01160-0

Yuan, W.H., Liu, K., Zhang, W., Dai, B., Wang, Y., 2020. Dynamic modeling of large deformation slope failure using smoothed particle finite element method. Landslides 17, 1591–1603. https://doi.org/10.1007/s10346-020-01375-w

Zabala, F., Alonso, E.E., 2011. Progressive failure of aznalcóllar dam using the material point method. Géotechnique 61, 795–808. https://doi.org/10.1680/geot.9.P.134

Zhang, B., Huang, Y., 2022. Impact behavior of superspeed granular flow: Insights from centrifuge modeling and DEM simulation. Eng Geol 299, 106569. https://doi.org/10.1016/j.enggeo.2022.106569

Zhang, W., Zhong, Z. hao, Peng, C., Yuan, W. hai, Wu, W., 2021. GPU-accelerated smoothed particle finite element method for large deformation analysis in geomechanics. Comput Geotech 129, 103856. https://doi.org/10.1016/j.compgeo.2020.103856

Zhang, X., Sheng, D., Sloan, S.W., Bleyer, J., 2017. Lagrangian modelling of large deformation induced by progressive failure of sensitive clays with elastoviscoplasticity. Int J Numer Methods Eng 112, 963–989. https://doi.org/10.1002/nme.5539

Zhang, X., Sloan, S.W., Oñate, E., 2018. Dynamic modelling of retrogressive landslides with emphasis on the role of clay sensitivity. Int J Numer Anal Methods Geomech 42, 1806–1822. https://doi.org/10.1002/nag.2815

Zhang, X., Wang, L., Krabbenhoft, K., Tinti, S., 2020. A case study and implication: particle finite element modelling of the 2010 Saint-Jude sensitive clay landslide. Landslides 17, 1117–1127. https://doi.org/10.1007/s10346-019-01330-4

Zhang, Z., Jin, X., Bi, J., 2019. Development of an SPH-based method to simulate the progressive failure of cohesive soil slope. Environ Earth Sci 78, 1–15. https://doi.org/10.1007/s12665-019-8507-6

Zhou, G.G.D., Song, D., Choi, C.E., Pasuto, A., Sun, Q.C., Dai, D.F., 2018. Surge impact behavior of granular flows: effects of water content. Landslides 15, 695–709. https://doi.org/10.1007/s10346-017-0908-6

Zienkiewicz, O.C., Humpheson, C., Lewis, R.W., 1975. Associated and non-associated visco-plasticity and plasticity in soil mechanics. Géotechnique 25, 671–689. https://doi.org/10.1680/geot.1977.27.1.101

Co-author declaration

This declaration states the independent research contribution of the PhD candidate for each paper compiled in the thesis and other papers published during the doctoral period.

Paper No.	Title and full bibliographic reference		
Paper I	Qiao, Z., Shen, W., Berti, M., Li, T., 2023b. An advanced SPH model for protective constructions of debris flows adopting the modified HBP constitutive law. Landslides. https://doi.org/10.1007/s10346-023-02123-6		
Role of PhD candidate	**Type of contribution**	**overall contribution (%)**	**Signature of PhD candidate and supervisor**
First author	Algorithm – compilation and debugging; Model Validation; Visualization; Writing - original manuscript and review; Field investigation	>75%	*Zhitian Qiao* *Matteo Berti*

Paper No.	Title and full bibliographic reference		
Paper II	Qiao, Z., Li, T., Simoni, A., Gregoretti, C., Bernard, M., Wu, S., Shen, W., Berti, M., 2023a. Numerical modelling of an alpine debris flow by considering bed entrainment. Front. Earth Sci. 10, 1–17. https://doi.org/10.3389/feart.2022.1059525		
Role of PhD candidate	**Type of contribution**	**overall contribution (%)**	**Signature of PhD candidate and supervisor**
First author	Software; Conceptualization; Model Validation; Visualization; Writing - original draft and review Editing; Field investigation	>75%	*Zhitian Qiao* *Matteo Berti*

Paper No.	Title and full bibliographic reference
Paper III	Shen, W., Berti, M., Li, T., Benini, A., Qiao, Z., 2022. The influence of slope gradient and gully channel on the run-out behavior of rockslide-debris flow:

Role of PhD candidate	Type of contribution	overall contribution (%)	Signature of PhD candidate and supervisor
an analysis on the Verghereto landslide in Italy. Landslides 19, 885–900. https://doi.org/10.1007/s10346-022-01848-0			
Corresponding author	Model Development; Methodology; Writing – review editing	30-50%	*Zhiran Qiao* *Matteo Berti*